



UNIVERSITAT POLITÈCNICA
DE CATALUNYA
BARCELONATECH



Institut
de Ciències
Fotòniques

Mechanochemical study of single living
cells and biomolecules combining
optical tweezers and Raman spectroscopy

Saurabh Raj

ICFO – The Institute Photonic Sciences

Universitat Politècnica de Catalunya

Barcelona 2012

Mechanochemical study of single living
cells and biomolecules combining
optical tweezers and Raman spectroscopy

Saurabh Raj

under the supervision of
Prof. Dmitri Petrov

submitted this thesis in partial fulfillment of the
requirements for the degree of
Doctor of Philosophy

by the

Universitat Politècnica de Catalunya

Barcelona 2012

To my loving parents

Take up one idea. Make that one idea your life - think of it, dream of it, live on that idea. Let the brain, muscles, nerves, every part of your body, be full of that idea, and just leave every other idea alone. This is the way to success, that is the way great spiritual giants are produced.

SWAMI VIVEKANANDA

At the heart of science is an essential balance between two seemingly contradictory attitudes - an openness to new ideas, no matter how bizarre or counterintuitive they may be, and the most ruthless skeptical scrutiny of all ideas, old and new. This is how deep truths are winnowed from deep nonsense.

CARL SAGAN

Acknowledgements

I would never have been able to finish my dissertation without the encouragement of several individuals, such as, group members, friends, and my loving family, who in one way or another contributed and extended their precious support in the realization and completion of this work.

First of all, I would like to express my sincere gratitude to Prof. Dmitri Petrov for giving me this opportunity to pursue doctoral studies under his supervision. This thesis would not have been possible without his constant guidance, motivation and sharing his vast experience in understanding how things work in experimental world. His passion for research and vast scientific knowledge has always been a source of inspiration. I express my deepest gratitude to him.

I want to express my gratitude to Prof. Lluís Torner, Director of ICFO - The Institute of Photonic Sciences, and his management team, for financial support during my research work, and for making ICFO such a wonderful place for research. His leadership skills will always be an inspiration for me.

A significant role in the progress of science and technology at ICFO is the support of administrative and human resources staff. I would like to thank the Human Resource unit for taking care of all the administrative and bureaucratic matters during my stay at ICFO and thus, allowing me to concentrate only on my research. I am thankful to the purchasing unit for their valuable help and rapid processing of equipment purchases and travel funds. I am also thankful for the timely support from the mechanical and electronic workshop of ICFO, without them, working at ICFO would not have been easy. I would also like to thank the cleaning staff for providing us a clean and hygienic environment to work.

I am thankful to Fundació privada Cellex, Barcelona and Generalitat de Catalunya, without their funding my PhD would not have been possible.

In my daily work I have been blessed with a friendly and cheerful group. I would like to specially thank Filip, not only for his valuable advice in scientific discussions, but also for his immense support to make my stay in Barcelona pleasant. It was a pleasure to work with Michal and Ignacio on various projects. I have always enjoyed many scientific and non-scientific discussions that we had during coffee breaks and various outings. Many thanks to Ignacio for translating my abstract in Spanish. Stefan, Satish, Monica, Claudia and Ali, all have been a wonderful person and made my stay in Barcelona very comfortable in both scientific and non-scientific way.

I would like to thank Dr. Susana Campoy and Carlota for helping me in PCR techniques and Prof. Felix Ritort and Joan for helping me in making a stronger DNA-bead construct.

I am also thankful to Prof. P. K. Gupta, Dr. Deepthy Menon, Sri Raktim Dasgupta, Prof. Nampoore and many other college and school teachers for lending their precious time and advice to me and contributing in my development at different stages of my life.

I would like to thank all my friends Joyee, Chaitanya, Mousumi, Kanchan, Ramaiah, Srividya, Arup, Goutam, Dhriti, Nikhil, Sudhir, Manoj, Kavita, Ritwick, Ujjwal da, Aditi di, Rajan, Pavan, Anju and many others for making my stay enjoyable. I would also like to show appreciation towards my school and

college friends. Special thanks to Varun, Avishek and Vishal for the wonderful friends they have been.

I would like to express my deepest admiration towards Jasleen for her love, dedication and support.

Where would I be without my family? I cannot thank my parents, Sri Nakul Lall and Late Smt Pushpa Lall, enough. They stood by me unconditionally for all my life. They were always there for me in my joy and sorrow, even though I was not able to be there for them when needed. My mother sincerely raised me with her caring and gentle love and helped me in becoming a good human being. Her untimely demise during my PhD left a void never to be filled again. My father has been my hero and my first teacher. He gave me full freedom and provided me with all the requirements to lead a meaningful life. They are always the motivation for every constructive thing I have done in my life. I am blessed to have Surabhi as my sibling. She has always been caring and supportive. I am fortunate to have Nimisha and Manisha as my sisters. I am grateful to Nimisha for all the love and care she has showered on me. I would also like to extend thanks to my brother in-laws, Mahendra and Pankaj, for guiding me through various parts of my life and always finding out time for me from their busy schedule.

Finally, I would like to thank everybody who was important to the successful realization of thesis, and my sincere apology to those whom I could not mention personally one by one.

Abstract

This thesis is devoted to the study of mechanochemistry of single cells and single biomolecules. Mechanochemistry relates to the association of mechanical and chemical occurrence at the molecular level. Using a combination of microrheological measurements and Raman spectroscopy based on optical tweezers we have shown how the molecular structures of single living cells and biomolecules are coupled with mechanical deformations.

The basic questions to respond in this work are: (i) How does a cell or a biomolecule detect an external force? (ii) How do the viscoelastic properties of living cells and biomolecules depend on its environment? (iii) How does the structure of the cell or biomolecules change because of the external force?

We use microrheology to detect the response of single cells (or biomolecules) to an external force. Two point microrheology is applied to study these samples - both in their relax configuration and in a stress situation when a known external force is applied. We are able to find non-linearities in mechanical response of RBC and DNA molecules subjected to an external load. In both the cases, an increase in elastic stiffness of the system is observed with increase in the force.

To detect changes in the molecular structures of DNA or a cell as a result of an applied mechanical load, Raman spectroscopy is used. Raman signals from biomolecules are rich and complex in nature and are accompanied with several noises. Hence processing of data is an important aspect in Raman spectroscopy. For gaining in-depth information regarding the behavior of the molecule under study, we used statistical techniques such as principal component analysis and 2D correlation spectroscopy.

Raman measurement of single DNA, with excitation optical beam focused by conventional optics, is almost impossible owing to very small thickness of DNA and inherent low efficiency of Raman scattering. To overcome this difficulty, we used additional optical phenomena - Surface Enhanced Raman Scattering (SERS) technique. With implementation of SERS, we were able to detect signals from single DNA molecule. Our study presents substantial findings that describe the structural changes of the phosphate backbone when DNA is extended in the entropic force regime. The current belief is that such forces are balanced by lowering DNA entropy via unfolding as the molecule is extended. While this is accurate, we observe structural movement at the bond level when the single biomolecule is extended at these low forces. This revelation has never been measured directly or predicted theoretically. The result gives a different view of DNA mechanical properties. We confirm and substantiate our experimental results with molecular dynamics simulations.

Raman signal from RBC is collected at various stretches across the length of the cell. Though the overall intensity of some bands remains almost constant, we observe changes in the intensity of certain peaks. We can identify three distinct regions for spectral changes along the varying length of RBC. Up to 15% of extension the RBC absorbs small forces without any noticeable changes in their molecular structure as the bands remain almost unchanged. In the mid-force region, molecular structure of RBC starts to change as is evident from an almost linear increase (or decrease) in intensity of certain bands. At even higher forces, the intensity saturates a bit and later on decreases (or increases). We

propose that at these extensions, molecular forces reach its maximum limit and on further extensions, rearrangement of bonds take place. We were able to relate the spectral changes to nonlinearities observed in microrheology measurements.

Novelty of this thesis consists in combining microrheology and Raman spectroscopy, and hence, in the potential ability to study the viscoelastic properties of living system in more quantitative manner, connecting them with molecular structure.

Resumen

Esta tesis se centra en el estudio de los procesos mecanoquímicos de células y biomoléculas individuales. La mecanoquímica relaciona la interacción entre la mecánica y la química a nivel molecular. Por éste motivo, usamos una combinación entre medidas microrreológicas obtenidas mediante la técnica de la trampa óptica y espectroscopía Raman. Mediante estas herramientas mostramos cómo las estructuras de las biomoléculas o de las células están conectadas con las deformaciones mecánicas.

Las preguntas básicas a responder en este trabajo son: (i) ¿Cómo la muestra (eritrocito o ADN) detecta fuerzas externas? (ii) ¿Cómo dependen las propiedades viscoelásticas del ambiente en el que se encuentra la muestra? (iii) ¿Cómo cambia la estructura de la muestra si se aplica una fuerza externa?

Usamos la microrreología para estudiar la respuesta de la muestra a una fuerza externa. La microrreología de dos puntos es aplicada para estudiar muestras individuales. Una vez aplicada una cierta tensión externa a cualquiera de los objetos de estudio, es posible encontrar efectos no lineales en la respuesta mecánica. Con el objeto de detectar cambios en la estructura molecular usaremos espectroscopía Raman. La señal Raman de compuestos biológicos es compleja y rica en información. Debido a ello, un procesamiento estadístico es un aspecto que ha siempre de acompañar a los datos experimentales. En este aspecto, para profundizar en la información que nos ofrece la muestra, usaremos técnicas como PCA y 2DCS.

La medida del espectro Raman de una molécula individual de ADN es casi imposible si tenemos en cuenta la escasa anchura del ADN junto a la baja eficiencia de Raman. Para superar esta dificultad haremos uso del efecto SERS. Gracias a esta técnica podremos obtener medidas de Raman de una molécula individual de ADN. Nuestro estudio describe los cambios estructurales de la cadena de fosfatos cuando el ADN es estirado dentro del régimen de fuerza entrópica. La explicación establecida es que las fuerzas simplemente se equilibran mediante una reducción de la entropía del ADN cuando la molécula es estirada. Si bien esto es correcto, nosotros observamos cambios estructurales a nivel de enlace cuando la biomolécula es estirada aplicando fuerzas débiles. Este hecho no había sido medido nunca antes experimentalmente y permite obtener una diferente visión de las propiedades mecánicas del ADN y su interacción con las proteínas que acaecen en este régimen de fuerzas. Estos resultados experimentales están confirmados gracias a simulaciones de la dinámica molecular.

La señal Raman de un glóbulo rojo (GR) individual es obtenida para diferentes grados de tensión celular. Es posible identificar tres diferentes regiones. Aunque algunas bandas presentan una intensidad sin cambios significativos, observamos un aumento (o reducción) en la intensidad de ciertos picos. Hasta un 15% de extensión desde el estado en reposo, el GR no presenta ningún cambio significativo en su espectro Raman. Esta primera región nos indica que el GR absorbe pequeñas tensiones sin ningún cambio significativo en su estructura molecular. De un 15% a un 20% de elongación, es apreciable un aumento (o disminución) casi lineal de ciertas bandas. Esto nos muestra cómo en esta región intermedia de fuerzas, la estructura molecular de la célula comienza a cambiar. A fuerzas mayores, la intensidad muestra una pequeña saturación,

que a continuación empezar a disminuir (o aumentar). Bajo nuestras hipótesis, a éstas extensiones, las fuerzas moleculares alcanzan su límite máximo y para mayores extensiones, los enlaces se reordenan. Los cambios en la intensidad de algunas bandas concuerdan con la no linealidad del glóbulo rojo, al igual que en las medidas microrreológicas.

La novedad presente en esta tesis se encuentra en la combinación de la microrreología con la espectroscopía Raman, y por tanto de poder relacionen los cambios de las propiedades viscoelásticas de la muestra con cambios en la estructura molecular.

Contents

Acknowledgements	i
Abstract	iii
Resumen	v
Introduction	x
1 Optical Tweezers	1
1.1 Working principle	1
1.1.1 Ray optics approach	3
1.1.2 Rayleigh regime	4
1.2 Trap calibration	5
2 Raman spectroscopy	8
2.0.1 Classical theory of Raman scattering.	10
2.0.2 Quantum theory of Raman scattering.	12
2.0.3 Resonance Raman scattering	14
2.0.4 Surface enhanced Raman scattering.	15
3 Microrheology	18
3.0.5 Macrorheology - Basic concepts	19
3.0.6 Viscoelasticity	20
3.1 Microrheology	24
3.1.1 Fluctuation-dissipation theorem	24
3.1.2 Generalized Stokes-Einstein relation	27
3.1.3 Passive microrheology	29
4 Materials and methods	33
4.1 Experimental set-up	33
4.1.1 Raman tweezers set-ups	33
4.1.2 Microrheology set-up	36
4.2 Fluid chamber	37
4.3 Sample preparations	38
4.3.1 Bead-DNA construct	38
4.3.2 RBC and bead preparation	39
4.3.3 Silver colloids	40
4.3.4 Silver coated silica bead	40
4.4 Statistical techniques used for processing experimental data	41
4.4.1 Processing of Raman signals	41
4.4.2 Signal from position detector - PSD and CSD	45

5	Detection of single DNA molecule in optical trap using SERS	46
5.1	Experimental method	46
5.2	Results and discussions	47
6	Structural rearrangement of DNA at low forces revealed by SERS	52
6.1	Experimental methods	53
6.2	Results and discussion	53
7	Single red blood cell under tunable external force studied by combining passive microrheology and Raman spectroscopy	58
7.1	Materials and methods	60
7.1.1	Bead-RBC-Bead construct	60
7.1.2	Data analysis method	61
7.1.3	Drag correction	62
7.1.4	Viscosity of Alsever's solution	63
7.2	Results and discussion	63
7.2.1	One-particle microrheology	63
7.2.2	Two-particles microrheology	66
7.2.3	Stiffness of the cell	68
7.2.4	Raman spectroscopy	71
7.3	Conclusion	74
8	Mechanochemistry of single red blood cells monitored using Raman tweezers	75
8.1	Materials and methods	76
8.2	Results	77
8.3	Discussions	78
8.4	Conclusion	83
9	Frequency dependent cross-correlated studies of single DNA mechanics using optical tweezers	84
9.1	Materials and methods	85
9.1.1	Data analysis method	86
9.2	Results and discussion	86
9.2.1	Stiffness of the DNA	88
9.3	Conclusion	90
10	Conclusions	92
A	Protocols for DNA construct	94
A.1	PCR protocol for amplifying DNA	94
A.2	DNA preparation through digestion of λ -DNA	97
A.2.1	λ -phage DNA Digestion	98
A.2.2	Preparation of the oligonucleotides	98
A.2.3	Purification of the oligonucleotides	99
A.2.4	Phosphorylation of the oligonucleotides	100
A.2.5	Annealing and ligation of the oligonucleotides with the DNA	101

B Protocol describing Labview program for DNA extension	102
B.1 Experiment's Outlook	103
B.2 Calibration of moving trap and picomotor	103
Annex 1: List of Publications of Saurabh Raj	107
Annex 2: Conferences and workshops	109
Annex 3: List of elements used in the optical set-ups	110
Bibliography	112

Introduction

Living cells and DNA are very complex systems. Cells are dynamic in nature - they live, multiply and die. At times they contain key informations regarding various diseases. For this reason they are called *basic unit of life*. They constantly communicate with their surroundings and actively trace the environment they are embedded into [1].

Deoxyribonucleic acid (DNA), on the other hand, contains genetic information (called genes) necessary for the functioning and development of all living organisms. DNA is also a highly active system as it goes under translation, transcription and replication. DNA has a width of $\sim 2 - 3\text{ nm}$ and its length, depending on the living organisms, can be tens of centimeters. At times, the condensation of DNA inside the cell nucleus may be 100 folds, which is an incredibly high density. Due to this enormous packaging density of DNA in the cell nucleus, changes in DNA topology can dictate role in many genetic reactions such as transcription, replication and recombination. Other than being an extremely interesting biomolecule, DNA is also studied as a model for polymer studies due to its semi-flexible nature [2]. The advancement in single molecule experiments [3] has gradually helped in a better understanding of mechanics of single biomolecules [4].

Mechanics directly control many functions of living cells and DNA, including the generation of forces, motion, and sensing of external forces [5]. The cytoskeleton is a network of semi-flexible linear protein polymers (actin filament, microtubules, and intermediate filaments) that is responsible for most of the mechanical functions of cells. They are different from common polymer materials, as they are highly complex and are not in thermal equilibrium. Chemical non-equilibrium drives mechanoenzymes (motor proteins) that are the force generators in cells. The cytoskeleton is thus an active material that can adapt its mechanics and perform mechanical tasks such as cell locomotion or cell division [6].

The influence of mechanical forces on individual cells and DNA has been long known. In a biological system, there exists a fine balance between the mechanical forces and chemical reactions of proteins, enzymes, and other molecular structures. Some common and well known examples are the mechanism of stretching and twisting that DNA undergoes during DNA-protein interaction and the conformational changes that a protein experiences during biochemical processes. At the single cell level, force can initiate cell protrusion, alter mobility and affect metabolic reactions, that regulate cell function, division and death. In addition to responding to externally imposing forces, cells also exert internally generated forces on the material to which they adhere. Some type of cells are exquisite detectors of material stiffness, changing their structure, motility and growth, as they interrogate the mechanical properties of their surroundings.

Just like an engineer, cells study the response of external medium by exerting some force and in the process assessing the medium properties. Cells generate forces through the cytoskeleton energized by motor proteins. They continuously adapt to changing environment with the help of transport molecules and signaling through intracellular regions with differing material properties, such as variation in viscosity and elasticity. Thus probing a cell's viscoelastic proper-

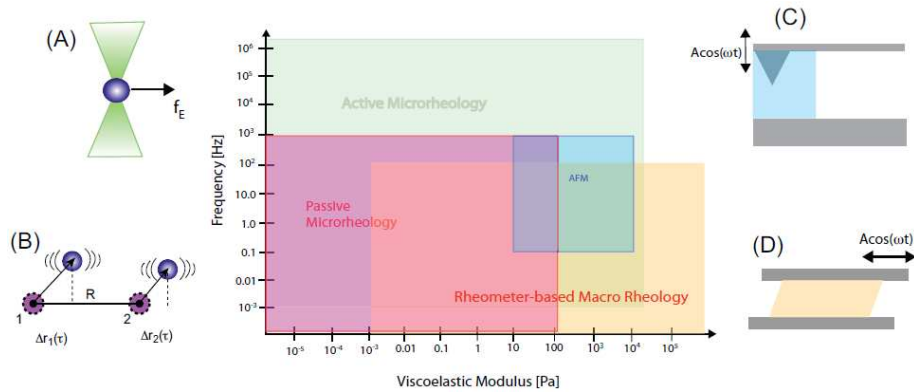


Figure 1: Rheological techniques employed over a decade to probe soft and complex materials. Main Figure: Typical frequency and viscoelastic modulus range of techniques. The contours represent min/max ranges of the techniques. Schematic illustrations of A) Active microrheology using optical tweezers to force probe particle. B) Passive two-point microrheology using image-based particle tracking. C) Dynamic measurement using atomic force microscopy (AFM). D) Oscillatory Macro-rheology (*Figure courtesy* [8]).

ties is quintessential in understanding the way cells behave in different conditions. Complete characterization of a polymer network, or soft matters, such as cells, require establishing a link between its structure, its equilibrium and non-equilibrium dynamics, and its rheology. Most of the times, these properties are coupled together, albeit in somewhat complex configuration. The dynamics of soft matter can be studied if we probe it mechanically. Rheology measurements typically subject a material to shear in a particular geometry and the material's response is then measured from the resultant stress and strain. These response functions are measures of a material's intrinsic elastic properties. Microrheology can be used for linking mechanical and structural characteristics of a cell with its biochemical properties [7], while spectroscopic technique in combination with mechanical measurements can give details regarding chemical changes at molecular level.

The material's properties, measured in terms of elastic moduli for solids or viscosities for liquids, are calculated from the ratio of stress to strain or stress to strain rate, respectively. To fully evaluate the viscoelastic properties of complex soft materials and polymers, the relation of stress to strain must be measured over a wide range of time scales. Various techniques have been applied in the past decade to obtain the rheological property of a material, as shown in fig. 1. Microrheology is an important experimental technique that uses the Brownian motion of submicron sized tracer particles to study the local viscoelastic properties of soft complex materials. The motion of the probe particle reflects the nature of the material in which it is embedded. If the particle is surrounded by a fluid, then its motion will be that of a diffusing particle whose diffusion coefficient depends on the viscosity of the fluid, that is, the motion of the particle will be diffusive in nature. If the particle is enclosed in an elastic network, by contrast, it will still move but its motion will be restricted

by the surrounding network, that is, the amount of motion will directly reflect the elasticity of the network. Thus, by measuring the motion of the particle either due to its thermal fluctuations (passive rheology) or due to its response to a driving force (active rheology), the elastic or loss modulus of the local environment of the particle can be probed.

Both active and passive microrheology has developed during the last ten years, however mainly to model solutions of parts of cytoskeletons or many living cells [9,10]. In this study we have applied the technique of passive rheology to study real single living cells or biomolecules like DNA, both in their relax configuration and in a stress situation when an external force, in particular, a (known and controllable) mechanical deformation is applied to the cell. When we apply some force to cells or biomolecules, then the basic questions to respond are:

- How does the cytoskeleton detect an external force?
- How do the viscoelastic properties of living cells and molecules depend on its environment?
- How does the structure of the cell or molecules change due to the external force?

There are three requirements to perform such an experiment. First, a tool is needed to isolate a cell and apply forces. Second, a method is necessary to monitor response of the cell as a result of the applied force. Third, a way to monitor the chemical changes of the cell under such a stress is necessary. The schematic of the requirements to the experiment is as shown in fig. 2. Several experimental techniques may satisfy the first and second requirements, including magnetic tweezers and atomic force microscope (AFM), but the optical trapping is the most promising and powerful tool due to its noninvasive nature and it is practically insensitive to the choice of the probe. In addition, because optical trapping may manipulate microscopic objects by exerting loads larger than thermal forces, both passive and active microrheology can be approached with a single and double probe [11,12]. Combining optical trapping with a position detection system, one can also achieve qualitative characterization of the mechanical force exerted on a studied living sample as well as its *mechanical* reaction.

Optical tweezers and atomic force microscope (AFM) are the most eligible candidates for studying structural and mechanical changes in single cell or biomolecules, as it is relatively easier to combine force measurements along with spectroscopic techniques in these cases. AFM uses a metal cantilever to probe a surface. Metal nanostructures are good source for local field enhancement and can be used for surface enhanced Raman/fluorescence spectroscopy. In fact, single RNA molecule was detected by combining AFM and Raman technique [13]. But one of the biggest issue in using AFM is the need of sample to be adhered to the surface. This is not a correct configuration if we want to analyze the biomolecules in proper physiological conditions. Another drawback of adhering the sample to the surface is the loss in the degrees of manipulations that can be achieved on the molecule. For example, it will be difficult to study the mechanism of DNA-protein interactions while observing the spectral changes using an AFM.

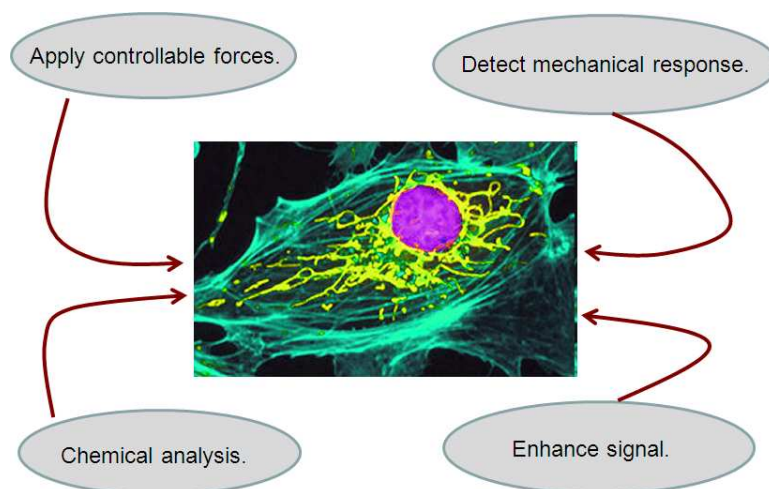


Figure 2: Schematic depicting the requirement of tools in process of studying the mechanochemistry of a biomolecule.

Optical tweezers, on the other hand, can be used to analyze biomolecules in physiological conditions. Combination of force measurements with spectroscopic techniques is straightforward in optical tweezers, as discussed in [14]. Manipulation of whole cell or DNA molecule can also be easily accomplished by trapping them between two microsphere handles. Recently, we measured Raman spectra from a single DNA molecule, trapped in dual-trap optical tweezers with the help of polystyrene beads [15].

A connection between the viscoelastic properties of studied living samples in the presence of external forces, along with monitoring the chemical changes - mechanochemistry - is of great importance: it permits one to reveal the contributions of different cell constituents to the overall changes in viscoelastic properties observed experimentally. Fluorescence has been shown as a potential tool for analyzing single molecules, such as in the experiments involving the manipulation of DNA [16]. In one of the early experiments using optical tweezers, a DNA - tens of microns in length, was labeled with ethidium bromide and stretched in two optical traps with polystyrene beads as handles. By simply watching the movements of the fluorescently labeled DNA, relaxation of the DNA could be followed as one bead was released. In a recently conducted experiment, possibilities of combining fluorescence imaging of multiply labeled molecules with optical tweezers force measurements was demonstrated. The elastic properties of a single dsDNA molecule, heterogeneously coated with filaments of Rad51 - an important component in eukaryotic homologous recombination, were investigated. In this assay, fluorescently labeled Rad51 filaments could be imaged on a piece of DNA tethered between two optically trapped beads. The response of both the fluorescent filaments and the bare DNA to an external force could be followed simultaneously using fluorescence microscopy and the position detection of trapped beads, allowing the authors to extract the rheological properties of each component from a measurement of the heterogeneous system [17]. This experiment was one example for the demonstration of

potential application of combining optical tweezers with fluorescence measurement, demarcating different parts of a large molecule and measure the response of each part with respect to an externally applied force. Recently, a combination of optical tweezers, fluorescence microscopy, and microfluidics was used to visualize the structural changes of an individual DNA undergoing the overstretching transition [18].

However, the combination of single-molecule fluorescence measurements with optical tweezers force and displacement measurements has slowed down, owing to various technical problems. The biggest hindrance being the lifetime of the fluorescent dyes that decreases dramatically when a near-infrared trapping photon is absorbed by the fluorescent excited state [19]. This effect could be avoided in the study just described, as actin's high value of stiffness allowed the investigators to use long filaments, thus the region of interest where single fluorophores were imaged could be separated by the position of the optical traps by about 10 μm . The detection of molecular motions, unfortunately, is greatly hindered by more flexible polymers, such as dsDNA, of this length because the stiffness of the tether decreases with increased length and lower stiffness degrades resolution. Nevertheless, at that moment it was possible to measure and apply force with the optical trap on only long pieces of DNA. Another issue with fluorescence is that it can be used only to observe strong topological changes [20].

Unlike the previous studies, in this thesis we follow a different technique to detect the response of the molecular complexes of DNA or a cell to an applied mechanical load - the Raman spectroscopy. This approach is more challenging because of inherently low efficiency of the Raman spectroscopy, however, it provides a more detailed information regarding different parts of molecular complexes that fluorescence can offer. Raman spectroscopy is a label free technique and consequently can be used with a sample in *pure* state. Additionally, there is no bleaching effect in case of Raman spectroscopy. Raman spectroscopy has proved to be an important characterization tool for biological systems. Raman fingerprint of a biological cell can yield a vast amount of information about the cell's structural makeup and chemical changes, and can even be used as a form of cell identification or imaging. The typical powers and wavelengths for trapping and Raman excitation of living cells are below the lower limits of cell heating and photodegradation, as further exemplified by demonstrations of the proliferation of a cell in an optical trap [14, 21, 22].

As can be seen from fig. 3, microrheology (gray color) has developed gradually in the last fifteen years. Up to the year 2004, this technique was not implemented to a great extent in the study of cells or DNA (red color). But after 2004, a major portion of publications on microrheology involved measurements of cells or DNA. The blue color shows the use of word fluorescence or Raman along with microrheology for cells or DNA. We can see that till now not much work has been done to combine mechanical and optical spectra to get overall information on biomolecules.

As Raman has very low efficiency, there is a need to use some enhancement techniques combined with statistical analysis to generate meaningful information from the experimental data. Surface enhanced Raman spectroscopy (SERS) has proved to be an useful tool for the enhancement of Raman signal. It is a surface sensitive technique that amplifies Raman signal of molecules adsorbed on rough metal surfaces through local surface plasmons. The enhancement factor can be as much as $10^{10} - 10^{11}$ and thus it can be used to resolve the structure

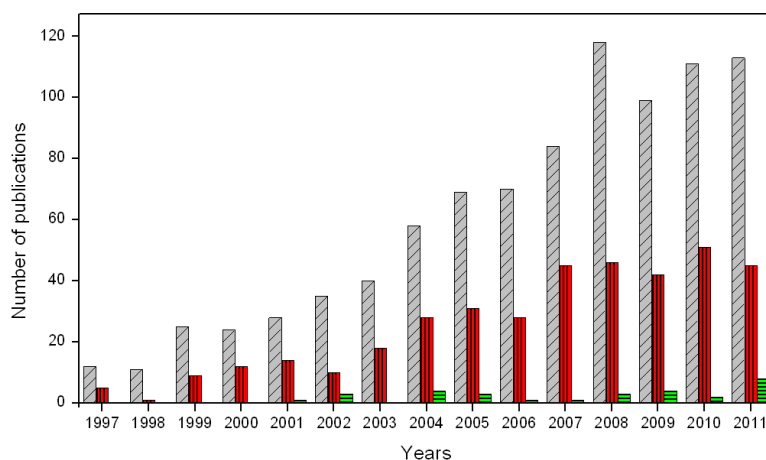


Figure 3: Number of papers published in past 15 years with words - microrheology (gray color, slanted lines), microrheology and cells or DNA (red color, vertical lines), microrheology and cells or DNA and Raman or fluorescence (green color, horizontal lines) - in abstract, title or body of a paper, as shown by ISI web of knowledge.

even at single molecule level [15, 23]. We have used this approach in order to obtain Raman signal from single DNA molecule in physiological conditions.

Thus the main goal of this thesis is, on the basis of experimental data for two important biological samples - Red Blood Cells and DNA - obtained by combining force measurements with spectroscopic Raman technique, to unravel the connection between rheological properties and molecular structure. This sort of approach is best suited for studying single biomolecules as it gives an in-depth understanding of how the molecular bondings change on the application of mechanical force.

Using above methodology, we have studied the mechanical properties of DNA and RBC and tried to relate these properties with molecular changes using Raman spectroscopy. We were able to show for the first time, the Raman signal from single DNA molecule in physiological condition in relaxed and various stretched state in entropic regime [24]. When DNA is extended in entropic force regime, it is a widely accepted view that entropic forces are simply balanced by lowering DNA entropy via unfolding as the molecule is extended. In addition, we also observed some molecular rearrangement for phosphate backbone. Our results were supported by theoretical calculations performed by our collaborators in supercomputing center in Barcelona. These results will open a new window in understanding the mechanism of DNA at low forces.

For getting the mechanical response, we used passive microrheology on RBC and DNA. Frequency dependent response function and stiffness was obtained for both of them. They showed a similar trend for real part of complex stiffness - increase with the applied force, but the cross-correlation spectrum showed different behavior.

We have used Raman spectroscopy to understand the stretching and relaxation that RBCs experience as they pass through vessels and smaller capillaries

inside human body. The results show a strong dependence of intensity of certain bands on the deformation (stretching) applied to the cell. Furthermore, we observed slight changes in the width and position of certain bands. Most of the peaks showed a saturation and slight relaxation in the intensity changes. This effect tentatively confirms the nonlinearity that we observed in the mechanical response of RBC using passive microrheology [25]. The Raman spectra obtained from RBC is highly complex in nature. We utilized statistical techniques to gain an in-depth understanding of spectral changes with stretching [26].

The organization of this thesis is as follows: following this introduction, **first chapter** discusses the development and working of optical tweezers technique. **Chapter two** discusses the theory of Raman spectroscopy and its comparison with other equally competitive techniques. Some of the signal enhancement techniques are also discussed in this chapter. **Chapter three** discusses microrheology and the theoretical backbone behind such measurements. **Chapter four** highlights the experimental set-ups that I developed and used during thesis period. This chapter also contains a section regarding methods and materials, where I discuss briefly about 2D correlation and principal component analysis (PCA) along with various biochemical protocols that were necessary for preparing functionalized beads, various SERS substrates and proper handling of biomolecules. **Chapter five** discusses results on the measurement of Raman signal from single DNA molecule in physiological conditions. **Chapter six** is an extension of chapter five and discusses the results of Raman spectra of DNA at various forces under entropic regime. **Chapter seven** is about combining microrheology technique with Raman spectroscopy for RBC. Raman spectroscopy of RBC is discussed in detail in **chapter eight**. This chapter also discusses in detail the importance of multivariate analysis and 2D correlation spectroscopy in order to understand a complex set of spectra. In **chapter nine**, microrheology of single DNA molecule is presented. Finally the **last chapter** concludes the essence of all the work conducted for the completion of this project. The list of publications is given at the end of the thesis.

1

Optical Tweezers

Since the advent of optical trapping in 1970 by Ashkin, the study of single molecule physics has been revolutionized. Although this technique is relatively new, the physics behind optical trapping has been known for a long time. The German astronomer Johannes Kepler was first to mention about radiation forces in his manuscript *De Cometis* of 1619, where he mentioned that the comet's tail point away from the sun because of some "solar breeze". He even proposed the idea of exploring the galaxy in sails pushed by these solar breeze. Two centuries later, Maxwell confirmed in his theory of electromagnetism that light can exert an optical force (or radiation pressure) on matter. The onset of lasers in 1960 gave impetus to experimental studies of radiation forces. In ten years, from the time of arrival of first laser, Ashkin was able to show that motion of polystyrene microspheres can be confined using radiation forces [27].

In 1986, Ashkin and coworkers demonstrated the first stable three dimensional optical trap, or optical tweezers, created using optical forces from a single laser beam [28]. Soon after he showed the potential of this technique in single biomolecule studies by trapping and manipulating single viruses and bacteria [29]. Since then, the usage of optical tweezers has grown leaps and bounds in the experimental studies of single molecule biophysics.

1.1 Working principle

Optical tweezers are based on the basic observation that photons have a momentum $p = h/\lambda$, with h being Planck's constant and λ is the wavelength of light. Hence, a change in momentum of the photons will result in optical force. This force go unnoticed on macroscopic objects, but can play a vital role on micro- or mesoscopic objects, such as polystyrene microspheres and biomolecules, when a focused laser beam is incident on it.

Optical forces that play a decisive role in the working of optical tweezers are *the scattering force* and *the gradient force*. Scattering force is as a result of

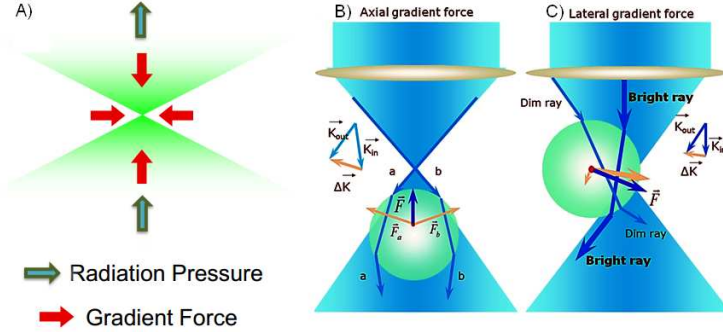


Figure 1.1: Qualitative view of the origin of the trapping force. Part A: shows the directions in which gradient force and radiation pressure acts. Part B: shows the axial gradient force acting towards the focus of the trapping beam. Part C: shows the lateral gradient force of a non-uniformly distributed laser beam.

photons that are absorbed or scattered by an object in its path and it is always in the direction of the incident beam. Gradient force is in the direction of larger light intensity. Therefore for a focused laser beam in an aqueous suspension of particles with a higher refractive index than water, the gradient force will direct a particle to the point with the highest intensity, i.e., the center of the focus. For a stable trap the gradient force, which is dependent upon the numerical aperture (NA) of the objective, should be greater than the scattering force. The equilibrium position of the trapped particle is slightly *off focus* due to the scattering force.

The optical forces are demonstrated in fig. 1.1. First image (fig. 1.1-A) gives an idea of scattering force and gradient forces in a focused beam. The other two figures depict forces on a transparent dielectric sphere, with refractive index higher than the medium, near the beam focus. Refraction of light from the dielectric sphere will cause a change in beam direction and consequently result in the change in momentum. This change in momentum will lead to optical forces on the sphere. In fig. 1.1-B, the optical force acting on the sphere is described as a combination of rays *a* and *b*. If reflection from surface is considered as zero, then the forces F_a and F_b pointing in the direction of momentum change, are entirely due to refraction. It can be seen that for small displacements of sphere from beam focus net restoring force is always directed back to focus, hence describing a stable gradient force in axial direction. For lateral direction, the momentum change between *bright* and *dim* ray can be seen to cause a net force in the direction of high intensity (fig. 1.1-C). Ashkin has discussed in details the theory of optical tweezers in ray optics regime in [30].

The theoretical model for trapping has been developed depending on the size of the object. Mie or ray optics regime is referred when the diameter of the trapped object is significantly greater than the wavelength of light ($d \gg \lambda$). The effect of diffraction can be neglected in this case and the optical forces can be understood using ray optics. In cases where the diameter of a trapped particle is much smaller than the wavelength of light ($d \ll \lambda$), one needs a model based on electromagnetic dipoles. This regime is called the Rayleigh regime. For

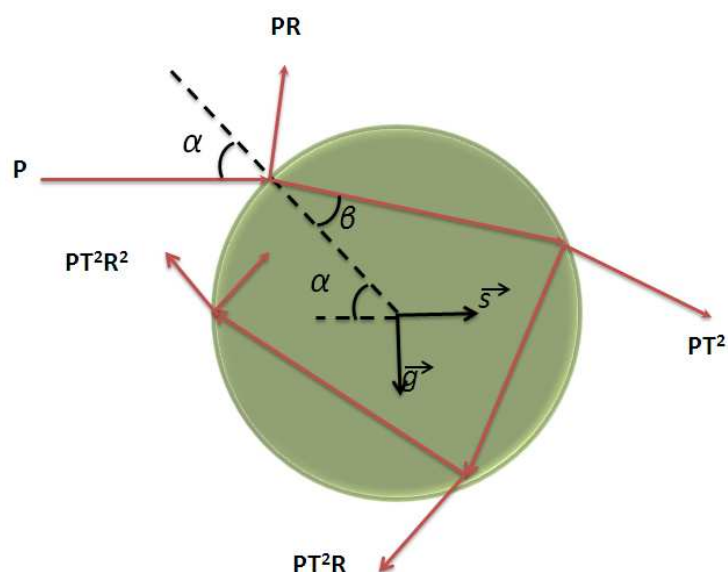


Figure 1.2: Schematic description of force calculation in ray optics regime.

particles comparable to the wavelength of light ($d \approx \lambda$), a complex approach is required to describe trapping. For this case, the dimensions of the focus cannot be neglected and the problem is usually solved by using electromagnetic theory. To derive trapping forces, the vector character of the laser's electromagnetic field has to be accounted for and Maxwell's equations for the appropriate boundary value problem needs to be solved.

1.1.1 Ray optics approach

When the diameter of the trapped object is much larger than the wavelength of the trapping beam ($d \gg \lambda$), the forces on the particle can be described using ray optics [30]. When a beam of light traveling in a medium with refractive index n_1 , impinges on a dielectric sphere with refractive index n_2 , it is refracted according to Snell's law. The beam is again refracted as it leaves the particle. The momentum of the light ray is changed because of the refraction by the particle. According to the law of conservation of momentum, this change of momentum is transferred to the particle and the particle experiences optical forces.

A light beam can be explained as a collection of rays with varying intensities. Total optical force on a particle is as a result of summation of forces from all the rays. Suppose a single ray of light with power P hits a dielectric sphere at an angle of incidence α . Its incident momentum per second can be described as $n_1 P/c$, where c is the velocity of light in vacuum (fig. 1.2). The total force on the sphere is the sum of contributions due to the infinite number of refracted rays with decreasing power PT^2 , PT^2R , ... PT^2R^n and the reflected ray of power PR . R and T are the Fresnel reflection and transmission coefficients at

angle α . The net force acting through the origin can be broken into scattering force (F_s) and gradient force (F_g) as:

$$F_s = \frac{n_1 P}{c} \left[1 + R \cos 2\alpha - \frac{T^2 \{ \cos(2\alpha - 2\beta) + R \cos 2\alpha \}}{1 + R^2 + 2R \cos 2\beta} \right], \quad (1.1a)$$

$$F_g = \frac{n_1 P}{c} \left[R \sin 2\alpha - \frac{T^2 \{ \sin(2\alpha - 2\beta) + R \sin 2\alpha \}}{1 + R^2 + 2R \cos 2\beta} \right], \quad (1.1b)$$

where α and β are the angles of incidence and refraction respectively. As R and T depends the polarization of light, hence scattering force and gradient force are polarization dependent.

The vector sum of these two force components gives the total force due to a single optical ray of power P . The total force exerted on the object can be found by summing over all rays passing through it [30].

1.1.2 Rayleigh regime

When the diameter of the trapped object is significantly smaller than the wavelength of the trapping beam ($d \ll \lambda$), the optical forces can be calculated on the particle by treating it as an induced point dipole which scatters light elastically.

A scattering force is exerted on the induced dipole as it absorbs and radiates the incident light. The scattering force is proportional to the intensity of light and is directed towards the propagation of the beam. The scattering force can be described by the following equation [31]:

$$F_s = n_m \frac{\langle S \rangle \sigma_{scatt}}{c}, \quad (1.2)$$

where,

$$\sigma_{scatt} = \frac{8}{3} \pi (\bar{\nu} r)^4 r^2 \left(\frac{m^2 - 1}{m^2 + 2} \right)^2, \quad (1.3)$$

is the scattering cross section of a sphere with radius r [32]. The quantity n and n_m are the sphere and medium refractive index respectively, $m = n/n_m$ is the relative index, $\bar{\nu} = 2\pi n_m/\lambda$ is the wavenumber of the light and $\langle S \rangle$ is the average Poynting vector.

The particle experiences a force in the direction of gradient of the electromagnetic field as it is polarized by the laser beam. The gradient force is proportional to the gradient field intensity and is directed towards the intensity gradient [29]. The gradient force can be calculated using following equation [31]:

$$F_g = \frac{\wp}{2} \nabla \langle E^2 \rangle, \quad (1.4)$$

where \wp is the polarizability of the particle:

$$\wp = n_m^2 r^3 \left(\frac{m^2 - 1}{m^2 + 2} \right). \quad (1.5)$$

Thus, a particle with a large dielectric constant within the laser beam will exert a force, which is directed toward the focus of the beam. Thus, a particle can be trapped and manipulated by moving the focus of the beam.

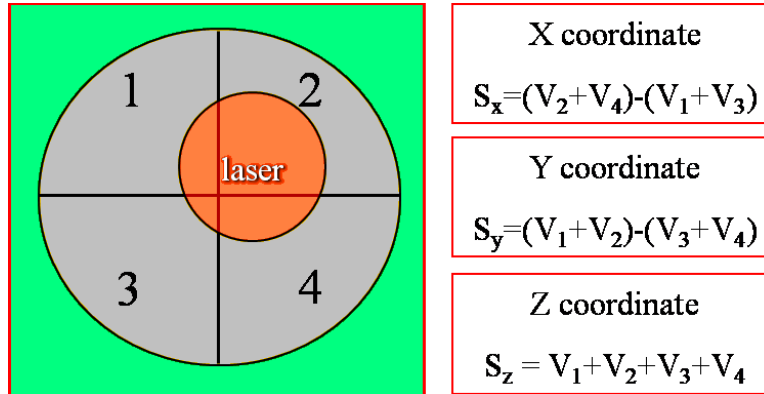


Figure 1.3: Working principal of a quadrant photodiode. The back focal plane of the condenser is imaged onto a QPD and the x , y and z position are determined from the signals of the four individual segments of the QPD.

For particles with size comparable to wavelength of light ($d \approx \lambda$), electromagnetic approach is used for theoretical calculations of trapping phenomena. This is the region of most interest as most of the particles and molecules under study fall into this regime. Diffraction effects become important for particles in this case. Moreover, we cannot neglect the vector nature of the electromagnetic field for a highly focused laser beam. Due to the above mentioned factors, it becomes increasingly difficult to calculate forces in this regime. Mazolli *et al.* outlined a detailed theory for force exerted on a dielectric sphere of arbitrary radius and refractive index from Debye-type integral for a laser beam focused through a high numerical aperture objective [33].

1.2 Trap calibration

If the purpose of optical tweezers is just to trap and move microscopic objects, then the set-up need not be calibrated. But for high precision force measurement and position tracking, it is pertinent that we calibrate the set-up. In this thesis, single molecule force spectroscopy has been studied on biomolecules and cells, hence accurate knowledge of position and force is very important. There are various ways in which an optical tweezers set-up can be calibrated [34,35]. Three of the most widely used techniques are:

- **Video based particle tracking:** This method involves extracting the pixel position from successive frames of an object in course of motion [36]. The difference in pixel positions in combination with pixel to nanometer conversion gives quantitative movement of the trapped object. The pixel to nm conversion factor can be resolved by knowing precisely the movements of an object or by using a ruled microscope slide. Though this technique is capable of video position detection, it is not used much because of very slow response time as compared to a quadrant photodiode (QPD).

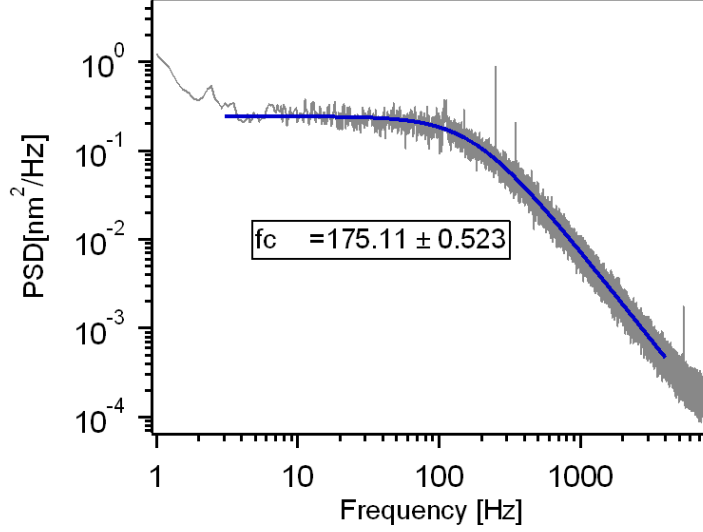


Figure 1.4: An example of power spectral density of the position of a trapped polystyrene bead in water. The measurement was done for two minutes on a $3 \mu\text{m}$ bead at 20 kHz acquisition rate and the data averaged for every 26 seconds. Solid line represents the Lorentzian fit of the PSD and is used to generate corner frequency (f_c) in order to determine the trap stiffness.

- **Viscous drag method:** In this technique, a trapped bead is subjected to a constant flow and its displacement from the trap center is measured with the help of a QPD. At equilibrium, trapping force and drag force will be equal and hence the stiffness of the trap can be calculated:

$$kx = 6\pi\eta rv, \quad (1.6)$$

where, k is trap stiffness, η is viscosity of the fluid medium, r is bead's radius and v is fluid velocity. Flow in the chamber can be induced either by moving the stage at a constant velocity or by injecting the sample in the flow cell with a high precision pump. Voltage to nanometer conversion for QPD can be obtained by immobilizing the bead on the surface and moving it with known step and measuring the response on the QPD. Although this method is a fast and accurate way to do calibration, it is limited by the accurate and automated movement of the stage which can be a costly part of system design.

- **Power spectral density method:** This method extracts voltage to nanometer conversion of the QPD directly from the power spectral density of a trapped bead [37]. This technique is relatively straightforward and hence, we have used this method for trap calibration.

To measure the signal from the motion of trapped particle, one of the most commonly used technique is *back-focal-plane interferometry* [38, 39]. According to this technique, far-field interference of the outgoing laser light with the

scattered light from the trapped particle can describe the intensity shifts due to the lateral displacement of the particle. The transmitted and scattered light is collimated by a condenser lens of focal length f . In the back focal plane of condenser, the intensity distribution does not change when moving the optical trap around in the sample, but it is affected by the motion of the trapped object with respect to the trap. For this reason, the back focal plane of condenser is imaged onto a quadrant photodiode (QPD). A QPD is a 2×2 array of individual photodiode active areas integrated on a single chip. Each of these areas behave as an independent detector whose signal, V_i ($i = 1, \dots, 4$), depends on the amount of light. The QPD can be decoupled into three different signals S_x , S_y and S_z which are linear combinations of those four voltages (fig. 1.3):

$$\begin{aligned} S_x &= V_2 + V_4 - (V_1 + V_3) \\ S_y &= V_1 + V_2 - (V_3 + V_4) \\ S_z &= V_1 + V_2 + V_3 + V_4 \end{aligned}$$

A trapped bead will feel both diffusional forces and restoring optical force in a viscous fluid. Assuming the confining force to be linear in the displacement with a proportionality constant k_x , the Langevin equation of the bead's motion can be written as:

$$\beta \frac{dx}{dt} + k_x x = f_R(t), \quad (1.7)$$

where $f_R(t)$ is the random thermal force which averages to zero over time and β is the viscous drag coefficient of the medium. The power spectral density (PSD) can be calculated by taking the Fourier transform of eq. (1.7):

$$C_x(f) = \frac{k_B T}{\beta \pi^2 (f_c^2 + f^2)}, \quad (1.8)$$

where k_B is Boltzmann's constant, T is the temperature and $f_c = k_x/2\pi\beta$ is called the corner frequency. The PSD of a particle under Brownian motion has a Lorentzian profile and hence by fitting the PSD obtained by Lorentzian, one can obtain the value of f_c and consequently determine the trap stiffness (fig. 1.4). From the equipartition of energy, we can write:

$$\frac{1}{2} k_B T = \frac{1}{2} k_x \langle x^2 \rangle, \quad (1.9)$$

So by comparing the value of variance, $\langle x^2 \rangle$, from eq. (1.9) and the one obtained from QPD, we can obtain the voltage to nanometer conversion factor.

2

Raman spectroscopy

When a monochromatic light of frequency ν_0 is incident on a molecule then it can go through absorption, transmission or scattering. Most of the scattered light has the same frequency as that of incident light (Rayleigh scattering). However, a small fraction of the light (approximately 1 in 10^7 photons) can undergo scattering at optical frequencies lower (Stokes scattering) or higher (anti-Stokes scattering) than the frequency of the incident photons. The process leading to this inelastic scattering is termed as Raman effect.

The effect of Raman scattering was reported first by an Indian Physicist C. V. Raman in 1928 [40]. By monitoring the light scattering from various crystalline and amorphous solids, fluids and gases with a mercury arc lamp, Raman succeeded to distinguish elastic scattering from additional spectral bands. He described these findings as a "spectrum of the new radiation", and deemed it as a result of energy exchange between the incident light and the scattering medium. Raman received the Nobel prize in 1930 for his work. The introduction of the laser in the 1960s allowed Raman spectroscopy to be more accessible to the scientific community. In the mid 1990's, the next generation of smaller, more compact instruments started to evolve. They utilized newer lasers, optics and detectors and began the micro Raman revolution [41, 42].

Applications based on Raman spectroscopy offers some major advantages in comparison with other analytical techniques. Raman is based on scattering of light, so all that is required for obtaining a spectrum is to place the sample into the excitation beam and collect the scattered light. There are little concerns regarding sample thickness and negligible interference from the ambient atmosphere, so there is no need for high-vacuum or desiccated sample holders. Water, glass and plastic have weak Raman spectra, making the technique even easier to use. Samples can be analyzed directly inside a plastic bag or glass bottle without having to open the package and risk contamination. Aqueous samples can be readily analyzed without a need to remove water, and as there is no interference from ambient humidity, there is no need to cleanup the instrument.

A rationale behind the belief that vibrational spectroscopy may be useful to

diagnose diseases or pathologies in individuals is that disease processes must, generally speaking, be accompanied by changes in the chemistry/biochemistry of cells, tissues, organs, or body fluids, and vibrational spectroscopy is indeed ideally suited for sensitive detection of such changes as a diagnostic technique. Given the fact that sample preparation and measurement are very simple and collection times are in the range of seconds or minutes, IR and Raman spectroscopy should be ideal modalities to establish very rapid non-subjective and cost-effective tools for early diagnosis of disease processes in individuals.

Biomedical IR and Raman spectroscopy probe biological samples in a way that the active vibrational modes of all constituents present in the mixture are observed in a single experiment, resulting in very complex spectra with superimposed spectral features throughout the whole spectral range. On the other hand techniques such as fluorescence, gas chromatography, UV-VIS spectroscopy, HPLC analysis etc can analyze only part of the chemical composition. Furthermore, these techniques usually require complex sample pretreatment steps and are often destructive, while Raman spectroscopy is non-destructive. This makes Raman spectroscopy ideal for investigating structural conformation of biomolecules in physiological condition. The lack of sample preparation also minimizes the possibility of cross-contamination.

Both Raman and IR spectroscopy are due to molecular vibrations. However, as Raman spectra are mainly composed of narrow bands, spectral analysis is simplified compared to infrared spectroscopy. In addition, low vibrational modes are generally not observable through infrared spectroscopy and samples can be mounted in a glass container during Raman spectroscopy, which is not possible with infrared spectroscopy. Raman spectroscopy is insensitive to interference of water, so where strong interference from water absorption occurs, Raman spectroscopy is preferred over IR spectroscopy. The spatial resolution that can be obtained by vibrational spectroscopy is dependent on the wavelength used: where a spatial resolution of several micrometers can be obtained by infrared spectroscopy, Raman spectroscopy is able to analyze a sample at sub-micrometer resolution by choosing an appropriate laser wavelength. In this way, individual cellular components can be analyzed, which is not possible with IR spectroscopy. In addition, IR spectroscopy requires a tunable source of light, thus increasing the technical complexity of the system. In comparison, Raman spectroscopy is much simpler as it needs a monochromatic source of light.

Raman spectra of no two molecules are similar and the intensity depends upon the quantity of material present. Thus Raman spectroscopy provides both qualitative and quantitative information about the sample, allowing for spectral interpretation, data manipulation, library searching and the application of chemometric methods.

Raman spectroscopy also has various additional advantages. Unlike other vibrational techniques, its operational wavelength range is usually independent of the vibrational modes being studied. Since Raman spectroscopy measures the shift in frequency from that of the excitation laser, it can be performed using any operating range from UV to NIR. It thus permits access to vibrational mode information normally associated with wavelengths ranging from 2 - 200 μm .

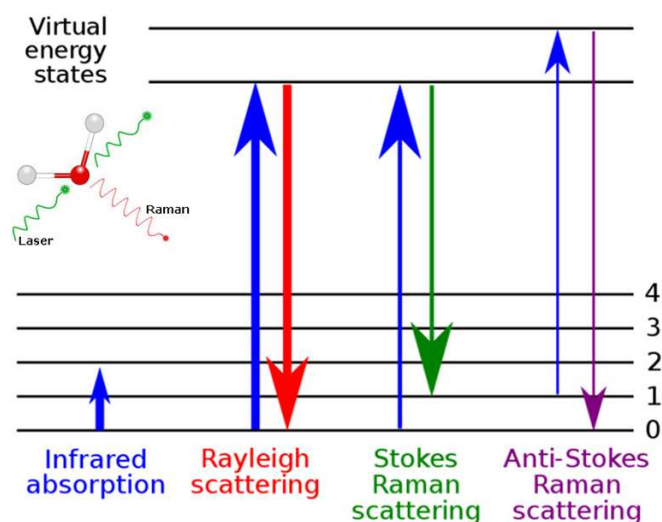


Figure 2.1: Schematic diagram of Raman scattering by molecules.

2.0.1 Classical theory of Raman scattering.

Raman effect occurs when light strikes upon a molecule and interacts with the electron cloud formed by the bonds of that molecule. The incident photon excites one of the electrons into a virtual state. For the spontaneous Raman effect, the molecule will be excited from the ground state to a virtual energy state, and relax into a vibrational excited state, which generates the Stokes Raman scattering. If the molecule is already in an elevated vibrational energy state, the Raman scattering is then called anti-Stokes Raman scattering. A simplified energy diagram that illustrates these concepts is shown in fig. 2.1. Stokes radiation occurs at lower energy (longer wavelength) as compared to the Rayleigh radiation, and anti-Stokes radiation has higher energy. The energy increase or decrease is related to the vibrational energy levels in the ground electronic state of the molecule, and, the observed Raman shift of Stokes and anti-Stokes features are a direct measure of the vibrational energies of the molecule.

When a molecule is introduced into an electric field \vec{E} , an electric dipole moment \vec{P} is induced in the molecule (see fig. 2.2). If α is the polarizability of the molecule, then the induced dipole moment is given by:

$$\vec{P} = \alpha \vec{E}. \quad (2.1)$$

When electromagnetic radiation of frequency ω_0 falls on the molecule, this introduces a varying electric field \vec{E} whose dependence on the time t is given by:

$$\vec{E} = \vec{E}_0 \cos \omega_0 t, \quad (2.2)$$

where \vec{E}_0 is amplitude of the electric field. Hence, from equations (2.1) and (2.2):

$$\vec{P} = \alpha \vec{E}_0 \cos \omega_0 t. \quad (2.3)$$

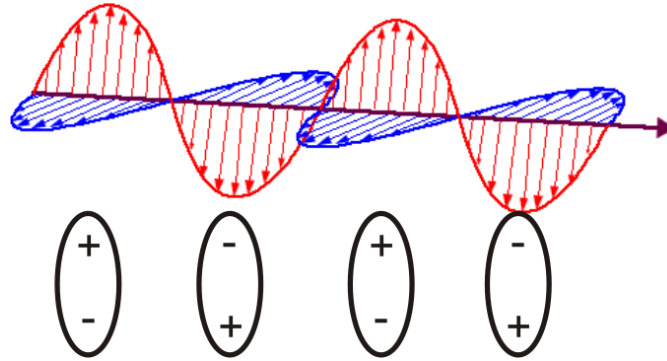


Figure 2.2: Oscillation of an induced dipole in an electric-magnetic field.

Such an oscillating dipole emits radiation of its own oscillation with a frequency ω_0 , giving the Rayleigh scattered beam.

For an isotropic medium, \vec{P} and \vec{E} are both in the same direction and polarizability (α) of the molecule is scalar. However, for non-isotropic molecules the application of an electric field in a fixed direction induces a dipole moment in different direction, and α becomes a tensor. In general, molecules are non-isotropic, and the three equations which take account of the unequal polarizability along different principal axes of the molecule are:

$$P_x = \alpha_{xx}E_x + \alpha_{xy}E_y + \alpha_{xz}E_z, \quad (2.4a)$$

$$P_y = \alpha_{yx}E_x + \alpha_{yy}E_y + \alpha_{yz}E_z, \quad (2.4b)$$

$$P_z = \alpha_{zx}E_x + \alpha_{zy}E_y + \alpha_{zz}E_z, \quad (2.4c)$$

where P_x , P_y and P_z are the induced electric dipole moment in x, y and z directions, respectively. The tensor α is defined by nine coefficients $\alpha_{xx}, \alpha_{xy}, \dots, \alpha_{zz}$. However, $\alpha_{xy} = \alpha_{yx}$, $\alpha_{yz} = \alpha_{zy}$ and $\alpha_{xz} = \alpha_{zx}$, hence the tensor α is really defined by six coefficients. If any of these six polarizability coefficients changes during a rotation or a vibration, then the theoretical criterion for a Raman spectrum is satisfied. If, however, the polarizability varies slightly with molecular vibration, we can write:

$$\alpha = \alpha_0 + \left(\frac{\partial \alpha}{\partial q} \right)_0 q_0 + \dots, \quad (2.5)$$

Here, q describes the molecular vibration, α_0 is polarizability at the equilibrium position, and $(\partial \alpha / \partial q)_0$ is the rate of change of α with respect to the change in q , evaluated at the equilibrium position. Equation (2.5) holds for α in each of the six coefficients for polarizability. We can write q as:

$$q = q_0 \cos(\omega_m t), \quad (2.6)$$

where q_0 is the amplitude of the molecular vibration and ω_m is molecular frequency. Substituting eq. (2.2) in eq. (2.4a) we get:

$$P_x = (\alpha_{xx}E_x^0 + \alpha_{xy}E_y^0 + \alpha_{xz}E_z^0) \cos \omega_0 t. \quad (2.7)$$

Taking α from eq. (2.5) and q from eq. (2.6) the following expression is obtained:

$$\begin{aligned}
 P_x &= (\alpha_{xx}^0 E_x^0 + \alpha_{xy}^0 E_y^0 + \alpha_{xz}^0 E_z^0) \cos \omega_0 t \\
 &+ \left\{ \left(\frac{\partial \alpha_{xx}}{\partial q} \right)_0 E_x^0 + \left(\frac{\partial \alpha_{xy}}{\partial q} \right)_0 E_y^0 + \left(\frac{\partial \alpha_{xz}}{\partial q} \right)_0 E_z^0 \right\} \\
 &q_0 \cos \omega_0 t \cos \omega_m t + \dots
 \end{aligned} \tag{2.8}$$

Eq. (2.8) can be readily transformed into:

$$\begin{aligned}
 P_x &= (\alpha_{xx}^0 E_x^0 + \alpha_{xy}^0 E_y^0 + \alpha_{xz}^0 E_z^0) \cos \omega_0 t \\
 &+ \frac{q_0}{2} \left\{ \left(\frac{\partial \alpha_{xx}}{\partial q} \right)_0 E_x^0 + \left(\frac{\partial \alpha_{xy}}{\partial q} \right)_0 E_y^0 + \left(\frac{\partial \alpha_{xz}}{\partial q} \right)_0 E_z^0 \right\} \\
 &\{ \cos(\omega_0 + \omega_m)t + \cos(\omega_0 - \omega_m)t \}.
 \end{aligned} \tag{2.9}$$

The first term of eq. (2.8) contains only one frequency factor ω_0 , that is the one of the incident radiation. This term is interpreted in terms of the *Rayleigh scattering*. In addition to the incident frequency, the second term contains the frequencies $\omega_0 \pm \omega_m$. Thus, the induced dipole moment can also oscillate with two frequencies $\omega_0 \pm \omega_m$, interpreted as the vibrational frequencies. The $\omega_0 - \omega_m$ and $\omega_0 + \omega_m$ frequencies correspond to the *Stokes* and *anti-Stokes* lines respectively.

According to eq. (2.8), α_0 in the first term determines the properties of Rayleigh scattering, while $(\partial\alpha/\partial q)_0$ in the second term determines the properties of the Raman scattering. In fact, it is clear that if $(\partial\alpha/\partial q)_0$ equals zero, so do the Stokes and anti-Stokes terms and there will be no Raman scattering. This gives a selection rule for the Raman-active transitions: for a vibration to be Raman active, the polarizability of the molecule must change with the vibrational motion.

2.0.2 Quantum theory of Raman scattering.

The Stokes scattering generally is observed to give a stronger signal than anti-Stokes scattering. This is in disagreement with equation (2.8) (which predicts equal intensities for both processes) and is the most obvious indication of the breakdown of the classical picture.

This problem can be solved by quantum-mechanical theory of Raman scattering. In the quantum picture, the molecular vibrations are quantized. The scattering process is viewed as the creation and annihilation of vibrational excitations by photons. Incoming beam raises the system to an excited electronic state (this may be a virtual state or, in the case of resonant Raman scattering, a real electronic state) from which return to a different vibrational level of the electronic ground state may be possible. Stokes scattering involves loss in energy of the incident photon and thus the system returns to a state with a higher vibrational quantum number.

The expectation value of the component α_{ij} of the polarizability tensor is given by:

$$\langle \alpha_{ij} \rangle = \int u_b^*(q) \alpha_{ij} u_a(q) dq, \tag{2.10}$$

where the function $u(q)$ represent the molecular eigenfunctions in the initial level a and the final level b . The integration extends over all nuclear coordinates. This shows that a computation of the intensities of Raman lines is based on the knowledge of the molecular wave function of the initial and final states.

For small displacement q_n the molecular potential can be approximated by a harmonic potential, where the coupling between the different vibrational modes can be neglected. The functions $u(q)$ are then separable into a product:

$$u(q) = \prod_{n=1}^Q w_n(q_n, v_n), \quad (2.11)$$

of vibrational eigenfunction of the n^{th} normal mode with v_n vibrational quanta, where $Q=3N-6$ (or $3N-5$ for linear molecules) gives the number of normal vibrational mode for N nuclei. Using the orthogonality relation:

$$\int w_n w_m dq = \delta_{nm}, \quad (2.12)$$

of the functions $w_n(q_n)$, one obtains from eq. (2.10) and eq. (2.5):

$$\langle \alpha_{ij} \rangle_{ab} = \alpha_{ij}^0 + \sum_{n=1}^Q \left(\frac{\partial \alpha_{ij}}{\partial q_n} \right)_0 \int w_n(q_n, v_a) q_n w_n(q_n, v_b) dq_n. \quad (2.13)$$

The first term is a constant and responsible of the Rayleigh scattering. For non-degenerate vibrations the integrals in the second term vanish unless $v_a = v_b \pm 1$. In this case its value is $[\frac{1}{2}(v_a+1)]^{1/2}$. The intensity parameter of the vibrational Raman spectroscopy is the derivative $(\partial \alpha_{ij} / \partial q)$, which can be determined from the Raman spectra.

The intensity of a Raman line at a Stokes or anti-Stokes frequency ($\omega_0 \pm \omega_n$) is determined by the population intensity $N_i(E_i)$ in the initial level E_i , by the intensity I_L of the incident pump laser, and by the Raman scattering cross section $\sigma_R(i \rightarrow f)$ for the Raman transition $E_i \rightarrow E_f$:

$$I_{Raman} = N_i(E_i) \sigma_R(i \rightarrow f) I_L. \quad (2.14)$$

The population density, $N_i(E_i)$, follows Boltzmann distribution at thermal equilibrium:

$$N_i(E_i) = \frac{N}{Z} g_i e^{-E_i/kT}, \quad (2.15)$$

where $N = \sum N_i$, the partition function $Z = \sum g_i e^{-E_i/kT}$, and g_i is the number of degenerate microstates which have the same energy level.

In the case of the Stokes radiation, the initial state of the molecules may be the vibrational ground state, while for the emission of anti-Stokes lines the molecules should have initial excitation energy. Due to the lower population density in these excited levels, the intensity of the anti-Stokes lines is lower by a factor:

$$\frac{I_{Stokes}}{I_{anti-Stokes}} = e^{(-\hbar\omega_n/kT)}. \quad (2.16)$$

The scattering cross section depends on the matrix element of the polarizability tensor [eq. (2.13)] and contains furthermore the ω^4 frequency dependence, and

it can be written as follow [80]:

$$\sigma_R(i \rightarrow f) = \frac{8\pi\omega_s^4}{9\hbar c^4} \left| \sum_j \frac{\langle \alpha_{ij} \rangle \hat{e}_L \langle \alpha_{jf} \rangle \hat{e}_S}{(\omega_{ij} - \omega_L - i\gamma_j)} + \frac{\langle \alpha_{ji} \rangle \hat{e}_L \langle \alpha_{jf} \rangle \hat{e}_S}{(\omega_{jf} - \omega_L - i\gamma_j)} \right|^2, \quad (2.17)$$

where \hat{e}_L and \hat{e}_S are the unit vectors representing the polarization of the incident and the scattered beam respectively. The sum extends over all molecular levels j with homogeneous width γ_j accessible by single-photon transitions from the initial state i . We see from eq. (2.17) that the initial and the final states are connected by two-photon transitions which implies that both states have the same parity. For example, the vibrational transitions in homo-nuclear diatomic molecules, which are forbidden for single-photon infrared transition, are accessible to Raman transitions.

Raman scattering is a relatively weak process (typical cross section of $10^{-30} - 10^{-25} \text{ cm}^2/\text{molecule}$). The number of photons Raman scattered is quite small. However there are several processes which can be used to enhance the sensitivity of a Raman measurement.

2.0.3 Resonance Raman scattering

On inspection of eq. (2.17), we find that cross-section of Raman scattering increases substantially as the laser frequency ω_L approaches the molecular transition frequency ω_{ij} . This enhancement in Raman spectra is termed as *resonance Raman spectroscopy*. It has shown that Resonance of laser with certain molecular vibration can lead to an enhancement of the order $10^2 - 10^4$ [43, 44].

So, in resonance Raman scattering, the molecule is excited near one of the electronic transition level as opposed to normal Raman scattering where we need to excite the molecule to a virtual state. Raman signal from this particular transition is enhanced as compared to other Raman bands. Hence if we want to explore more than one transition, we need to use a tunable laser source. The technique becomes even more complicated when the electronic transition is UV/visible region, as is the case with most of the molecules. First problem with UV/visible wavelength is that Raman signal might be accompanied by huge fluorescence background which will lead to difficulty in analysis of Raman bands. Another issue, mainly associated with biomolecules, is that the light at these wavelengths can leads to photo-degradation of the molecules under long period of measurements.

Nevertheless, resonance Raman technique is very helpful if we are interested in analyzing specific molecule from a very complex material such as proteins. As we know, more the number of atoms in an analyte, more the number of bands that will be visible under Raman spectroscopy (given most of them are Raman active). This may lead to a very complex spectra from which it might not be very straightforward to extract some information. In resonance Raman we can select and excite a particular transition and study the information contained in that particular molecule. Thus we can reduce the complexity of spectra to a large extent.

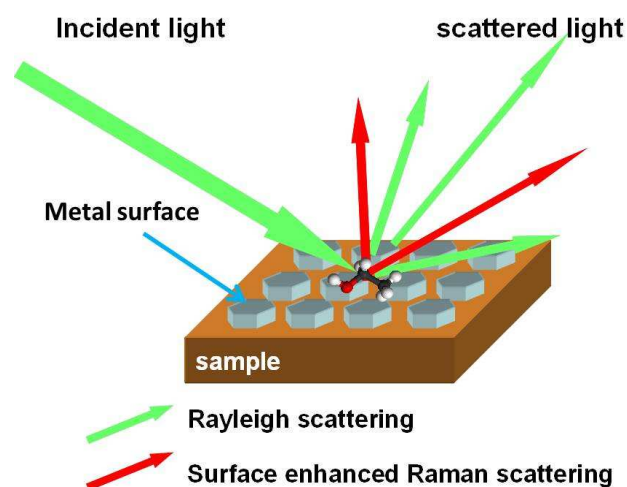


Figure 2.3: Representation of surface enhanced Raman scattering.

2.0.4 Surface enhanced Raman scattering.

Although Raman is an extremely sensitive technique, it suffers from a major drawback of very low efficiency. Biomolecules, in particular, have very low Raman cross-section and the output signal may be accompanied by huge background or fluorescence signal, thus obscuring the visibility of Raman bands.

Resonance Raman can be helpful, but it has certain disadvantages and might be suited for certain experiment types. I have used Surface enhanced Raman scattering (SERS) as one of the method to enhance Raman signal. SERS is a form of Raman spectroscopy which involves the study of samples adsorbed to or interacting in some manner with metal surfaces, typically nanoscale featured gold or silver surfaces, or, gold or silver colloids (fig. 2.3).

Although now a widely accepted and utilized technique, the first SERS experiment was accidentally performed as recently as 1974. The initial discovery by Fleischmann [45] reported very intense spectra for pyridine on a roughened silver electrode. The intensity of the spectra was initially attributed to an increase in molecular packing on the surface, which (due to successive oxidation and reduction cycles) had an increased surface area. Further research showed that this increased packing density alone could not account for the intensity increase and in 1977 two independently developed theories were published [46, 47]. They showed that the scattering intensity from the adsorbed molecules is $10^5 - 10^6$ times stronger than that of non-adsorbed molecules. Even higher enhancement ($10^{14} - 10^{15}$) can be achieved which allows SERS to be sensitive enough to detect single molecules [48]. The enhancement factor depends on the metal surface and type of the molecule.

SERS is sensitive to the surface on which the experiment is taking place. The structural properties of the metal nanoparticles strongly affect the enhancement efficiency because these influence the ratio of absorption and scattering events. "Surface roughness" is essential for SERS. In this context 'roughness' means that a surface must have regions with a certain curvature.

The details of the several proposed mechanisms of enhancement remain a matter of debate. It is considered that the "Electromagnetic Model" (EM) operates in majority of the cases, although some contribution from "Charge Transfer Model" (CT) is often also involved. As Raman scattering is governed by the relationship $P = \alpha E$, then SERS must involve an increase in either or both of the terms E (amplitude of the electric field), and α (molecular polarizability). The EM theory essentially addresses the enhancement of E , and the CT model is concerned with the enhancement of α . One common feature between these two theories is that both require surface roughness for spectral enhancement.

Electromagnetic enhancement

The EM model deals with E , the amplitude of the electric field of light (a molecule independent factor), and proposes that enhancement is due to the structure of the surface, and interaction of adsorbed molecules with surface plasmon.

Localized surface plasmons are generated when an electromagnetic wave interacts with metal surface. Maximum field enhancement is achieved when the incident beam is in resonance with plasmon frequency ω_p . In order for scattering to occur, the plasmon oscillations must be perpendicular to the surface; if they are in-plane with the surface, no scattering will occur. It is because of this requirement that roughened surfaces or arrangements of nanoparticles are typically employed in SERS experiments as these surfaces provide an area on which these localized collective oscillations can occur [49].

Suppose light from a laser is incident on a small metallic sphere then the field at the surface is described by:

$$E_r = E_0 \cos \theta + g \left(\frac{a^3}{r^3} \right) E_0 \cos \theta, \quad (2.18)$$

where E_r is the total electric field at a distance r from the sphere surface, a is the radius of the sphere, θ is the angle relative to the direction of the electric field, and g is a constant related to the dielectric constants such that,

$$g = \left(\frac{\epsilon_1(\nu_L) - \epsilon_0}{\epsilon_1(\nu_L) + 2\epsilon_0} \right), \quad (2.19)$$

where ϵ_0 and ϵ_1 are the dielectric constants of the medium surrounding the sphere and of the metal sphere respectively. ν_L is the frequency of the incident radiation. In general, ϵ_0 is close to 1, hence g will be maximum if ϵ_1 will be around -2. At this frequency, the plasmon resonance frequency, the excitation of the surface plasmon greatly increases the local field experienced by the molecule absorbed on the metal surface. Although the light beam is linearly polarized, we can not control the orientation of metal colloids with respect to the direction of polarized light. Hence it is not possible to tell with surety the orientation of electric field.

According to eq. (2.18), if surface plasmon is not generated, then there is no enhancement in electric field and the system behaves like normal Raman scattering.

Chemical enhancement

The chemical enhancement (CE) mechanism provides an order or two of enhancement to the Raman signal intensity [50]. It is less understood than the EME enhancement, but brings some interesting considerations to a thorough discussion of SERS. The CE enhancement is associated with a charge transfer process between the adsorbed molecule and the metal surface. The molecule adsorbed onto the surface necessarily interacts with the surface. This interaction is responsible for CE, which has been described in several ways. The metal adsorbate proximity may allow pathways of electronic coupling from which novel charge-transfer intermediates emerge that have higher Raman scattering cross-sections than does the analyte when not adsorbed onto the surface. This is very much like Resonance Raman effect. Alternatively it can be explained as the alterations in analyte's chemistry caused by the molecular orbitals of the adsorbate broaden into the conducting electrons of the metal. It is interesting to note that the CE effect may be an alteration in the scattering cross-section; the chemical nature of the analyte changing due to its interaction with the metal, whereas the EME effect was a change in the intensity of those analyte molecules that did scatter, not a change in scattering cross-section.

3

Microrheology

Rheology relates to the viscoelastic properties of a material. Simple solids store energy and provide elastic response, whereas simple liquids dissipate energy through viscous flow. For more complex viscoelastic materials, rheological measurements reveal both the solid and fluid-like behavior and generally depend on the time scale at which the sample is probed [51]. The rheological behavior of most soft materials can exhibit many regimes depending on the scale, geometry, amplitude, and rate of the imposed deformation. To determine the effect of local variations on these materials, the technique of rheology is exploited. Rheology describes how materials store and dissipate mechanical energy as a function of length scale. Complex fluids like actin solution and complex materials such as polymers and biomolecules are viscoelastic systems so they can act both like lossy and elastic. Rheology can describe the combined viscous and elastic properties of these materials. Whereas in macroscopic rheology stress-strain relationship are measured through mechanical deformation of bulk materials, in microrheology the embedded probe motion is tracked and its relationship to the local environment inferred. Only small amounts of sample are required for this technique unlike conventional rheology which needs samples in bulk. Before describing in details regarding the theory of microrheology, it is pertinent that we review the basic concepts of viscosity and elasticity. These concepts are discussed in details in [52].

Initial use of microrheology was in the analysis of uniform complex fluids and it was a challenge to investigate materials containing structural heterogeneity. These materials are structured on a range of length scales greater than that of their molecular arrangement. Investigations for cellular structures and DNA, which are far from an homogeneous mixture, are helpful to assess and interpret the dynamic local mechanical properties. Cells continually rearrange their internal structure, they change shape and divide, and thereby modify their mechanical properties. Their invariable modification requires the transport of molecules and signaling through intracellular regions with variable material properties, such as changes in viscosity or elasticity. It is important

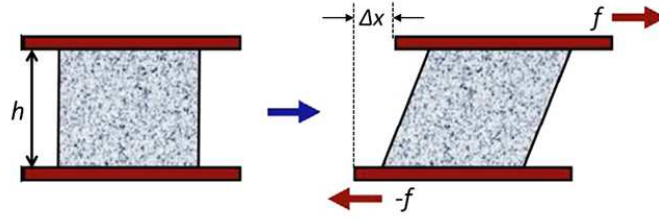


Figure 3.1: A typical schematic for a shear measurement is depicted, in which two parallel bars attached to the top and bottom of the sample are moved relative to each other (right). Measurements of the extent of deformation and the force required to make the movements determine the viscoelastic properties of the sample.

to understand the material properties of a cell and DNA to unfold its dynamic and functional behavior. It has been argued that biomolecules have both elastic and viscous characteristics. Cells and DNA are highly nonlinear in nature and their elastic behavior depends on the properties of the environment in which they are embedded [53]. Therefore, microrheology is an useful technique for understanding the viscoelastic properties of biomolecules.

3.0.5 Macrorheology - Basic concepts

Consider a material sandwiched between two parallel surfaces, as shown in fig. 3.1. In this simple shear demonstration, the top surface is displaced with a force f in the x -direction, and the force is transmitted to the bottom surface via the sandwiched material. If the material is adhered strongly to the surfaces, then there will not be any slippage at either surfaces. If the material is perfectly rigid, the bottom plate must experience a force $-f$ to prevent net translation in the $+x$ direction. The shear stress (σ) resulting from the force exerted in the $+x$ direction and transmitted to a planar cross-sectional area A normal to the y -direction is defined as:

$$\sigma \equiv \frac{f}{A}. \quad (3.1)$$

Shear strain (ϵ) can be defined as the ratio of displacement of top plate (Δx) and the thickness of the sample (h):

$$\epsilon \equiv \frac{\Delta x}{h}. \quad (3.2)$$

For a perfectly elastic material, the stress is linearly proportional to the strain. The constant of proportionality, known as the shear modulus G , is defined by:

$$G \equiv \frac{\sigma}{\epsilon}. \quad (3.3)$$

Both shear stress and shear modulus have are measured in Pascals. Given that the deformation is uniform, the material will experience same local stress and strain on the application of a force. This property of elastic material, where the modulus is constant over a range of strains is known as Hooke's law of elasticity.

Depending on the material and type of deformations, shear can be volume conserving or non-volume conserving. Some general representation of various deformations are depicted in fig. 3.2.

For a purely liquid material, the shear stress is independent of strain. In this case, shear stress depends linearly on the shear rate $\dot{\epsilon} \equiv \frac{d\epsilon}{dt}$. The constant of proportionality is known as viscosity (η) and can be defined as:

$$\eta \equiv \frac{\sigma}{\dot{\epsilon}}. \quad (3.4)$$

Fluids that are represented by eq. (3.4) are known as Newtonian fluids. For such fluids, the resistance to deformation (shear stress), in contrast to solids, is independent of amplitude of deformation, but depends only on the rate of deformation.

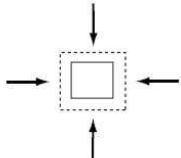
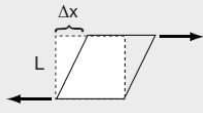
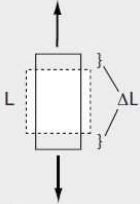
Modulus	Strain	Deformation
Bulk (K)	$\frac{\Delta V}{V}$	
Shear (G)	$\frac{\Delta x}{L}$	
Extensional, Young's (E)	$\frac{\Delta L}{L}$	

Figure 3.2: Basic modulus, strain and deformation for homogeneous isotropic materials. Figures with solid lines are the material after deformation while dashed figure corresponds to material prior to deformation. Shaded region corresponds to volume-conserving deformations.

3.0.6 Viscoelasticity

In practice, most of the materials behave neither as Hookean solid nor as Newtonian fluid, having time-dependent mechanical responses between Newtonian fluids and Hookean solids. These are known as *viscoelastic* materials.

Viscoelasticity can be understood using a time-dependent shear modulus $G(t) \equiv \sigma(t)/\epsilon$. Suppose a constant stress, σ_0 , is applied at time $t = t_0$ as shown in fig. 3.1. Now for a Hookean solid with shear modulus G , the stress will

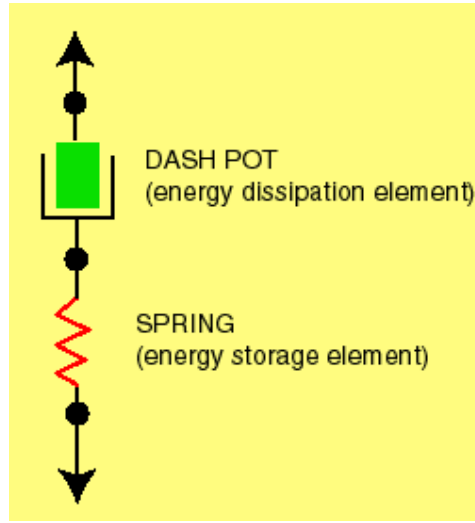


Figure 3.3: The spring-dashpot Maxwell model for viscoelastic materials.

remain ϵG till the time stress is applied and then it will almost instantly return to zero once the stress is removed. In contrast, for a Newtonian fluid a sharp spike will be exhibited on the application of stress and then decay rapidly to zero. If, on the other hand, the material is viscoelastic in nature then the stress will decay exponentially to zero with a characteristic relaxation time τ .

Most of the linear viscoelastic materials can be modeled as some combinations of Hookean springs and Newtonian dampers (dashpot). The elastic elements can be modeled as Hookean spring as:

$$\sigma = G\epsilon, \quad (3.5)$$

where σ is the applied stress, G is the shear modulus of the material, and ϵ is the strain that results from the given stress. Similarly, we can model the stress for Newtonian dampers as:

$$\sigma = \eta \frac{d\epsilon}{dt}, \quad (3.6)$$

where η is viscosity and $d\epsilon/dt$ is the strain rate.

Two of the most commonly studied models for viscoelastic behavior are the Maxwell and Voigt models. The Generalized Maxwell model, also known as the Maxwell–Wiechert model, is most commonly used as linear model for viscoelasticity. In this case, a viscoelastic material can be modeled by a dashpot and a spring connected in series, as shown in the fig. 3.3. The spring represents the elastic or storage component of the material, while the dashpot represents the conformational or lossy component. In this configuration, stress on each element is the same and equal to the imposed stress, while total strain is given as the sum of the strain in each element:

$$\begin{aligned} \sigma &= \sigma_s = \sigma_d, \\ \epsilon &= \epsilon_s + \epsilon_d, \end{aligned} \quad (3.7)$$

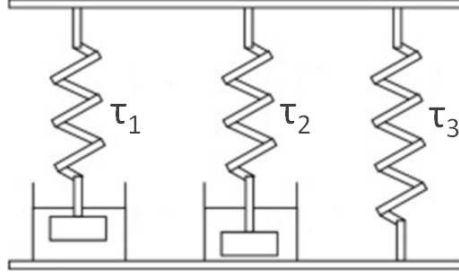


Figure 3.4: The spring-dashpot Maxwell model for complex viscoelastic materials.

where the subscripts s and d refers respectively to spring and dashpot. Serial combination of spring and dashpot takes into account that the relaxation does not occur at a single time, but at a distribution of times. Most of the complex network has molecular segments of different lengths where shorter segments contribute less than longer ones and hence a time dependent relaxation occurs. Thus, these network possess a critical time scale below which the response is dominantly elastic and above which the response is dominantly viscous.

Time dependent strain for the viscous part, when a constant strain ϵ_0 is applied at $t = t_0$, is given by:

$$\tau \frac{d\epsilon_d(t)}{dt} = \epsilon_0 - \epsilon_d(t), \quad (3.8)$$

where τ is the relaxation time given by $\tau \equiv \eta/G$. From above equation we can obtain:

$$\begin{aligned} \frac{d\epsilon_d(t)}{\epsilon_0 - \epsilon_d(t)} &= \frac{dt}{\tau}, \\ \ln(\epsilon_0 - \epsilon_d(t)) &= \frac{-t}{\tau} + C. \end{aligned} \quad (3.9)$$

With the initial condition as $\epsilon_d(0) = 0$, we get $C = \ln\epsilon_0$. Strain in elastic part can be written as:

$$\epsilon_s(t) = \epsilon_0 - \epsilon_d(t) = \epsilon_0 e^{(-t/\tau)}. \quad (3.10)$$

As the stress across spring and dashpot is identical, hence we can write:

$$\sigma(t) = G\epsilon_s(t) = G\epsilon_0 e^{(-t/\tau)}. \quad (3.11)$$

In the Maxwell model for linear deformations, the relaxation modulus for stress can be given by $G(t) = \sigma(t)/\epsilon_0 = Ge^{(-t/\tau)}$. According to this equation, stress relaxation is independent of strain and depends only on single relaxation time τ in the linear regime.

This Maxwell model for two elements is overly simplified and in most practical cases can not describe the system completely. Nevertheless, more complex systems can be modeled as multiple basic Maxwell elements of series springs and dashpots as shown in fig. 3.4. Each of these series of springs and dashpots forms an independent mode with their own relaxation time in the linear regime. Network behavior can be obtained by linear superposition of these modes to yield

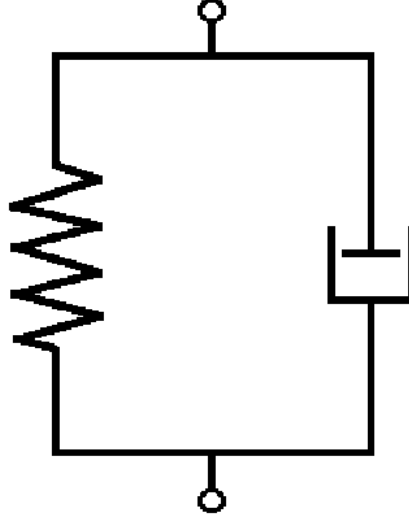


Figure 3.5: The spring-dashpot Kelvin model for viscoelastic materials.

a multi-timescale decay profile of stress relaxation. For example, in a polymer network there are multiple length scales in the underlying polymer distribution. All these length distribution will have its own relaxation time and hence they vibrate with a characteristic frequency.

Voigt Model (also known as Kelvin-Voigt model) is another commonly used model to represent complex networks. They are useful in studying crosslinked polymer networks. Voigt model consists of an elastic spring and a dashpot connected in parallel as shown in fig. 3.5. Contrary to Maxwell model, in Voigt systems strain is uniformly distributed ($\epsilon_0 = \epsilon_s = \epsilon_d$) while total stress is the sum of stress ($\sigma_0 = \sigma_s + \sigma_d$) present in each element. In such a network, as long as strain or stress is applied, the stress will never relax in that duration. When a step stress is imposed, the strain increases across both elements gradually until it reaches to a saturating value.

The total stress across the system may be written as:

$$\sigma(t) = G\epsilon(t) + \eta \frac{d\epsilon}{dt}. \quad (3.12)$$

If a constant step stress, $\sigma(t) = \sigma_0$, is applied then eq.(3.12) can be written as:

$$\tau \frac{d\epsilon}{dt} + \epsilon(t) = \frac{\sigma_0}{G}, \quad (3.13)$$

where $\tau = \eta/G$. Solving eq.(3.13) with initial condition $\epsilon(0) = 0$, the time-dependent strain for Voigt model can be found as:

$$\epsilon(t) = \frac{\sigma_0}{G} \left(1 - e^{-t/\tau}\right). \quad (3.14)$$

Although, Maxwell model is more often used for solids and the Voigt model is predominantly used for liquids, the choice is not obvious in viscoelastic materials such as cells and gels.

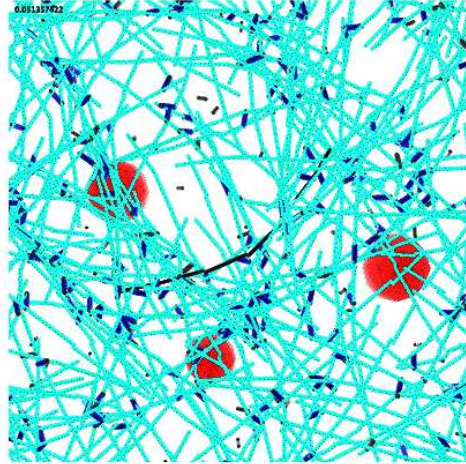


Figure 3.6: In PMR, embedded micro-sized mechanical probes locally deform the medium and extract information from their thermal motion.

3.1 Microrheology

Microrheology is generally classified in two groups - passive microrheology (PMR) and active microrheology (AMR) [12, 51, 54]. PMR tracks the Brownian (thermal) motion of the probe (fig. 3.6) and with its help studies the response function of the medium in which it is embedded. The thermal fluctuations of the probe (tracers) are measured optically either by microscopy, by diffusing-wave spectroscopy or by optical trapping technique. Observing the motion of the probe particle can tell us the nature of medium which is being probed. If the motion of probe particle is freely diffusive then one can say that the medium is purely viscous in nature. On the other hand if the probe has sub-diffusive trajectory then we can deduce that the medium has viscoelastic properties. The drawback of PMR, however, is that this technique is still limited at high frequencies and for materials with internal fluctuations (such as cells), direct measurement of complex shear modulus can not be computed.

AMR tracks the motion of probe that is under the influence of some external force. This method directly measures the response of tracer particles to an oscillating external force that can be applied using optical or magnetic tweezers. It has been shown that through AMR one can achieve a bandwidth of 0.1 Hz to 100 KHz [12].

Let us consider the main mathematical formulations that would be needed for the interpretation of experimental results.

3.1.1 Fluctuation-dissipation theorem

Probes go under numerous collisions during thermal motion. Although these collisions occur randomly, a number of the collisions produce a systematic force on the probe proportional to the motion of the particle. Thus random impacts of surrounding molecules leads to two kinds of effect: firstly, they act as a

random driving force on the particle to maintain its incessant irregular motion (Brownian motion), and, secondly, they give rise to the frictional force for a forced motion. Hence frictional force and the random force should be related to each other as they have the same origin. This internal relationship between the systematic and the random parts of microscopic forces is termed as the fluctuation-dissipation theorem [55].

This theorem links the response of a given system to an external perturbation and the internal fluctuation of the system in the absence of the perturbation. Such a response is characterized by a response function which has a complex behavior in general. The internal fluctuation is characterized by a correlation function of the probe particle fluctuating in thermal equilibrium, or by their fluctuation spectra. The fluctuation-dissipation theorem thus provides following information: (i) it can predict the characteristics of the fluctuation or the noise intrinsic to the system from the known characteristics response function, or (ii) it can be used as the basic formula to derive the response function of the medium from the analysis of thermal fluctuations of the system.

Einstein's diffusion relation

In 1905, Einstein gave a diffusion equation for a Brownian particle in a solution [56]. Diffusion constant (D) of a particle is given by:

$$D = \frac{k_B T}{\beta}, \quad (3.15)$$

where, $\beta = 6\pi\eta R$ is the friction constant. Here η is viscosity of the medium and R is the radius of probe. Eq. (3.15) is known as the Stokes-Einstein relation and forms the theoretical basis of all passive microrheology measurements. It states that the diffusivity of a particle due to thermal excitation can be used to generate information regarding the viscosity of the fluid, thus relating an embedded probe particle's dynamics with the medium's rheology. It is also important to note that Eq. (3.15) contains a constant (i.e. frequency/time-independent) viscosity. However, in the preceding sections we have seen that most soft materials are viscoelastic, and, hence, frequency-dependent moduli are necessary to describe their rheological response. Therefore it is important to establish a generalized Stokes-Einstein relation for materials with viscous properties.

In the presence of an external potential $U(x)$, the particle flows with a drift velocity of:

$$v = -\frac{\partial U/\partial x}{\beta}, \quad (3.16)$$

which is opposite to diffusion current. In equilibrium, the particles concentrate around the areas with lowest U , but will still be spread out to some extent because of random diffusion. Hence, the net drift current is given by:

$$J(x) = -D \frac{\partial f(x)}{\partial x} + v f(x), \quad (3.17)$$

where $f(x)$ is the concentration of particle at position x . In equilibrium, we can infer that eq. (3.17) is equal to zero and $f(x) \propto \exp(-U/k_B T)$.

If a particle covers a distance x , in a given time t , then the probability distribution of x is given by the solution of a diffusion equation. Therefore we

may assume that

$$D = \lim_{t \rightarrow \infty} \frac{1}{2t} \langle (x(t) - x(0))^2 \rangle, \quad (3.18)$$

where the average is taken over an ensemble in thermal equilibrium. Also, we can write

$$x(t) - x(0) = \int_0^t v(t') dt'. \quad (3.19)$$

Eq.(3.18) can thus be written as:

$$\begin{aligned} D &= \lim_{t \rightarrow \infty} \frac{1}{2t} \int_0^t dt_1 \int_0^t dt_2 \langle v(t_1)v(t_2) \rangle \\ &= \lim_{t \rightarrow \infty} \frac{1}{t} \int_0^t dt_1 \int_0^{t-t_1} dt' \langle v(t_1)v(t_1+t') \rangle \\ &= \int_0^\infty \langle v(t_0)v(t_0+t) \rangle dt, \end{aligned} \quad (3.20)$$

where it has been assumed that

$$\lim_{t \rightarrow \infty} \langle v(t_0)v(t_0+t) \rangle = 0. \quad (3.21)$$

Therefore, eq. (3.15) can be written in term of mobility (μ), which is inverse of friction constant, as

$$\mu = \frac{1}{\beta} = \frac{D}{kT} = \frac{1}{kT} \int_0^\infty \langle v(t_0)v(t_0+t) \rangle dt. \quad (3.22)$$

From Eq. (3.22) we can say that the mobility of a particle is related to the Brownian motion fluctuations. This relationship is a common display of *fluctuation-dissipation theorem*.

Fluctuation-dissipation theorem for Brownian motion.

Momentum (p) of a particle under Brownian motion can be given by stochastic differential equation as:

$$\frac{dp}{dt} = -\Gamma p + f(t), \quad (3.23)$$

where $\Gamma = m\gamma$ is friction constant (γ is friction coefficient) and $f(t)$ is stochastic force. Convoluting Eq. (3.23) with Green's function gives us:

$$p(t) = \int_0^\infty dt' e^{-\Gamma t'} f(t-t'). \quad (3.24)$$

Let us assume that the stochastic force obeys the following two relations for average and covariance:

$$\langle f(t) \rangle = 0, \quad (3.25)$$

$$\langle f(t_1).f(t_2) \rangle = C(t_1 - t_2). \quad (3.26)$$

Equations (3.25) and (3.26) are valid for homogeneous stochastic processes. As left hand side of eq. (3.26) is symmetric in t_1 and t_2 , so C should be an even

function. Expectation value of momentum can be defined as:

$$\begin{aligned} \langle p^2 \rangle &= \left\langle \int_0^\infty dt_1 e^{-\Gamma t_1} f(t-t_1) \int_0^\infty dt_2 e^{-\Gamma t_2} f(t-t_2) \right\rangle \\ &= \int_0^\infty dt_1 \int_0^\infty dt_2 e^{-\Gamma(t_1+t_2)} C(t_1-t_2), \end{aligned} \quad (3.27)$$

Let us transform our time variable to new coordinate system, which can be defined as:

$$\begin{aligned} t_- &= t_1 - t_2, \\ t_+ &= \frac{1}{2}(t_1 + t_2). \end{aligned} \quad (3.28)$$

From eq. (3.27) and (3.28) we can write:

$$\langle p^2 \rangle = \frac{1}{\Gamma} \int_0^\infty dt_- C(t_-) e^{-\Gamma t_-}. \quad (3.29)$$

If the Laplace transform of C is written as C^* , then we can write eq. (3.29) as:

$$\langle p^2 \rangle = \frac{C^*(\Gamma)}{\Gamma}. \quad (3.30)$$

Equipartition theorem for d -dimensional space will give:

$$\frac{\langle p^2 \rangle}{2m} = \frac{d}{2} k_B T, \quad (3.31)$$

where m is the mass of the particle. Equations (3.30) and (3.31) will lead to:

$$\Gamma = \frac{C^*(\Gamma)}{dmk_B T}. \quad (3.32)$$

This equation is known as ‘‘fluctuation-dissipation theorem’’ which relates the correlation function of the fluctuating force to the frictional coefficient (or dissipation).

3.1.2 Generalized Stokes-Einstein relation

In generalized Stokes-Einstein relation (GSRE) we assume that the mobility adopts the same functional form at all frequencies:

$$\mu^*(\omega) = \frac{1}{6\pi\eta^*(\omega)R}. \quad (3.33)$$

This assumption is made on the basis of linearity found in eq. (3.15). With this assumption and with the help of Langevin equation, relationship between mean square displacement (MSD) and frequency dependent mobility can be found [57]:

$$m\dot{V} = f_R(t) - \int_0^t \zeta(t-t')V(t')dt', \quad (3.34)$$

where $f_R(t)$ is a random force acting on the spherical probe particle in an isotropic linear viscoelastic material, m is the mass and V is the velocity of the

probe respectively. $\zeta(t-t')$ is the time dependent hydrodynamic resistance given by $F_H(t) = \int_0^t \zeta(t-t')V(t')dt'$ whose Laplace transform is inverse of mobility $\tilde{\zeta}(s) = \tilde{\mu}(s)^{-1}$. Taking the Laplace transform of eq. (3.34), we can solve for $\tilde{V}(s)$ as:

$$\tilde{V}(s) = \frac{mV(0) + \tilde{f}_R(s)}{ms + \tilde{\zeta}(s)}, \quad (3.35)$$

where $\tilde{V}(s)$ is the Laplace transform of $V(t)$ and s is the Laplace frequency. Multiplying eq. (3.35) by $V(t=0)$ and taking an ensemble average gives:

$$\langle V(0)\tilde{V}(s) \rangle = \frac{m\langle V(0)^2 \rangle + \langle V(0)\tilde{f}_R(s) \rangle}{ms + \tilde{\zeta}(s)}. \quad (3.36)$$

In stochastic processes, such as this, it is not inappropriate to assume $\langle f_R V = 0 \rangle$ and equipartition theorem gives us $\frac{1}{2}mV(0)^2 = \frac{1}{2}k_B T$. The autocorrelation function of eq. (3.36) for d -dimensional space can thus be written as:

$$\langle V(0)\tilde{V}(s) \rangle = \frac{dk_B T}{ms + \tilde{\zeta}(s)}. \quad (3.37)$$

In most of the medium, the inertial term ($\tilde{\zeta}(s)$) dominates the inertial term ms . Hence the eq. (3.37) can be written as:

$$\langle V(0)\tilde{V}(s) \rangle \approx dk_B T \tilde{\zeta}^{-1}(s) = dk_B T \tilde{\mu}(s). \quad (3.38)$$

The Laplace transformation of velocity autocorrelation can be related to MSD via the equation:

$$\langle V(0)\tilde{V}(s) \rangle = \frac{s^2}{2} \mathcal{L} \langle \Delta r^2(t) \rangle = \frac{s^2}{2} \langle \Delta \tilde{r}^2(s) \rangle, \quad (3.39)$$

where \mathcal{L} denotes the Laplace transform. Comparing eq. (3.38) and eq. (3.39) gives:

$$\langle \Delta \tilde{r}^2(s) \rangle \approx \frac{2dk_B T}{s^2 \tilde{\zeta}(s)} = \frac{2dk_B T}{s^2} \tilde{\mu}(s), \quad (3.40)$$

$$\tilde{\mu}(s) = \frac{s^2 \langle \Delta \tilde{r}^2(s) \rangle}{2dk_B T}.$$

Here we can introduce frequency dependent shear modulus $\tilde{G}(s)$, such that

$$\tilde{G}(s) = \frac{dk_B T}{3\pi R s \langle \Delta \tilde{r}^2(s) \rangle}, \quad (3.41)$$

where R is probe radius. Then the probe mobility can be written in terms of $\tilde{G}(s)$ as:

$$\tilde{\mu}(s) = \frac{s}{6\pi R \tilde{G}(s)}. \quad (3.42)$$

Eq. (3.41) is the backbone for all rheological measurements which involve measurement of thermal motion of an embedded spherical probe and is known as *generalized Stokes–Einstein relation*. It states that the Laplace transform of the shear modulus of the medium is related to the Laplace transform of the probe's MSD. The continuous Fourier transform is equivalent to evaluating the bilateral Laplace transform with imaginary argument $s = i\omega$. Hence eq. (3.41) can be represented in terms of Fourier transform via analytic substitution $s = i\omega$.

3.1.3 Passive microrheology

In *passive microrheology (PMR)*, one studies the motion of probe due to thermal fluctuations. The most straightforward and direct method for measuring molecular motion is to track its trajectory directly in an optical microscope. This technique has an advantage of measuring ~ 100 particles simultaneously, hence giving a good statistics in very short time. But this technique suffers from a low bandwidth measurement. This limitation of small bandwidth can be overcome by combining optical tweezers with high speed position detection system. This technique can provide higher temporal and spatial resolution.

PMR using optical tweezers can be performed using one-particle (1PMR) and two-particles (2PMR). 1PMR is the most simple approach to measure rheological properties of a medium. Such measurements probe the dynamics on length scales comparable to that of the optically trapped probe. Hence, the bulk properties of material may not be truly studied using this technique. Two-particle microrheology (2PMR) studies the cross-correlated thermal motion of pairs of tracer particles separated by distance r , which can be much larger than the probe particle size and thus probe the mechanics of the medium on a length scale comparable to the interparticle separation. This technique is independent of probe size and the coupling between probe and the medium [9, 11, 54].

The motion of an optically trapped probe in a purely viscous medium is described by the Langevin equation,

$$k_1 u(t) + \beta \frac{du(t)}{dt} = f_R(t), \quad (3.43)$$

where k_1 is the stiffness of the trap, β is the viscous drag coefficient and $f_R(t)$ is the random thermal force. In system with low Reynold's number, viscous drag dominate and hence we have neglected the inertial term in above equation.

Thermal (Brownian) motions of probes are exactly described by linear response theory [58]. We can relate the Fourier transform of the displacement $u_\alpha^j(\omega)$ of particle j (1 or 2) in direction α (x or y) to the Fourier transform of the applied force $F_\beta^k(\omega)$ applied to particle k in direction β via the response function $\chi_{\alpha\beta}^{j,k}(\omega)$ as: $u_\alpha^j(\omega) = \chi_{\alpha\beta}^{j,k}(\omega) F_\beta^k(\omega)$. Here, $\omega = 2\pi f$ is the radial frequency. We have employed the Einstein summation convention in which both coordinate directions (Greek indices) β and particle numbers (Latin indices) k are summed over. The single-particle response functions $\chi_{\alpha\beta}^{1,1}(\omega)$ and $\chi_{\alpha\beta}^{2,2}(\omega)$ refer to the displacement responses of particles 1 and 2 to forces applied to the same particle. The $\chi_{\alpha\beta}^{j,k}(\omega)$ for $j \neq k$ refer to the inter-particle response functions, e.g., describing how particle 1 responds to forces on particle 2, while for $j = k$ refers to single particle response function. The complex response function can be separated in real part (in-phase) and imaginary part (out of phase) component in the following way: $\chi_{\alpha\beta}^{j,k}(\omega) = \chi_{\alpha\beta}^{\prime j,k}(\omega) + \chi_{\alpha\beta}^{\prime\prime j,k}(\omega)$.

The correlation function of both probes for the x and y direction can be given by:

$$S_{\alpha\beta}^{(j,k)}(\omega) \equiv \int_{-\infty}^{\infty} \langle u_\alpha^j(t) u_\beta^k(0) \rangle e^{i\omega t} dt, \quad (3.44)$$

which is the Fourier transform of time series data of trapped probe. For $j \neq k$, we get cross-correlation function, while for $j = k$ we get autocorrelation spectra of the trapped probe. Now from fluctuation-dissipation theorem, we can relate

the imaginary part of response function to $S(\omega)$ by,

$$S_{\alpha\beta}^{(j,k)}(\omega) = \frac{2k_B T}{\omega} \chi_{\alpha\beta}^{\prime\prime(j,k)}(\omega). \quad (3.45)$$

For getting the real part we can make use of *Kramers–Kronig relation*, which are bidirectional mathematical relations connecting the real and imaginary parts of any analytical complex function, such that

$$\chi_{\alpha\beta}^{\prime(j,k)}(\omega) = \frac{2}{\pi} P \int_0^\infty \frac{\omega' \chi_{\alpha\beta}^{\prime\prime(j,k)}(\omega')}{\omega'^2 - \omega^2} d\omega', \quad (3.46)$$

where P denotes the principal value integral. Care must be taken while calculating $\chi'(\omega)$ in eq. (3.46) because the cosine and sine transforms of finite samples can lead to discontinuities or nonsensical data corresponding to the smallest and largest frequencies studied. $\chi''(\omega)$ can be faithfully calculated only when $\chi'(\omega)$ is known over a large enough range of frequency [12, 59].

Optical trapping generates an external potential on the probes that is independent of inherent mechanical properties of the medium and depends solely on optical trapping power. This will influence the thermal motions and consequently must be corrected for getting medium response function. If this is not taken into account, the trapping potential will introduce an error in the magnitude of the storage modulus derived from the particle fluctuations, which can be dominant at low frequencies. In the absence of optical traps, the complex shear modulus G of isotropic, inhomogeneous and incompressible medium for an isolated particle can be related to the complex response function $\chi(\omega)$ through a generalized Stokes-Einstein relation [54, 57, 59],

$$\chi(\omega) \rightarrow \alpha(\omega) = \frac{1}{6\pi R G(\omega)}, \quad (3.47)$$

where, $\alpha(\omega)$ is the response function of the medium in absence of trap. It is the response of the medium that we are interested in, that is why it is important that we evaluate $\alpha(\omega)$ from $\chi(\omega)$ for a trapped probe. The measured response function $\chi(\omega)$ equals the *actual* response of the medium only in the absence of the trapping potentials.

Similarly, in the absence of optical trap, the inter-particle response function between two probe separated by a distance r can be given generalization of the Oseen tensors [54]:

$$\chi_{||}(\omega) \rightarrow \alpha_{||}(\omega) = \frac{1}{4\pi r G(\omega)}, \quad (3.48a)$$

$$\chi_{\perp}(\omega) \rightarrow \alpha_{\perp}(\omega) = \frac{1}{8\pi r G(\omega)}, \quad (3.48b)$$

where $\chi_{||} \equiv \chi_{x,x}$ and $\chi_{\perp} \equiv \chi_{y,y}$. Above equations have been deduced by assuming that the contribution of inertia is negligible. Both these equations can be used to find the value of $G(\omega)$, but in experiments perpendicular channels are noisier than parallel channels.

In the presence of optical traps, the probes feel an additional force generated by optical potential, modifying the motion of trapped beads, $u_{\alpha}^j(\omega)$. For small motion, we can model the optical traps as Hookean spring of characteristic trap stiffness. Hence, force applied on the j probe due to trap in α^{th} direction can

be given as $-k^j u_\alpha^j(\omega)$, where k^j is the stiffness of the trap holding probe j in the beam focus. Thus, if an external force $F_\alpha^j(\omega)$ is applied to the probe j , then the total force acting on the probe in the direction α will be $F_\alpha^j(\omega) - k^j u_\alpha^j(\omega)$. Displacement $u_\alpha^j(\omega)$, in terms of medium response function can be written as [54]:

$$u_x^1(\omega) = \alpha^1(\omega) \times [F_x^1(\omega) - k^1 u_x^1(\omega)] + \alpha_{||}(\omega) \times [F_x^2(\omega) - k^2 u_x^2(\omega)], \quad (3.49a)$$

$$u_x^2(\omega) = \alpha_{||}(\omega) \times [F_x^1(\omega) - k^1 u_x^1(\omega)] + \alpha^2(\omega) \times [F_x^2(\omega) - k^2 u_x^2(\omega)], \quad (3.49b)$$

where k^1 and k^2 are the trap stiffness of the two traps. Similarly we can write a pair of equation for movement in y -direction by simply substituting x by y in above equations.

The measured response function χ can be written as a function of α by solving the above equation for $u_\alpha^j(\omega)$ [54]:

$$\begin{aligned} \chi_{xx}^{(1,1)} &= \chi_{||}^1 \\ &= \frac{\alpha^1 + k^2 \alpha^1 \alpha^2 - k^2 (\alpha_{||})^2}{1 + k^1 \alpha^1 + k^2 \alpha^2 + k^1 k^2 \alpha^1 \alpha^2 - k^1 k^2 (\alpha_{||})^2}, \end{aligned} \quad (3.50a)$$

$$\begin{aligned} \chi_{yy}^{(1,1)} &= \chi_{\perp}^1 \\ &= \frac{\alpha^1 + k^2 \alpha^1 \alpha^2 - k^2 (\alpha_{\perp})^2}{1 + k^1 \alpha^1 + k^2 \alpha^2 + k^1 k^2 \alpha^1 \alpha^2 - k^1 k^2 (\alpha_{\perp})^2}. \end{aligned} \quad (3.50b)$$

From above equations we can see that the presence of two traps breaks the rotational symmetry of the single particle response since they differ from interparticle response. The response function for other particle can be obtained just by replacing the indices 1 by 2. As long as the particles used have same diameter and trapping potential is comparable, we should get same response function for both probes.

The interparticle response function can be given by [54]:

$$\begin{aligned} \chi_{xx}^{(1,2)} &= \chi_{||} \\ &= \frac{\alpha_{||}}{1 + k^1 \alpha^1 + k^2 \alpha^2 + k^1 k^2 \alpha^1 \alpha^2 - k^1 k^2 (\alpha_{||})^2}, \end{aligned} \quad (3.51a)$$

$$\begin{aligned} \chi_{yy}^{(1,2)} &= \chi_{\perp} \\ &= \frac{\alpha_{\perp}}{1 + k^1 \alpha^1 + k^2 \alpha^2 + k^1 k^2 \alpha^1 \alpha^2 - k^1 k^2 (\alpha_{\perp})^2}. \end{aligned} \quad (3.51b)$$

From the above equations of single particle response function and interparticle response function it can be observed that as stiffness of the traps approaches zero, the measured response function χ approaches the medium response function α . However, it is χ that we can measure and we are interested in knowing the value of α . Hence it is important that we rewrite eq. (3.50a), (3.50b), (3.51a) and (3.51b) so that α is a function of χ . This can be achieved by the inversion of above equations [54]:

$$\alpha^1 = \frac{\chi_{||}^1 + k^2 (\chi_{||})^2 - k^2 \chi_{||}^1 (\chi_{||})^2}{1 - k^1 \chi_{||}^1 - k^2 \chi_{||}^2 - k^1 k^2 (\chi_{||})^2 + k^1 k^2 \chi_{||}^1 \chi_{||}^2}, \quad (3.52a)$$

$$\alpha^2 = \frac{\chi_{||}^1 + k^1(\chi_{||})^2 - k^1\chi_{||}^1(\chi_{||})^2}{1 - k^1\chi_{||}^1 - k^2\chi_{||}^2 - k^1k^2(\chi_{||})^2 + k^1k^2\chi_{||}^1\chi_{||}^2}, \quad (3.52b)$$

$$\alpha_{||} = \frac{\chi_{||}}{1 - k^1\chi_{||}^1 - k^2\chi_{||}^2 - k^1k^2(\chi_{||})^2 + k^1k^2\chi_{||}^1\chi_{||}^2}. \quad (3.52c)$$

Corresponding equations for perpendicular motion for one particle and two particle response function can be obtained by substituting $\chi_{||}$ with χ_{\perp} in above equations. The value of α_1 and α_2 should be same for x and y motion for an isotropic and homogeneous medium.

We can extract the viscoelastic properties of the medium from the response function α , as measured with one and two particle microrheology, using eqs. (3.47) and (3.48a) after correcting for the trapping effect on the measured response function χ using eqs. (3.52a)-(3.52c). This pre-processing of the raw data can thus prevent systematic error that can be introduced by optical traps.

One-particle microrheology is a simple and powerful technique to study the rheological properties of extremely small sample volumes at frequencies inaccessible to bulk measurements. But this technique has certain limitations. First of all, 1PMR assumes that the local fluctuations of the particle reflects the property of the bulk. In many cases, this may not be true. For example, if the embedded bead modifies the local material configuration, then the one-particle response will be a reflection of the local microenvironment rather than bulk rheology. One particle response may not address the complete picture in complex soft matters such as cells and polymers which have time dependent response. One-particle microrheology is also dependent on the size of probe, such that the bulk properties are measured only if the probe size is larger than the length scale of heterogeneity in the sample. These length scales are often unknown prior to a microrheology experiment. When the probe diameter is comparable to or smaller than the length scale of structures in the medium, their motions does not only represent the viscoelastic response, but also of the effect of steric hindrances caused by the cavity walls [60].

These limitations of one particle microrheology can be overcome by using two particle microrheology developed by Crocker *et al.* [11]. This technique eliminates the response due to purely local structure by measuring a cross-correlated motion of a pair of probe particles in the sample. The correlated motion of the tracers is not affected by the size (or even shape) of the probe particles. The results are also not affected by coupling between probe and the medium. Furthermore, the length scale being probed is the distance between two beads, which can be much larger than the radius of probe, the length scale probed in 1PMR. This increase in length scale means that the technique can be used to measure overall rheological properties of the medium.

4

Materials and methods

4.1 Experimental set-up

Depending on the requirements of measurements, three different optical tweezers set-up are used. All these are dual-trap optical tweezers set-up. List of components used in all the set-ups have been summarized at the end of the thesis in Annex 3. Out of these three systems, two are used for Raman spectroscopy in combination with force measurements (Raman tweezers). These two set-ups are very similar in working except for the difference in the wavelengths of trapping beam and excitation beam and use of different spectrometers. The Raman excitation beam used for measurements were 785 nm and 532 nm for two systems. The 785 nm beam is used as there is less absorption in biomolecules for this wavelength and fluorescence background is also negligible, hence giving a better signal without damaging the sample. The reason for using 532 nm is to enhance the Raman signal through SERS effect in presence of silver nano-colloids.

4.1.1 Raman tweezers set-ups

Fig. 4.1 shows a schematic of Raman system, in combination with optical tweezers, used for our measurements. The system is divided into two parts - the first part being the optical tweezers setup and the second part is Raman setup. The tweezers part is made with the help of a 1064 nm diode laser beam (Laser Quantum Limited, Manchester, England), coaxially aligned with a 633 nm detection beam (He-Ne laser, Research Electro-optics Inc.; Model no. LHRP-0501). The 1064 nm beam is expanded and collimated with the help of lenses L_1 and L_2 before dividing into two parts by polarizing beam splitter BS_1 . The beam is expanded in order to overfill the objective (Nikon, oil immersion, 100X, 1.3NA) - an essential requirement for trapping. Both the beams are again combined using another beam splitter BS_2 after getting reflected from the mirrors M_1 and M_2 . These mirrors are in a plane conjugate to the back focal plane of the objective. The conjugation is achieved with the help of another collimator formed

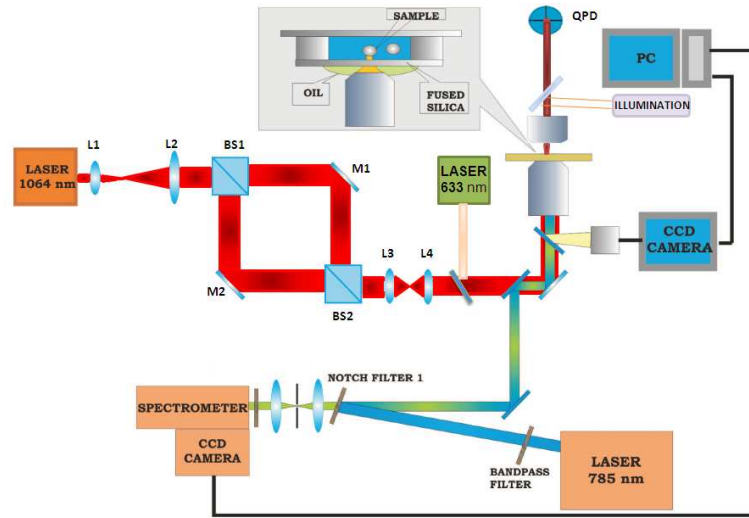


Figure 4.1: A schematic of Raman tweezers set-up with 785 nm beam used for Raman excitation.

by a set of lenses L_3 and L_4 using procedure suggested in [61]. Movement of one of the lenses, L_3 or L_4 , can control the movement of trap in the direction of beam propagation. The movement of either mirrors (M_1 or M_2) will then result in $x - y$ movement of the trap without changes in its intensity and shape, thus keeping the trapping potential of the traps the same. One of the mirrors is connected to a motorized optical mount (Picomotor, New Focus, 8807).

BS_1 and BS_2 also polarize the beams passing through them such that after coming out of BS_2 , both the beams are orthogonally polarized. Hence, the two beams do not have any crosstalk at the focus of the microscope objective, giving us a stable dual trap. The red beam coaxial to one of the trapping beam is used for position detection and force measurement. The forward scattered beam is incident on a QPD (New Focus, model 2991) and gives a high precision information regarding the displacement of the trapped object from the focus.

The second step is construction of confocal Raman microspectroscopy set-up and couple it with optical tweezers in the same microscope as described above. A diode laser (Micro Laser systems Inc.) operating at 785 nm is used for Raman excitation. Depending on the type of measurements, the power of laser is tuned to get high signal to noise ratio without affecting the sample. The Raman section of set-up is shown in fig. 4.2. The beam is filtered using a 780 nm bandpass filter to exclude the broad fluorescence from the diode laser and narrow down its bandwidth. The filtered beam is collimated before it falls on a holographic notch filter NF (Kaiser Optical Systems) at a small angle. The reflected light from NF goes inside an Olympus-IX51 inverse microscope where the object under study is trapped.

The back scattered light is collected from the same objective. This light consists of Rayleigh photons and Raman photons. The beam is passed through the notch filter and a confocal pinhole of $100\text{ }\mu\text{m}$ (P) dimension. The confocal system discards most of the signal coming from out-of-focus region of the objec-

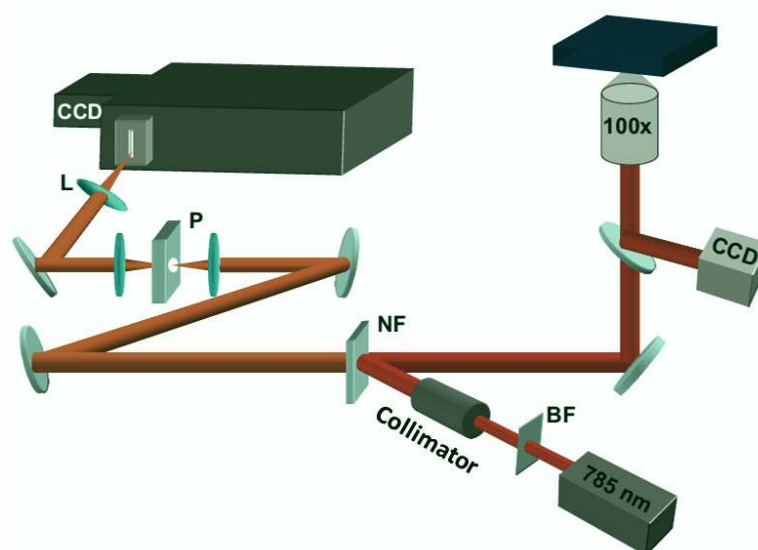


Figure 4.2: A schematic of the confocal Raman microspectroscopy set-up.

tive. The beam is then focused on to the slit of the spectrometer with the help of a lens. The spectrometer is a SpectraPro 2500i, 500 mm focal length monochromator, with a resolution of 0.05 nm at 435.8 nm, containing a 600 lines/mm grating (blazed to 750 nm) and fitted with a Spec-10:100B back-illuminated CCD, cooled down to -80°C . CCDs amplify any noise or signal that comes from the active area of the CCD. Thermal noise is generated by thermally excited carriers in the detector and hence it is required to cool the camera to a sufficiently low temperature to suppress these noise effects. The data from the CCD are recorded using WinSpec software (Princeton Instruments). As we are using an oil-immersion objective, we have to be careful that the oil does not have any fluorescence signal at the wavelength of interest. During our measurements we used cargille immersion oil (type 37).

An additional CCD color camera (JAI) is attached to the microscope in order to take images before, during and after the measurements of single cell and single DNA manipulations. It was also used to capture movies during the experiments.

The other Raman tweezers set-up that utilizes 532 nm wavelength of light for Raman excitation is almost similar in working as the set-up described above, except for certain differences in the components, as shown in fig. 4.3. The trapping is achieved by a diode laser emitting at 985 nm wavelength (Arroyo Instruments). The Raman excitation is done using a 532 nm beam from fiber coupled laser. For Raman spectroscopy it is often better to use near infrared (NIR) wavelength for two reasons. Firstly, NIR reduces the fluorescence signal and secondly, the photodamage to the biosamples is usually less in the NIR wavelength region. But NIR is generally not a suitable candidate for surface enhanced Raman spectroscopy as it is usually far from the surface plasmon resonance of silver nanoparticles of size $\sim 75\text{ nm}$, used widely in experiments.

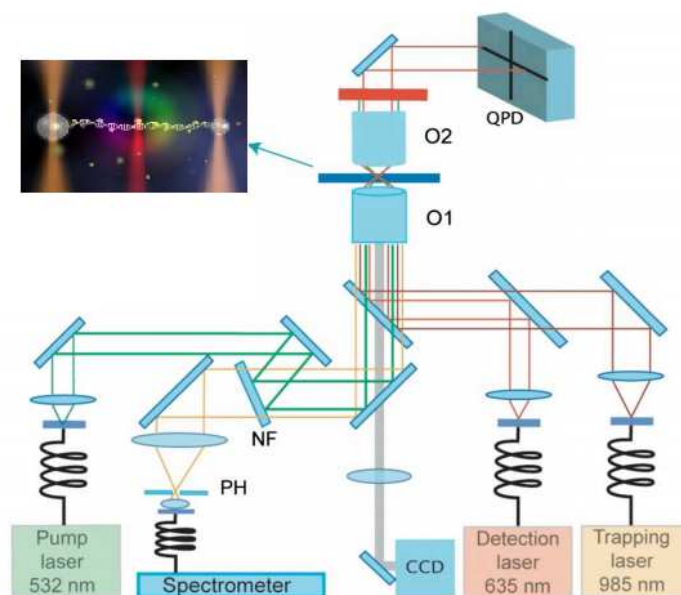


Figure 4.3: A schematic of Raman tweezers set-up used with 532 nm beam used for Raman excitation.

For this reason we make use of green light. The signal is collected from an Andor Shamrock 163 imaging spectrograph and Andor iDus camera.

As this set-up is mainly used for SERS measurements, it is necessary that we synthesize nanostructured substrate for this purpose. For getting this enhancement, we use silver nano-colloids of size ~ 70 nm attached directly to the biomolecules. Another more stable and robust approach is to use a silica bead covered with these nano-colloids and immobilized on the coverslip, to act as a fixed SERS substrate.

4.1.2 Microrheology set-up

The microrheology set-up has been designed in order to measure the effect of mechanical forces of single biomolecules and living cells. The fully steerable dual trap optical tweezers setup consists of two high power, fiber coupled lasers (Manlight : $\lambda_1 = 1064$ nm, $P_1 = 3$ W and Arroyo instruments diode laser: $\lambda_2 = 850$ nm, $P_2 = 200$ mW) used for trapping and manipulation fig. 4.4. Both beams are expanded by a factor of 4 for overfilling the back aperture of an oil immersion objective (Nikon 100X/1.30 NA) for the same reason described above. The 1064 nm beam passes through an acousto-optic detector (AOD, ISOMET LS55) conjugated to the back focal plane of the objective. This allows us to modulate the trap in position without any noticeable change in stiffness. Two trapping beams are coupled using a dichroic mirror before they reach the objective.

Two additional beams of wavelengths 532 nm and 635 nm propagate coaxially with the trapping beams and are used to detect the motion of optically

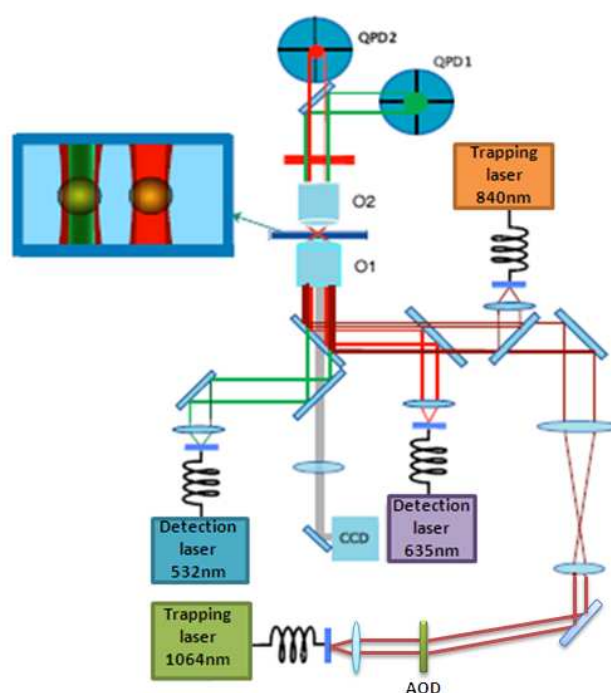


Figure 4.4: A schematic of dual trap optical tweezers set-up used for microrheological measurements.

trapped beads. Fluctuations in positions of optically trapped objects are determined by measuring the detection of the forward-scattered light transmitted through the beads. The forward scattered beams are detected by two identical quadrant photodetectors (New Focus, model 2991). Signals from the detectors are digitized by ADC converter (National Instruments, BNC 2110) and data streaming of time series is performed with LABVIEW. This way we can perform force measurements with very high sensitivity.

A CCD camera (JAI) is installed in order to collect the light used for illumination. This gives the real-time monitoring of particle in the trap. We also use this camera for recording the video of our experiment as well as taking images for image analysis.

4.2 Fluid chamber

For inhibited progress of the experiments, it was important to design a fluid chamber where there can be a constant inflow of the sample. For my experiments, I used an indigenously developed fluid chamber. The design is as shown in fig. 4.5. The basic idea is to sandwich a thin layer of parafilm (Nescofilm, Nesco), with intended channel design, between two coverslips of size zero (Knittel Deckgläser). One of the coverslips has holes of 0.8 mm in diameter, overlap-

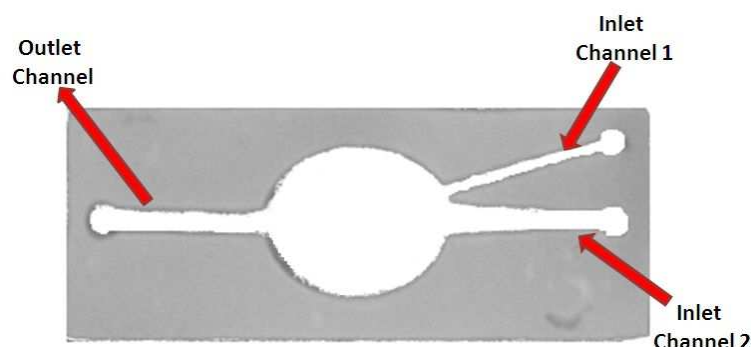


Figure 4.5: One of the various designs of fluid chamber used during the experiments. The basic idea is to draw the desired design over parafilm with help of CO₂ laser and sandwich it between two coverslips.

ping with the holes of parafilm. Depending on the need of experiments we used single channel or double channel chamber. The channels in the parafilm and the holes on the coverslip is made with the help of a CO₂ laser (Epilog mini, 25W). This assembly of coverslip-parafilm-coverslip is then mounted on a custom designed metallic holder. This holder is designed by us and the realization was made with the help of mechanical workshop at ICFO.

The samples are inserted inside the fluid chamber through a standard silicon tube with the help of ordinary 2.5 ml syringes. To manually control the flow, we used a microscrew controlled stage to push the sample inside the flow cell.

As can be seen from fig. 4.5, two different kind of samples are injected through two channels and these two samples mix at the center of the chamber where bead-RBC-bead or bead-DNA-bead construct can be formed *in situ*.

4.3 Sample preparations

For trapping of DNA and RBC with polystyrene bead as handles, I needed to develop an understanding of biochemistry of cells and different beads and learn several protocols for making the construct of beads with biosamples possible. The protocol for DNA is very big and I have put it in appendix. In this section I will discuss protocols regarding preparation of beads for attaching them to RBC and DNA, preparing silver colloids and silver coated silica beads for SERS measurements and RBC sample preparation.

4.3.1 Bead-DNA construct

For making a bead-DNA-bead construct, DNA was incubated with streptavidin (strep) coated polystyrene bead for half an hour and then injected inside the fluid chamber along with anti-digoxigenin (AD) coated polystyrene beads. We use two different type of bead chemistry as we wanted to avoid attachment of both ends of DNA to the same bead during incubation.

Streptavidin coated beads of 1.87 μm size are purchased from Kisker (PC-S-1.5). 20 μl of beads from stock is washed three times in phosphate buffer saline (PBS, Sigma-Aldrich, P4417), pH 7.4 and 140mM salt concentration, at a speed of 13,400 rpm. Finally, the beads are diluted in 200 μl of PBS. We take 5 μl of diluted bead and mix it with 30 μl of PBS and 5 μl of DNA to make a total volume of 40 μl . This mixture was incubated at room temperature for 30 minutes while putting it on a shaker. At last, 960 μl of PBS is added to the mixture to make a total volume of 1000 μl .

For anti-digoxigenin coated beads, 15 μl of protein G coated polystyrene beads (Kisker, PC-PG-3.0) of diameter 3 μm is taken from stock. These beads are washed 3 times, as described above and then resuspended in 30 μl of PBS. To the resuspended beads, we add 5 μl of anti-digoxigenin (Polyclonal sheep, Roche 1333089). This mixture is again incubated as described above and finally resuspended in 950 μl of PBS to make a total volume of 1000 μl .

To form the bead-DNA construct, we inject 500 μl each of AD-beads and strep-beads into the chamber. Both the beads are trapped in the two traps and brought to the touching distance of each other. One of the end (biotin end) of DNA is already attached to strep-bead, the other end (digoxigenin end) gets attached to AD-bead in few seconds as soon as the the beads are brought close to each other. The construct can be tested by moving one of the beads away. If the construct formation is successful, the other trapped beads will also move away from the trap as soon as DNA approaches its contour length. If the other bead does not move then the construct formation is unsuccessful and the same process should be repeated with the other pair of beads.

4.3.2 RBC and bead preparation

Fresh blood sample (30 μl) from a healthy adult is diluted in Alsever's solution (Sigma Aldrich A3551). It is an isotonic balanced salt solution routinely used as an anticoagulant or blood preservation. The red blood cells are then isolated from the blood plasma via a centrifugation process at 2000 rpm and resuspended in 600 μl of Alsever's solution.

100 μl COOH (carboxyl) coated 3 μm polystyrene beads (Spherotech, CPX-30-10) is taken from stock and washed 4 times at 4,500 rpm in 400 μl of 100 mM MES buffer (Sigma Aldrich M1317). The beads are then resuspended in 700 μl of MES buffer and sonicated for 15 minutes. To the resuspended beads 4 mg of *N*-(3-Dimethylaminopropyl)-*N*'-ethylcarbodiimide hydrochloride (EDC, Sigma-Aldrich, 03450) is added. The mixture is allowed to react for 15 minutes at room temperature with continuous mixing. Then 100 μl of lectin (Lectin from *Triticum vulgare*, Sigma-Aldrich, L9640), with a concentration of 2mg/ml is added to the the mixture and incubated at 37 °C for 6 hours with continuous mixing. Lectin solution should be made just before putting it into bead-EDC mixture as it becomes very unstable in liquid form at this concentration. After incubation is over, 30 μl of beads is taken from the mixture and washed two times in 200 μl of Alsever's solution at 4500 rpm and resuspended in 1000 μl of Alsever's solution. The beads are ready to be used for RBC binding. Store rest of the beads at 4 °C. It should be noted that the beads obtained finally after chemical treatment is very sticky in nature and tend to form clumps with themselves. Hence, it is recommended that before using the beads for experiments, it should be sonicated for 15-20 minutes.

4.3.3 Silver colloids

Two methods are used for the preparation of silver colloids for SERS measurements in this thesis. Lee Meisel method, also known as citrate reduction method, and Leopold a Lendl method, also known as hydroxylamine reduction method, are used. Both these methods employ reduction of silver nitrate.

Lee and Meisel method

Silver colloids in this method are prepared by reducing silver nitrate (AgNO_3 , Sigma-Aldrich, S8157) with the help of trisodium citrate ($\text{C}_6\text{H}_5\text{O}_7\text{Na}_3$, Sigma-Aldrich, C3434), according to protocol described by Lee and Meisel [62], with some modifications. 100 ml of 10^{-3} M silver nitrate aqueous solution is heated to boiling ($\sim 90^\circ\text{C}$) and then 2 ml of a 1% (w/v) trisodium citrate solution is added slowly and steadily, while continuously stirring the mixture. The mixture is kept boiling for 1 hour (with stirring on) and then is allowed to cool down. The resultant colloidal mixture is of dark grey color.

Leopold and Lendl method

In this technique, silver colloids are prepared by reduction of silver nitrate by hydroxylamine hydrochloride ($\text{NH}_2\text{OH}\cdot\text{HCl}$, Sigma-Aldrich, 55460), according to protocol described by Leopold a Lendl [63], with some modifications. 90 ml of 1.67×10^{-3} M hydroxylamine hydrochloride solution is obtained in double distilled water. To this solution, 300 μl of 1 M sodium hydroxide is added and the final solution is mixed rapidly. While keeping the stirring on, 10 ml of 10^{-2} M silver nitrate aqueous solution is added very slowly to the above mixture. The mixture is stirred for approximately 20 minutes and taken off. The final result is a solution of silver colloids with dark grey color.

4.3.4 Silver coated silica bead

One of the SERS substrate used during my experiments was obtained by chemically covering a 5 μm silica bead (Micro Particles, GmbH) with silver colloids obtained from hydroxylamine method [64]. To start with, 1000 μl of silica beads is taken from stock and all the liquid in which it is suspended is removed by centrifugation at 3500 rpm for 4 minutes. The beads are then dried overnight at 60°C . Now a solution of 1% APTMS (3-aminopropyl trimethoxysilane) is made in pure ethanol. Then 100 μl of APTMS is added to the dried beads in 900 μl of absolute ethanol. The whole mixture is incubated for 24 hours while stirring it continuously. The beads obtained from above process is then washed three times in 500 μl of absolute ethanol at 3500 rpm for 4 minutes. The supernatant from all three washes is discarded and the remaining beads are dried again at 60°C .

One-tenth of the beads from the dried sample obtained above is redispersed in 1000 μl double-distilled water. Rest of the dried beads can be kept at a cool and dry place for future use. From the redispersed sample, 10 μl beads is taken and is mixed in 940 μl of double-distilled water along with 50 μl of silver colloids obtained from above methodologies. The whole mixture is then incubated at a speed of 300 rpm for 30 minutes. What we obtain as final product is silica beads with a layer of silver nanoparticles over it (fig. 4.6).

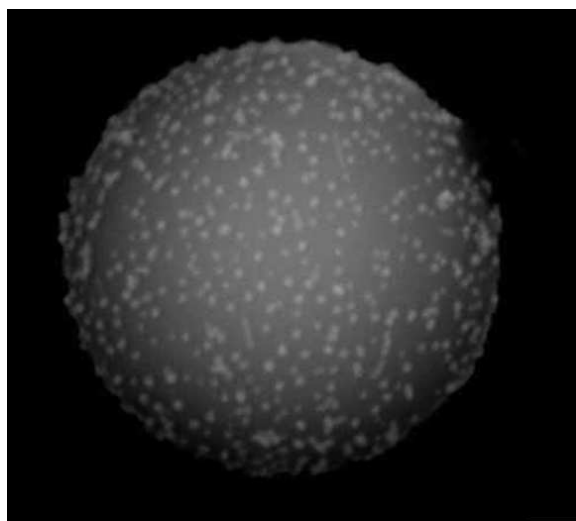


Figure 4.6: SEM images depicting the packing density and homogeneity of silver colloid bound to silane monolayer (APTMS) coated silica beads.

Amount of beads and amount of silver coating can be varied according to the need of experiment. But it should be remembered not to put too much beads at once for the silver coating, as it will hinder the uniform metal coating due to high bead density. To get rid of free colloids in suspension or to change the suspension from DI water to the buffer in which experiments have to be carried out, we can centrifuge the final sample at 3500 rpm for 4 minutes and discard the supernatant. This will remove most of the freely suspended silver colloids. Finally, a solution in which we want the metal coated beads to be suspended is added.

4.4 Statistical techniques used for processing experimental data

The data obtained from spectrometer and QPDs are usually suppressed with various noise and most of the time no proper information can be extracted from these raw signals alone. Hence it is important that we analyze our data properly to reach a certain conclusion. In this section I will describe the techniques that I have used for data analysis.

4.4.1 Processing of Raman signals

Raman signals are weak in nature and are generally accompanied with several noises and background spectra. Hence, it becomes very important that the data are processed properly to generate any discerning information from the signal. The data processing may include some or all steps from following: background subtraction, cosmic ray removal, normalization, smoothing and statistical analysis.

Background subtraction

A major hindrance in most of the spectroscopic studies is a background signal. Whether it is fluorescence, absorption or Raman scattering, the background signal from solvents needs to be subtracted or taken into account. Some of the technical steps that are usually taken in order to reduce background signals are: (i) Reducing the size of entrance slit of spectrometer. But there is a limit up to which we can reduce the slit width as after a certain width we will start to lose Raman signal as well. (ii) By moving the excitation to longer wavelengths and consequently avoiding absorption and fluorescence background in the sample. But going towards longer wavelength region decreases the scattering cross-section and in turn we have lower efficiency of Raman signal. Hence we need to employ some mathematical tools to get rid of background signal.

The background subtraction technique used in this thesis is based on the work done by Mikhailyuk et al. [65]. Briefly, the experimental graph is reconstructed into a geometric curve. The geometric curve has the same unit (for example, pixels) along the coordinate axes, as opposed to experimental graphs which have different units for its axes, for example in Raman spectroscopy its intensity *vs.* wavenumber. Next step is to choose a circle along the curve with a radius that is determined via optimization criteria based on the curvature of the background and the widths of the signal bands. The circle is moved tangentially along the curve and difference values between the curve and the circle are collected via an algorithm. Finally, the algorithm rolls the circle under the curve, erasing the region it overlaps along the way. Since the Raman peaks are usually much narrower than the curvature of the scattering background, a large circle can subtract the background without significantly affecting the peaks.

2D correlation spectroscopy

In the 1980s, Noda did elaborate work on the concepts of 2D correlation spectroscopy [66]. This technique first originated in NMR spectroscopy, but now it finds wide use in various spectroscopic studies. A general scheme employed for implementing 2D correlation spectroscopy is shown in fig. 4.7. In this technique, a sample is subjected to an external perturbation while all other parameters of the system remain unchanged. This perturbation can be a systematic and controlled change in any or all of the following: pressure, temperature, force, pH, chemical composition of the system with time. As a result of the controlled perturbation, the system will undergo variations which can be measured by a chemical or physical detection method, for example Raman spectroscopy in our case. This variation of the system measured as signals or spectra can be processed with 2D correlation analysis for interpretation.

When a spectra consists only of a few bands, it might not be very difficult to determine which bands are undergoing changes. Changes in the band can be caused, for example, by external force. However, for a complex spectra where changes are not so obvious and may contain overlapping bands, the interpretation of the measured signal becomes more tricky. 2D correlation spectroscopy allows one to determine a systematic change in bands, whether it is increase or drop in intensity or changes in the band width or position. The dynamic 2D correlation spectra can be given as:

$$X(\nu_1, \nu_2) = \Phi(\nu_1, \nu_2) + i\Psi(\nu_1, \nu_2), \quad (4.1)$$

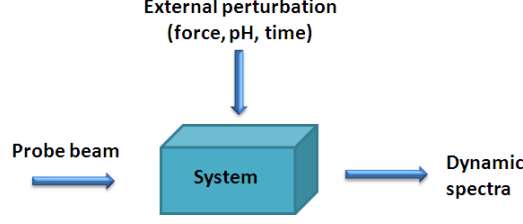


Figure 4.7: Schematic for obtaining perturbation based 2D correlation spectra.

which comprises of real and imaginary part representing synchronous ($\Phi(\nu_1, \nu_2)$) and asynchronous ($\Psi(\nu_1, \nu_2)$) part of the signal. $X(\nu_1, \nu_2)$ represents the 2D correlation spectra of the signal. A 2D synchronous map demonstrates the similarity between two separate intensity variations measured at different spectral variables in the original dataset. It can be mathematically expressed as covariance (or correlation):

$$\Phi(\nu_1, \nu_2) = \frac{1}{T} \int_0^T \tilde{I}(\nu_1, t) \cdot \tilde{I}(\nu_2, t) dt, \quad (4.2)$$

where $\tilde{I}(\nu, t)$ is mean-centered dynamic spectral intensity variations:

$$\tilde{I}(\nu, t) = I(\nu, t) - \bar{I}(\nu), \quad (4.3)$$

with $I(\nu, t)$ being the measured spectra while $\bar{I}(\nu)$ being the mean-centered dynamic spectral intensity variations given as:

$$\bar{I}(\nu) = \frac{1}{T} \int_0^T I(\nu, t) dt. \quad (4.4)$$

Asynchronous map represent sequential or successive changes in the measured spectral series. It is anti-symmetrical along the diagonal and there are no autopeaks on the diagonal. Positive cross-peak indicates that a band from the first spectra grows earlier or is more intensive than a band from second spectra and vice versa. It is given as:

$$\Psi(\nu_1, \nu_2) = \frac{1}{T} \int_0^T \tilde{I}(\nu_1, t) \cdot \tilde{J}(\nu_2, t) dt, \quad (4.5)$$

where $\tilde{J}(\nu_2, t)$ is time-domain Hilbert transform of $\tilde{I}(\nu_2, t)$, given as:

$$\tilde{J}(\nu_2, t) = \frac{1}{\pi} p.v. \int_0^T \frac{\tilde{I}(\nu_2, t')}{t' - t} dt', \quad (4.6)$$

Synchronous 2D map is symmetric with respect to the diagonal ($\nu_1 = \nu_2$). Mathematically, the intensity of peaks located at diagonal positions corresponds to the autocorrelation function and are called autopeaks. They indicate the susceptibility of corresponding bands to the external perturbation.

The off-diagonal peaks are called cross-peaks. Cross-peaks represent how the intensities at two different wavenumbers change with respect to each other.

While the sign of autopeaks is always positive, the sign of cross peaks can be either positive or negative. The sign of synchronous cross-peak is positive if the band intensities at the two spectral variables corresponding to the coordinates of the cross-peak are either increasing or decreasing together as functions of the external variable. On the other hand, a negative sign of the cross-peak intensity indicates that one of the spectral intensities is increasing while the other is decreasing.

Asynchronous 2D correlation spectra along with synchronous spectra gives the complete information regarding the changes. The cross-peaks appear in asynchronous spectra if the fluctuations of signal brought about by a common external stimulus are not completely synchronized. In case of asynchronous, the spectrum is antisymmetric with respect to the diagonal line. The asynchronous spectrum has no autopeaks, and consists exclusively of cross-peaks located at off-diagonal positions. An asynchronous cross-peak develops only if the intensities of two spectral features change out of phase with each other. This feature is especially useful in differentiating overlapped bands arising from spectral signals of different origins.

Principal component analysis

Principal component analysis (PCA) is a multivariate technique used for reducing the dimensionality of a complex spectra and thus present the spectra in a form that can be analyzed in a comparatively easier way. The mathematics behind this technique has been described in detail in [67]. In this technique, a set of observations of correlated variables are decomposed using an orthogonal transformation to obtain a set of values of linearly uncorrelated variables called principal components (PCs). The number of PCs can be less than or equal to the number of original variables. This transformation is formalized in such a way that the first PC accounts for the highest possible variance (i.e. contains maximum information) in the dataset, and each succeeding component in turn accounts for as much of the remaining variability as possible with the constraint that it be orthogonal to (i.e., uncorrelated with) the other components.

Suppose we have a data set of p variables and n samples. The data for each variables are centered around the means. This step make sure that the data is clustered around the origin of our principal components, but does not influence the spatial relationships of the data or the variances along the variables. The first principal components (Y_1) can be written as the linear combination of the variables X_1, X_2, \dots, X_p

$$Y_1 = a_{11}X_1 + a_{12}X_2 + \dots + a_{1p}X_p, \quad (4.7)$$

or, in the form of matrix as,

$$Y_1 = a_1^T X. \quad (4.8)$$

The weights, $a_{11}, a_{12}, \dots, a_{1p}$, are calculated in a way that the sum of their squares is equal to one:

$$a_{11}^2 + a_{12}^2 + \dots + a_{1p}^2. \quad (4.9)$$

Similarly, the second PC can be obtained with the condition that it is orthogonal to first PC and contains the next highest variance,

$$Y_2 = a_{21}X_1 + a_{22}X_2 + \dots + a_{2p}X_p. \quad (4.10)$$

Rest of the PCs can be calculated in similar fashion. All the variables, in terms of their PCs, can be written as:

$$Y = AX. \quad (4.11)$$

A consists of rows of eigenvectors of the variance-covariance matrix of the original data. The elements of these eigenvector are the weights a_{ij} , and are also known as loadings. Loadings plot gives us a summary of variable properties and it is a mean to see a pattern in the data set. The elements in the diagonal of the variance-covariance matrix of the principal components gives us the eigenvalues. Eigenvalues are the variance explained by each principal component, and as explained before, are obliged to decrease from the first PC to the last in monotonous way.

The positions of each observation in this new coordinate system of PCs are called scores and are calculated as linear combinations of the original variables and the weights a_{ij} . Scores plot gives us a summary of the relationship among the observations (or samples).

As reduction of dimensionality is main goal of principal components analysis, several paradigms have been proposed for figuring out how many PCs, of all the PCs present, should be investigated to give a complete representation of data without loss in any information. One common rule is to ignore PCs at the point at which the next PC offers little increase in the total variance explained. Secondly, to include all those PCs which can determine the variance up to 90%. There are other different criteria, but in most cases first three PCs usually are enough to interpret the data set.

4.4.2 Signal from position detector - PSD and CSD

While taking the measurements from a position detector (QPD), we obtain the Brownian fluctuations of the trapped bead. Signals from the detectors are digitized by ADC (National Instruments, BNC 2110) and data streaming of time series is performed with LABVIEW. These signals are in volts and they are converted to nanometer by the methodology described in calibration section of chapter 1. If the trapped bead is embedded in some highly dynamic medium then some information can be found even from the raw data obtained from Brownian motion [68]. But for media with no or less dynamic activity, almost no information can be generated from raw data alone and hence there is a need for processing of this signal to extract some information regarding the medium properties.

One of the simplest and straightforward way to obtain meaningful information is to take the spectral density of the signal. Spectral density function shows the strength of the variations in the signal as a function of frequency. It gives an idea about which frequencies have strong variations and at which frequencies variations are weak. For a single trapped bead, the spectra density is calculated by taking the Fourier transform of autocorrelation function and is known as power spectral density (PSD). It gives the local response of the medium in which bead is embedded. To understand the response of medium at larger length scale, cross spectral density (CSD) is calculated, which is Fourier transform of cross-correlation function. Details regarding calculations of PSD and CSD is given in section 2.3 of chapter 3.

5

Detection of single DNA molecule in optical trap using SERS

Raman scattering is a powerful tool for gaining information on the chemical structure of a studied sample. Recently, Raman scattering has even been obtained from single molecules [48,69,70]. The key element of these measurements is the surface-enhanced Raman scattering (SERS) process where a considerable enhancement of the emitted signal occurs due to coupling of electromagnetic fields with optically excited local surface plasmons in nano-sized metal structures [71].

DNA molecules or their basic constituents in bulk solutions have already been the subject of SERS measurements [72–77]. These works have produced a library of peaks that lead to a well characterized Raman spectrum for DNA. Silver colloids have proven to be effective in detecting single DNA strands as well, however with the DNA immobilized on the surface, which allows for a higher number of metal nanostructures to be in contact with the molecule and easier positioning of the excitation light field [13,78].

Here, we believe we demonstrate for the first time the use of SERS in the spectroscopic detection of a single DNA molecule that is optically trapped in a natural aqueous environment [15]. Two optically trapped dielectric beads are used as anchors while the DNA is suspended in a solution with nanosized silver colloid particles. The colloidal particles non-specifically bind to the DNA and enhance the Raman scattering that is excited by a near-infrared beam. Raman spectra show the presence of known vibrational bands of DNA and a force-extension curve verifies the single DNA molecule.

5.1 Experimental method

The molecule used was double-stranded λ -DNA amplified at 12 kbp from *E. Coli* using standard polymerase chain reaction (PCR) techniques with sam-

ple concentrations of 40 ng/ μL . The DNA molecules were tagged with biotin and digoxigenin (DIG) at each end in order to attach to streptavidin and anti-digoxigenin (anti-DIG) coated polystyrene beads, respectively. DNA molecules were first incubated with the streptavidin coated beads (1.87 μm diameter) for 30 minutes in phosphate buffer solution (PBS) at pH 7.4. The sample was then washed before being injected along with the anti-DIG coated beads (3.15 μm diameter) into a home built fluid chamber with separate channels for the injection of the beads leading in to a center channel through which passed the optical beams. The final DNA-bead constructs were realized *in situ*. Silver colloids with an average size of 70 nm were produced by the citrate reduction method [62] at a concentration of 5×10^{11} particles/ μL , as described in chapter 4. A minute quantity of NaCl was also added which provides the salt-induced activation of the colloids and neutralization of the surface charge of the metal particles thus promoting non-specific binding to the negatively charged DNA molecules. Silver colloids diluted in PBS were injected in to the chamber at a concentration in order to achieve an Ag particle:DNA molecule ratio of approximately 5:1. Measurements were conducted after a few minutes wait time in order to allow the diffusing and binding of the metal particles to the DNA.

The experimental setup is a combined optical trapping system with confocal Raman spectroscopy and has been discussed in details in chapter 4. Briefly, a 785 nm beam was used for the Raman excitation with an average power of 5 mW at the sample. The solution with DNA molecules and functionalized beads were placed inside the flow chamber. The chamber was placed on an inverse microscope equipped with a 100×1.3 NA oil immersion objective. The backscattered light was collected by the same microscope objective and passed through a holographic notch filter before entering the confocal system with a 100 μm pinhole. Raman spectra were recorded with a spectral resolution of 3 cm^{-1} .

1064 nm optical beams were used for the dual trap with an average power of 10 mW at the each bead. For the measurement, we held the beads attached to the DNA and aligned it such that the Raman excitation beam passed between the beads (see Fig. 5.1). An additional 633 nm optical beam was coaxial to the propagation direction of one of the trapping beams. Its forward scattering intensity was characterized with a pinhole and a quadrant position detector in order to calibrate the optical traps using well established procedures [37] and measure the extension curve of the DNA molecule.

5.2 Results and discussions

For the experiment, live Raman spectra were recorded successively at 1 s acquisition time in order to adjust the position of the molecule based on the intensity of the Raman peaks. A 10 s acquisition was then performed, and once the DNA Raman peaks were observed, an extension curve was measured by stretching the DNA and recording the position of one of the trapped beads. Fig. 5.1 presents a Raman spectrum that is typical of the successful measurements from the sample set. The spectrum shown in grey is plotted directly from the spectrometer, without any smoothing or background removal. A background curve was also measured in the same conditions, with the DNA moved away from the trap until the signal disappeared from the short time live scans. The background is

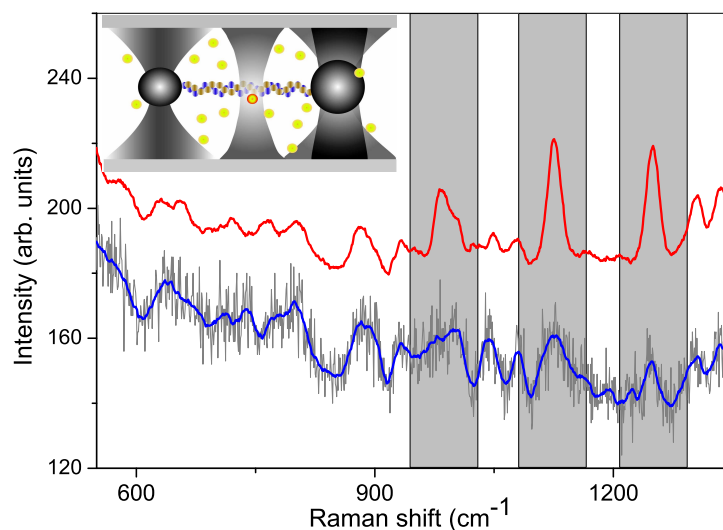


Figure 5.1: A spectrum (top plot) from a typical SERS measurement of a single DNA molecule plotted against a background spectrum (bottom plot). The raw data (gray line) are plotted with their smoothed counterparts (Savitzky-Goley, 30 points) for both the DNA (red line) and background (blue line) spectra and are shifted for clarity. Inset: an illustration (not drawn to scale) of the DNA-bead construct in the optical trap.

not quite as smooth as one would expect from water at near-infrared excitation. During a 10 s acquisition it is possible that loose DNA and other particles along with colloids could diffuse in and out of the excitation volume leading to the noisier background. However, distinct bands emerge when the trapped DNA is brought in to the confocal volume. We consistently observe three bands. The first, at 1265 cm^{-1} , is assigned to the C-C and C-N stretching vibrations (out of phase) of the base residues, in particular to the aromatic skeletal vibrations of cytosine. The peak at 1140 cm^{-1} is attributed to the deoxyribose-phosphate backbone and the C-O stretching in the deoxyribose gives the Raman peak at 1000 cm^{-1} [79, 80]. These peaks have previously been observed to be strongly enhanced through interaction with Ag colloids [78, 81]. We must point out the absence of the highly SERS active adenine modes which have been observed in single stranded DNA [77] and at single molecule concentrations in solution [76] with silver particles. Initially, one can consider that the double stranded DNA does not allow direct contact of the bases to the metal, however a strong adenine SERS peak was also observed for dsDNA adsorbed on to gold [75]. Further studies must be performed that consider the DNA-metal interaction in order to shed more light on the specific conformations of DNA structure at the metal surface. The non-specific binding of the Ag particles means that the distribution of the particles on the DNA is random. This was most likely the major cause for the lack of Raman signal from some of the molecules: at times there were no metal particles in the confocal volume. The fluctuating DNA molecule in the optical trap moves the excited colloids. However, the micron cubed focal volume, which is much bigger than the width of the DNA and metal particle,

and our setting of the DNA at about 70 % extension before measuring Raman signal combined to minimize this fluctuation, as could be seen in the live 1 s acquisition scans.

To verify that the Raman signals originate from a single DNA molecule, force-extension curves [82] were measured of the DNA molecules that produced a Raman signal. Fitting the curves in Fig. 5.2 to the well established worm-like chain (WLC) model [83] allows two basic parameters to be extracted: the contour length (L_0) and persistence length (P) (formula given in Fig. 5.2a inset). In all measurements, the measured contour length, at $4.1 \mu\text{m}$, was consistent and verified our amplification protocol for this length and the rough length estimate found with electrophoresis.

The final confirmation of a single DNA molecule between the beads should be the extension curve fitting to the DNA natural persistence length of 53 nm [82,84]. This value would change proportionally to the number of molecules being extended. In the sample set, the persistence length values ranged between 47-57 nm which is within reasonable error of the well-established value for a single DNA molecule. Most likely due to the metal particles, the fits are not as good as what is typically seen for these types of measurements. Thus, in order to ensure that the curves are beyond a reasonable error range from a multi-molecule ensemble, theoretical force-extensions curves for two persistence lengths, 53 nm and 26 nm, are included in Fig. 5.2 with the experimental data and original fit (where all parameters were allowed to vary). The lower persistence length estimates the effective rigidity of two DNA molecules which forces a large deviation of the WLC model from the experimental data. However, the 53 nm value for a single DNA molecule is extremely consistent, not even changing more than 5% at different pH conditions [82]. This leads to our conclusion that although our measured values indicate a single DNA molecule, the mechanics of the DNA are being affected by the attached metal particles.

The WLC fits are weakened by the higher force values in the region between 80% ($3.3 \mu\text{m}$) and 88% ($3.6 \mu\text{m}$) extension or 0.5 - 1.5 pN. The region is representative of the DNA transitioning from entropic dominated forces to acting like a structure with an intrinsic elasticity [85]. The attached metal particles do not seem to affect the entropic forces that are necessary to straighten the DNA nor the linear elastic region at higher forces. The average diameter of the silver particles is larger than the persistence length of DNA. Thus, if there are clusters of few Ag particles, the DNA could tend to coil around the metal rather than taking on a rod-like behavior with just one particle. The force needed to uncoil these segments would certainly occur at low values, because of the non-specific binding, but should be greater than what is needed to straighten the DNA to a rod at normal aqueous and thermal conditions. The absence of an effect at longer extension, or larger forces, is also due to the size of the metal particles, but this time in an opposite way. The nanometer sized diameters of the metal particle or clusters are much less than the microns length scale of the DNA, leaving stretching forces in the length direction unaffected when the DNA is acting as a rod with a finite stretch modulus. This is also dependent on the low density of metal on the DNA molecule, which is confirmed from the concentrations used.

This technique of the single molecule DNA detection offers distinct advantages over the current methods of studying single DNA spectroscopically that require the DNA to be stuck to a surface in order to realize the reproducibility

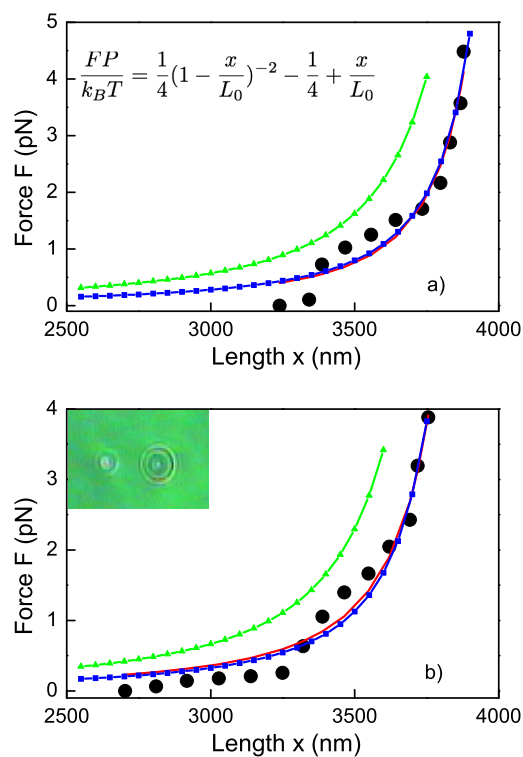


Figure 5.2: A sample of two extension curves from the data set of DNA molecules that gave a Raman signal at the conditions of Fig. 5.1. The curves are fit to the WLC model (red line) (formula in (a) inset) and all curves give the expected contour length (L_0) of $4.1 \mu\text{m}$ and persistence lengths (P) that vary between 47 - 57 nm. In the two examples given here, persistence values of (a) 55 nm and (b) 48 nm were found. Error bars are calculated to be far less than the size of the plotting symbols and are therefore not shown. Theoretical force-extension curves are included using the expected contour length and persistence lengths of 53 nm (blue line-square) and 26 nm (green line-triangle) in order to further demonstrate the presence of a single DNA molecule. A camera image of the suspended DNA-bead construct is included in (b) inset.

of the metal coverage [78] or laser excitation in a TERS configuration [13]. Of course, this leaves the DNA in a static unnatural state which is sufficient for DNA sequence studies, however, one can envision with the current configuration correlating DNA Raman signal with the force sensing and manipulation aspects of the optical trap. This could add a new dimension to dynamical studies of structural conformation, such as extension or twisting, or even protein diffusion along the DNA.

6

Structural rearrangement of DNA at low forces revealed by SERS

The DNA molecule acts as a platform for a host of critical functions such as transcription, replication, and other molecular motor driven processes, where the DNA strand undergoes numerous mechanical events that are primarily supported by the polymer-like phosphate backbone. As a passive substrate, DNA maintains mechanical compliance to allow interactions with proteins. Some of these interactions occur at low forces where the mechanical load on DNA is balanced by lowered entropy via unfolding. Thus, understanding DNA structural responses in this entropic regime is essential to elucidate overall DNA function.

The advancement of single molecule force spectroscopy (SMFS) has connected physiological function to molecular level processes, for example, with DNA [4, 86]. A typical SMFS experiment provides force measurements which are related to models that idealize the molecule mechanically [87]. Advancements in instrumentation have pushed length scale resolution limits leading to dynamical studies of active processes [88]. However, these experiments are either limited to measuring a few averaged parameters or require advanced particle tracking with fluorescence probes [18]. The use of fluorescence imaging is generally applicable to strong topological changes [20] occurring in higher force regimes. More importantly, light interacting directly with chemical bonds would provide a more ideal measure of the DNA structure.

Raman spectroscopy is well suited to be a radical complement to SMFS, as it provides the highest level of chemical structure information with minimal external interference due to its fundamental scattering process at all optical wavelengths. Raman studies of DNA have been conducted for two decades and have produced a database of Raman peaks that characterize the various components of the DNA structure [72, 79]. Raman signal can be amplified by metal nanostructures through plasmonic effects [71] which makes possible single DNA molecule detection [13, 48, 76]. The drawback is that the DNA or its constituent samples are measured as an ensemble or anchored to hard sur-

faces; far from an ideal physiological state. We have previously demonstrated a methodology to overcome some of these issues by optically trapping single DNA molecules [15] with silver nanoparticles nonspecifically bound to the phosphate backbone, which made possible the Raman detection of single molecule DNA in its natural aqueous environment.

In the previous chapter we have shown Raman spectra from single DNA molecule in physiological conditions [15]. But it had two main drawbacks - firstly, both DNA and silver colloids have negative charge and hence colloids are not so easy to get attached to DNA. Secondly, if we stretch DNA, colloids stuck to its surface will also move, hence denying us the signal. In this work, we demonstrate a novel combination of optical tweezers and SERS to study DNA structural responses from an applied load in the low force, entropic regime. A single DNA molecule is optically stretched close to an external SERS substrate while its Raman spectrum is simultaneously measured. We identify a correlation between the phosphate backbone structure and molecular extension. The results of this novel experimental technique are confirmed with state of the art theoretical modeling, which combines molecular dynamics (MD) with mixed quantum mechanics/molecular mechanics (QM/MM), to compute Raman modes for DNA structures modeled at different extensions. The overall result demonstrates a structural response in a regime where mechanical load is thought to only be countered by entropy changes. We also highlight an innovative methodology for directly observing single molecule chemical structure changes in response to controllable forces.

6.1 Experimental methods

The experiment (see inset Fig. 6.1) consisted of DNA-bead constructs, double-stranded λ -phage 12 kbp DNA (4.25 μm contour length) molecules anchored to silica microspheres, manipulated in solution with a dual optical trap. The molecule was brought close to a SERS substrate, 5 μm silica beads with silver nanoparticles (70 nm) [62] attached to their surface [64], that had been previously deposited on the glass surface. Additional beams passed through the system for bead position tracking and Raman excitation. For the experiment, the DNA molecule is extended in increments while the Raman signal is detected at each step.

6.2 Results and discussion

Figure 6.1 shows a typical series of Raman spectra from a single DNA molecule at three different extensions where a difference in some peak positions between spectra is immediately clear. The plotted region contains stretch vibrational modes of the phosphodiester network (C-O-P-O-C) and C-N bonds in the cytosine base [79], with bands at lower and higher frequencies containing bending and scissor modes, respectively, that are not typically SERS active. We note, as in our previous studies [15], the absence of the adenine SERS peak that has been observed in single stranded DNA [77] and from single adenine molecules in silver colloid solutions [76]. This may be due to the less understood interaction between silver and the double strand which may cause shielding of the other

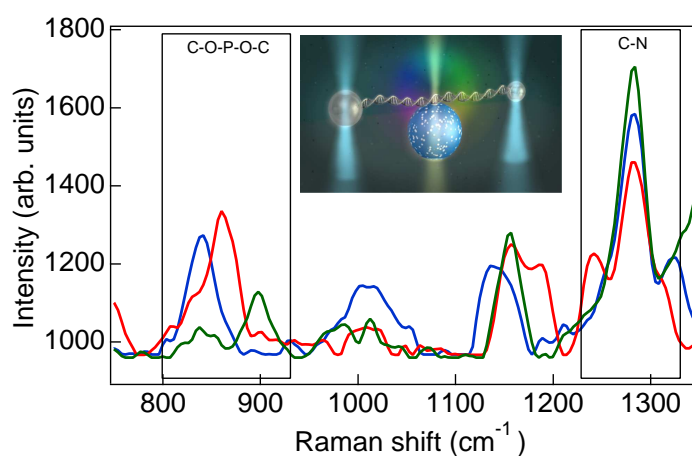


Figure 6.1: Raw Raman spectra from a single DNA molecule at three different extensions: 3700 (blue), 3800 (red), and 3900 (green). The O-P-O Raman band in the 800 - 900 cm^{-1} range undergoes an upward shift in position while the C-N vibration (1280 cm^{-1}) remains constant as the molecule is extended. Inset: Depiction of the experiment where Raman scattering and mechanical extension are simultaneously measured utilizing a dual optical trap and Raman excitation of the molecule close to the SERS bead.

bases from the silver nanoparticle plasmonic fields.

Raman spectra from measurements of 5 DNA molecules at all extensions are grouped together and cross-correlated via a 2D correlation analysis [66] to identify peak movement in the sample set. Peak position trends will emerge as hotspots in *both* the in-phase (synchronous) and out-of-phase (asynchronous) maps. Features between 800 - 900 cm^{-1} band, where stretch modes of the O-P-O unit lie, are present in both maps, signifying a displacement of this band with extension (Fig. 6.2). The doublet spot is due to a shift greater than the width of the peaks. The C-N stretch mode of the cytosine ring, 1280 cm^{-1} , only has an in-phase feature due to an intensity change with no position shift in the peak. Generally, intensity changes of SERS spectra are difficult to interpret because the enhancement level can vary due to differences in the relative positions of the SERS substrate, molecule, and incoming excitation light [89]. This also led to a few occurrences of a large peak at 1200 cm^{-1} that cause lines of spots in the maps at this position which we deem to have no physical significance. While intensities are solely dependent on the interaction of the chemical bond with light, band positions also depend on bond symmetry and polarizability which is a direct consequence of the conformation of the bond. Thus, Raman band position changes are expected to correlate with mechanical alteration of the local structure [90]. We conclude that the 800 cm^{-1} phosphodiester stretch mode is sensitive to molecule extension while the cytosine mode is unaffected. A similar sensitivity of the O-P-O stretch mode was previously observed, where an upward shift of the band is present between looser wound A-form DNA and tighter wound B-form structures [79].

Figure 6.3a is a plot of Raman peak position versus extension for all mea-

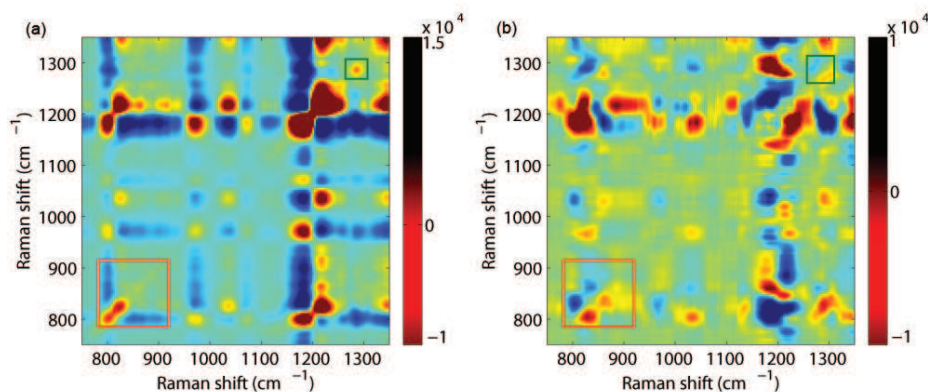


Figure 6.2: 2D correlation maps (synchronous **(a)** and asynchronous **(b)**) from Raman spectra of 5 different molecules that were extended. The signatures in both maps (boxes) together indicate a shift in peak position of the O-P-O Raman band ($800 - 900 \text{ cm}^{-1}$) while the C-N cytosine base vibration (1280 cm^{-1}) remains constant during the molecule extensions. The large spots along the 1200 cm^{-1} axes are due to a large random peak that appeared at this position in two of the spectra which is common with SERS.

measurements. The plots contain the phosphodiester and cytosine base stretch modes that had distinct spots in the correlation plots. Owing to the known high mechanical uniformity between DNA molecules, the majority of error will lie in the Raman peak positions. A small spread in the extension points is due to uncertainty in the starting extension, because each molecule must be stretched to a finite initial length in order to be approached to the micron sized SERS substrate. The effect is immediately clear: the phosphodiester mode shifts while the cytosine mode remains unaffected during the DNA extension. Assuming a linear relationship, the most striking parameter is the sensitivity of the phosphodiester Raman band to the force-extension, $0.11 \text{ cm}^{-1}/\text{nm}$. Given a spectroscopic resolution of our system to be 3 cm^{-1} , this demonstrates that our combined SERS-optical trapping technique is sensitive enough to measure DNA structural changes at sub-pN forces, translating to a minimum unfolding of approximately 10 base pairs to give a detectable phosphodiester Raman peak position shift.

We performed simulations with density functional theory (DFT) normal mode frequencies to confirm the modes above and their sensitivity to extension. The modeled structures [91] were 30 base pairs long with only cytosine-guanine base pairs, which minimized the number of theoretical modes that are not measurable in the experiment. Four lengths were tested: 97 (unextended), 120, 135 and 155. The theoretical structure extensions were higher than in experiment due to the long computational time necessary to resolve smaller extensions (forces). For each modeled structure, normal mode frequencies were calculated for three adjacent segments on each chain, with each region containing two base-pairs and surrounding sugars for a total of 134 atoms.

Raman active modes were determined by computing the frequencies and Ra-

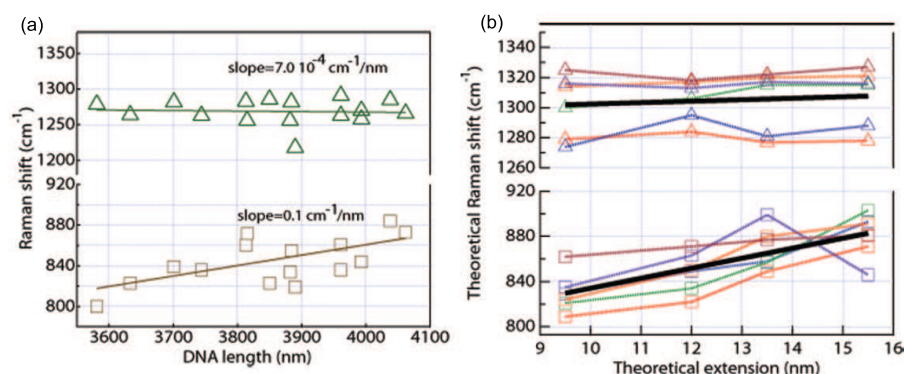


Figure 6.3: Experimental (a) and theoretical (b) plots of Raman peak position versus DNA extension for the O-P-O phosphate backbone and C-N cytosine base stretch modes. The points from all 5 molecules and all 6 calculated regions are plotted together for the experimental and theoretical plots, respectively. The data sets are fit to a straight line and the slopes are included for the experimental data.

man activities of a reduced structure, which consisted of a single phosphodiester network between a guanine and cytosine base. The phosphate vibration with the highest Raman activity in the vicinity of 800 cm^{-1} prominently involves a single O-P vibration but includes motion throughout the phosphodiester chain (C-O-P-O-C), while the 1280 cm^{-1} cytosine peak comes from a C-N vibration in the cytosine ring. Figure 6.4a depicts the identified motion of the phosphate mode. Identifying the motion in the reduced system allowed us to locate the corresponding band in the full DNA structure computation and track it through the different extensions. The computed modes for each region are plotted versus extension in Fig. 6.3b. Once again, the phosphate stretch mode shows sensitivity to DNA extension while the cytosine base remains unaffected.

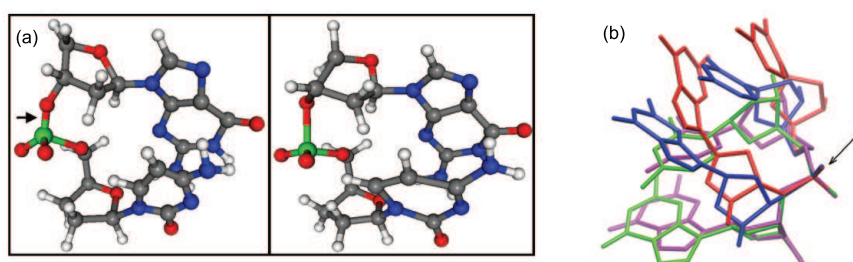


Figure 6.4: Theoretical snapshots (a) of the O-P-O vibrational mode responsible for the 800 cm^{-1} Raman peak taken from the reduced structure calculation used to determine the Raman activities. An overlay (b) of the calculated DNA structures focused at a single region, with the phosphorus atom (arrow) as the common origin: 97 (blue), 120 (red), 135 (green), 155 (purple).

The Raman frequency of a vibration can change due to an alteration of

the mechanical and electromagnetic components of the bond. The increase in the phosphate mode frequency is a result of an alteration in geometry and energetics of the system as the molecule is extended. Figure 6.4b is an overlay of the modeled structures with a single calculated region of the DNA chain isolated and the phosphorus atom as the common origin. The orientation of the O-P-O unit remains constant and the O-P-O bond angle shows no correlation with extension (data not shown). The orientations of the carbons and adjacent sugars relative to the O-P-O unit change drastically, however. Nearest neighbors reconfigurations can affect the bond's polarizability and its interaction with light via Raman scattering by changing the symmetry of the local region. From an energetics standpoint, the region experiences a mechanical perturbation as the structure is extended. The total end effect of the above is a shift in the bond's Raman peak position.

The DNA structural alterations observed here at small forces should aide in understanding DNA-protein interactions in the entropic regime. Although DNA can be modeled as a semi-flexible polymer, the result shows that chemical bond orientations are involved and can be sensitive to mechanical loading at all scales. The technique is a novel combination of known methodologies that provides a new addition to the SMFS field. By directly measuring at the bond level with Raman scattering, these structural shifts can be observed at low forces without the need for complex particle tracking. Most importantly, with the constant advancement of SERS substrates, the stability and amplification level will continue to improve while maintaining the DNA strands free of optical probes and leaving them in a more ideal physiological condition.

7

Single red blood cell under tunable external force studied by combining passive microrheology and Raman spectroscopy

Nowadays human blood and urine are probably the most common samples submitted for medical diagnosis because they are easily accessible and provide a lot of useful information about donor's health conditions. Red blood cells have relatively simple architecture (a composite of lipid bilayer with embedded proteins and an underlying cytoskeleton without nucleus and intra-membrane organelles) and is usually considered as an ideal system for modeling single living cells [92]. One of the most important properties of RBC is its deformability which describes the mechanical response of the cell to a deforming force. Deformability of RBC is known to be extremely high which is essential in gas transport between blood and tissues in microcirculation [93]. In particular it allows RBCs to flow through microcapillaries with inner diameter typically less than half the diameter of the cells. This extraordinary property has been attributed to several factors: cell shape, viscosity of intracellular fluid, and rheological properties of the membrane [94]. The latter, as previously demonstrated by Suresh et al., can also be affected by some human diseases such as malaria, spherocytosis, elliptocytosis or sickle cell anemia [95]. In human body, RBC adopts different stretching states caused mainly by blood flow and associated cell squeezing.

Full understanding of RBC's mechanical behavior requires that we investigate response of cell to externally applied forces. Despite experimental difficulties, this problem has been partially addressed earlier by deformability measurements using pipette aspiration [96, 97]. In recent years the interest in this area has grown significantly mainly because of huge development in microscopic manipulation techniques such as optical or magnetic tweezers which

can monitor/impose force (displacement) to a resolution of the order of tens of femtoNewton (nanometer) [98]. They provide excellent methods for probing single living cells at different conditions giving potentially powerful tools for diagnosis and treatment of disease [92]. So far most of the rheological studies have been carried out by measuring the static changes of cell length [99–102] or area expansion [103] in response to a deforming force. On the other hand RBC in normal conditions (in human body) experience a wide spectrum of dynamic forces associated with thermal fluctuations, blood circulation or materials transport through the membrane. In particular, specific chemical reactions, such as oxygenation and deoxygenation, can be induced by stretching [104].

It is well known that in addition to static rheology, dynamic viscoelastic properties of different materials can be probed using one or two particle passive (or active) microrheology approach which differs from each other in experimental and theoretical points of view [105]. These methods are particularly valuable because, for example, in homogeneous, isotropic medium they allow for direct detection of both real and imaginary part of complex shear modulus at different frequencies. The main advantage of passive rheology (used in this work) in comparison to active is relatively short time required to record fluctuations simultaneously at wide range of frequencies. In contrast, in active rheology the response function is obtained straightforward but the scan over all required frequencies has to be performed. This time consuming measurement might lead to mechanical cell degradation depending on applied amplitude of modulation. Also heating via particles can not be excluded and special care has to be taken to reduce time of experiment. Single particle passive microrheology is the simplest form where the viscoelastic properties are extracted from the power spectral density (PSD) of thermally fluctuating probe position. Main limitation of this approach is significantly shorter probe length scale which is similar to the probe size [12]. On the other hand interaction between two probes at some separation (which can be much longer than probe size) opens up the possibility to examine a medium on length scale comparable to the distance between the probes. If a medium with defined geometry (like RBC) is placed between two fluctuating probes, their correlated motions are supposed to be mainly determined by the properties of this medium.

Although elasticity of human red blood cells has been of scientific interest for a long time, little is known about the dynamic response of cell (particularly at higher frequencies). Complete understanding of RBC's mechanics and functioning also requires that we consider molecular changes induced by deformation in cell. A link between viscoelastic response and changes in molecular structure is obvious, however there are no such studies till now. Fluorescence and/or Raman spectroscopies are the best candidates to demonstrate correlations between rheological behavior and changes in molecular structure. Raman spectroscopy provides the highest level of chemical structural details with minimal interference from outside sources, due to its fundamental scattering process that functions at all optical wavelengths. Raman studies of RBC or their basic constituents have been presented for several decades ([106–110]) and have produced a database of Raman peaks that characterize the various constituents.

The combination of two measurements: microrheology and Raman spectroscopy performed at different forces is a potential tool to establish crucial linkages between structure, mechanical properties and functions of the cell. To the best of our knowledge, reports regarding frequency dependent behavior of

RBC with only one end attached to the bead and the other end stuck to the surface of a cover-slip have been shown earlier [111,112]. More recently Yoon et al. [113] reported two probes rheology of single RBC but in limited frequency range, mainly due to the applied detection method, where particle fluctuations were recorded by a CMOS camera at frame frequency rate of 470 Hz. So far however, the comparative study of one and two probes microrheology of single RBC, supplemented by Raman spectroscopy, has not been presented yet.

Main aim of this work is to explore viscoelastic properties of the cell measured in the extended frequency range via single and two particle microrheology, providing comparison between local and overall properties of RBC. The second purpose is to associate mechanical properties of single cell with the changes observed on molecular level measured via Raman spectroscopy.

7.1 Materials and methods

Section 4.1.1 and section 4.1.2 of chapter 4 describes in details the set-ups for Raman spectroscopy and microrheology respectively. The RBC sample and beads were prepared as described in section 4.3.2 of chapter 4. Samples were injected into a homebuilt two-channel fluid cell whose position was fully controlled by a piezostage (PiezosystemJena NV40). The flow in the chamber was precisely dosed by a syringe coupled with a picomotor (New Focus).

The measurements were made in similar fashion as in [104], with three main differences. Firstly, we attached polystyrene beads at two opposite ends of the cell, as described below. This allowed us to use higher power of trapping beams with lower photodamage to the cells. Hence we could stretch the cells more compared to [104]. Secondly, as changes in the membrane is the main focus of this study, Raman beam was aligned to preferentially excite the edge of the trapped cells. Finally, unlike [104] where only cells that initially gave oxy Raman peaks were considered, we did not select the cell using this criteria. A Raman signal was collected for 30 seconds at relaxed and about 10-15 different stretched states (till one of the beads came out of the trap). Whole process was repeated on about 15 different cells. We observed similar patterns of Raman spectra in majority of the cells. Measured Raman spectra were background subtracted, normalized using Multiplicative Scatter Correction (MSC) and smoothed using smoothing spline technique [114].

7.1.1 Bead-RBC-Bead construct

Passive microrheology and Raman experiments were performed using bead-RBC-bead construct which was floated well above the glass slide surface like in [115]. This construction minimizes hydrodynamic drag from the glass surface of the fluid chamber and isolates samples from mechanical vibrations of the chamber. The construct was made according to following procedure. Both, beads and RBC solutions, were separately injected to different channels of the fluid chamber. This way we can avoid uncontrolled pairing of RBC with beads. Firstly, two beads were optically trapped at a known separation between them. The thermal fluctuations of these two beads were recorded simultaneously by the position detection systems. These data were then used for the trap calibration and also for calculations of rheological properties of solvent as a control and

for comparison. Next the RBC solution was slowly injected (so that to avoid removing the beads from their traps) and cell was trapped in a third trap located between two beads. This additional trap was made using the AOD in time sharing (10 kHz) regime. The power of additional (third) trap was significantly reduced to minimize the heating of RBC. The stiffness and position of this trap were controlled by modifying electrical signal (amplitude, frequency and width of rectangular pulses) driving the AOD. The RBC, which was already placed between two beads, was first connected to one of the bead by changing the modulation amplitude of time shared trap. Second bead was attached by changing deflection of the beam using AOD. The relatively larger size of beads ($3 \mu\text{m}$) was chosen to reduce possible heating of RBC [116]. Once the bead-RBC-bead construct was achieved, the time-sharing regime was switched off and hence the RBC was not under direct influence of trapping laser for the whole experiment.

7.1.2 Data analysis method

Detailed theoretical description of one and two probe microrheology including trap correction has been mentioned in section 3.1.3 of chapter 3.

Since the system is inhomogeneous and anisotropic, the shear modulus G cannot be simply derived from the response function using the Stokes-Einstein relation. Instead, the effective stiffness of the system describing viscoelastic properties was calculated by simple inversion of trap corrected, medium response function [113]:

$$K = \frac{1}{\alpha} \quad (7.1)$$

Fluid and particle's inertia in these equations have been neglected, which is a good approximation at low frequencies and relatively small distances between the particles studied here, particularly if only the parallel case is taken into account [10, 105].

Fluctuations of two particles (in the absence and presence of RBC) were recorded simultaneously with sampling frequency of 20 kHz for 2 minutes. Next the DC component was removed and noise-reduced PSD and CSD were computed by averaging together the power spectra of short segments of the data [117]. In order to further reduce the noise, randomly distributed points were obtained in log scale and to speed up the above mentioned calculations both PSD and CSD were log-binned [118] before the response functions were obtained according to eq. (3.45). Data were processed using Igor 6.2 program (Wavemetrics).

The distance between trapped beads was estimated from the microscope images based on the knowledge of beads diameter. The center of beads was found by fitting the ellipse to the boundary of each particle using "Imageanalyzeparticles" function implemented in Igor 6.2. The distance between centers was converted from pixels to micrometers using an average calibration factor calculated based on *a priori* known beads diameter. The initial diameter of all the cells was found to be in the range of 6 - 7 μm .

Trap stiffness measurement and calibration of both traps were achieved using the method described in section 1.2 of chapter 1. Lorentzian fitted PSD data for both the traps are shown in Fig. 7.1. Although the detection beams were readjusted to pass through the center of the trapped bead, sometimes a small but definite change in the overall intensity of the forward scattered light was

observed. The calibration factor used for each stretch was normalized with respect to the intensity of the forward scattered light when the bead was not attached to the RBC.

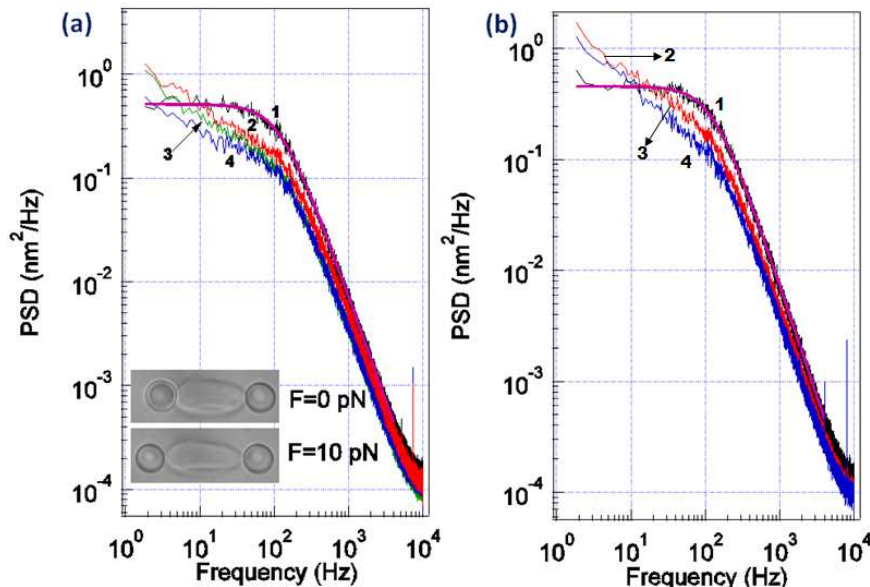


Figure 7.1: Power spectral density of the single particle fluctuations for left (a) and right (b) trap in the absence ((1) black) and presence of RBC and different forces applied to the cell (red (2) - the cell at rest, green (3) - the cell stretched by 12 %, and blue (4) - the cell stretched by 16 %). Spectrum obtained in the absence of RBC is fitted with Lorentzian function (pink solid line) and used for calibration purposes as described in the text. Inset shows the images of bead-RBC-bead construct for relaxed and stretched state taken by the microscope camera.

Knowing stiffness of the traps, the force can be determined by multiplying it by particle displacement. In this work the force was calculated based on displacement of the bead in the unmovable right trap (see inset in Fig. 7.1a).

7.1.3 Drag correction

Hydrodynamic drag γ strongly depends on the distance of particle from the surface. This effect becomes important when the distance from the surface is comparable to the particle radius and then drag dramatically increases near the surface. Although all the measurements were done well above the coverslip surface, nevertheless, the drag was corrected for surface proximity using Faxen law [31]:

$$\gamma_{corrected} = \frac{\gamma}{1 - \frac{9}{16}\left(\frac{R}{h}\right) + \frac{1}{8}\left(\frac{R}{h}\right)^3 - \frac{45}{256}\left(\frac{R}{h}\right)^4 - \frac{1}{16}\left(\frac{R}{h}\right)^5}, \quad (7.2)$$

where h is the distance from the surface to the center of the bead.

Distance of trapped beads from the surface was estimated based on the readout from the piezostage. The data were recorded at about 20 μm above the surface.

7.1.4 Viscosity of Alsever's solution

Due to viscosity effect we found small but systematic differences between the power spectra of pure water and Alsever's solution at the same experimental conditions. Knowing (a priori) viscosity of water, it is possible to determine viscosity of purely viscous solvents as soon as viscosity dependent parameter $A = k_B T / 2\pi^2 \gamma$ is extracted from the Lorentzian fitting (see equation (1.8)) and the calibration factor is known [119]:

$$\eta = \frac{k_B T}{12\pi^3 R A \beta^2}. \quad (7.3)$$

Therefore the viscosity of Alsever's solution was estimated by extracting an average A parameter from Lorentzian fitted to 40 PSD (x and y channels) of fluctuations of 3 μm particles. Calibration factor β for viscosity measurements was determined as described above (see paragraph "Calibration and force measurement") in water at the same experimental conditions like for Alsever's solution using beads from the same batch. Again an average from 40 PSD was taken to reduce the particle size distribution effect. Calibration factor β was assumed to be the same in Alsever's solution and in water. Finally the viscosity of Alsever's solution was found to be $(9.3 \pm 0.6) \times 10^{-4} Pa \cdot s$ (25 $^\circ C$).

7.2 Results and discussion

7.2.1 One-particle microrheology

Measurements with RBC were preceded by calibration of the system, which was done using the beads, later attached to RBC. Single and inter-particle response functions were measured simultaneously. The trap stiffness for both the traps were adjusted to be approximately the same. Excluding possible polydispersity of attached beads, our system is quite symmetric (see inset of Fig. 7.1a) so we are expecting to get similar results from the analysis of displacement autocorrelation of both beads separately. We are going to refer these two traps as the left and right trap.

PSD of the bead fluctuation in both traps in the presence and absence of RBC are shown in Fig. 7.1. Spectra recorded in the absence of RBC were satisfactory fitted using the Lorentzian formula (eq. (1.8)), yielding corner frequencies equal to 119 Hz and 127 Hz corresponding to trap stiffnesses 21 $pN/\mu m$ and 22 $pN/\mu m$, for left and right traps, respectively. As the system is quite symmetric and the stiffness of both trap is also comparable, therefore we expect single particle response of left and right trap to be the similar. Hence we have discussed only the results corresponding to left trap for one particle microrheology.

Passive microrheology measurements of single RBC were done at three different states of the cell, namely: RBC at rest (without external force) and the cell stretched by applying external force of 6 pN and 10 pN , corresponding to

stretching ($\Delta L/L \times 100\%$) of about 12% and 16% respectively. Average variance of the trapped bead position (in left trap) was found to be 11.4 nm for unattached bead and 9.6 nm, 9.1 nm and 8.4 nm for cell at rest, stretched by 12% and 16%, respectively. It is clearly visible in Fig. 7.1 that the shape of PSD in the presence of RBC is no longer Lorentzian. The power density gradually increases below the corner frequency which is in contrast to the flat PSD measured without RBC for ($f \ll f_c$). As expected, the power density decreases almost over the whole frequency range with cell stretching. This indicates a nonzero contribution of elastic component which presumably grows with stretching. Measured PSD spectra are expected to exhibit “power law” like behavior at higher frequency range $f \gg f_c$. The power law exponents were determined by fitting a power law ($PSD \sim f^{-\gamma}$) for all presented PSD with γ as an adjustable parameter. Data were fitted in the range from 400 Hz (above the corner frequency) to 5 kHz (half the Nyquist frequency) yielding exponent γ equal 2.0, 1.9, 1.8 and 1.8 for PSD of one particle fluctuations without RBC, cell at rest, stretched by 12% and 16%, respectively. The $1/f^2$ decay obtained for solvent is consistent with free Brownian motions in a purely viscous solution.

Interestingly, at low frequencies (below 10 Hz) PSD approaches higher values in the presence of RBC than for as compared to the free bead. There are at least two possible explanations of this behavior. Low frequency signal indicates the contribution of non-thermal (probably ATP driven) motions previously observed in [118] or is attributed to possible translational motions of the whole RBC-Beads system. The contribution from possible trapping beam pointing fluctuations which usually become relevant at higher forces and low frequencies can be rather excluded because for the unattached bead the spectrum remains flat up to 1.8 Hz. Since RBC is a living cell it might not be completely thermally equilibrated leading to the softening of RBC [118,120]. Despite many debates, non-thermal contribution to the RBC membrane motions still remains controversial. According to [118], fluctuations might be partially non-thermal in the low frequency domain ($f < 10$ Hz). In contrast, no direct evidences for such motions were observed from 1.6 Hz to 32 Hz by Yoon et al [113]. We are aware that in case where non-thermal motions are significant the fluctuation dissipation theorem should be used carefully [12,121]. This is particularly true when the cell is exerting strong forces on the probe in relation to Brownian motions. In contrast, mechanical activity of RBC is much smaller than, for example, actin networks driven by myosin motor proteins [12,121]. In fact, non-equilibrium cellular forces of RBC are definitely too small to be directly observed in bead fluctuations plotted as a function of time like it was seen for osteocyte-like MLO-Y4 cells in ref. [68]. Fluctuations in time of beads attached to RBC (data not shown) are dominated by random Brownian motions and we believe that the fluctuation dissipation theorem remains reliable approximation.

In order to explore second possible explanation of low frequency contribution and also to compare with [113], PSD of the fluctuations of the cell length $PSD_{\delta x}$ at different stretching states were obtained as a Fourier transform of the relative fluctuations between beads (Fig. 7.2). At higher frequencies the behavior of difference spectra is quite similar to single particle PSD, though the fluctuations of RBC length seems to be less affected by stretching. In particular, the power density growth at low frequencies is much smaller and almost negligible. It is therefore more likely that the low frequency contribution observed in single particle PSD is because of translational motions rather than due

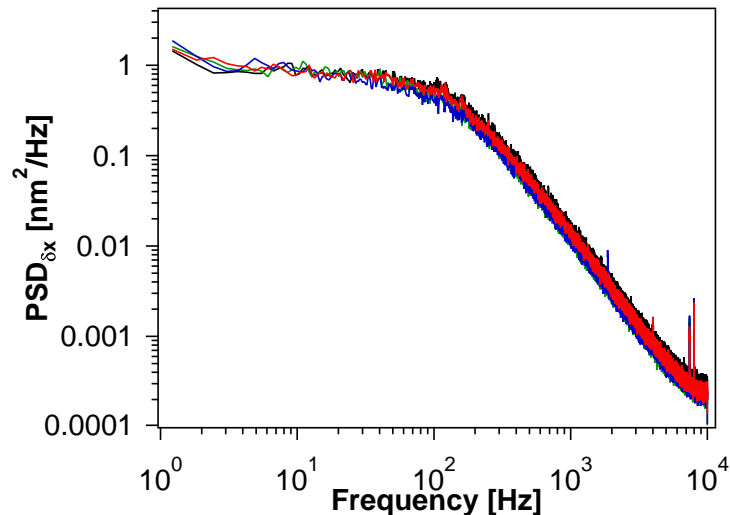


Figure 7.2: Power spectral density of the relative fluctuations between beads in the absence (black), $r = 9.2\mu m$ and presence of RBC and different forces applied to the cell (red - the cell at rest, $r_0 = 9.8\mu m$, green - the cell stretched by 12 %, $r_1 = 10.6\mu m$, blue - the cell stretched by 16% , $r_2 = 10.8\mu m$). In the presence of RBC $PSD_{\delta x}$ represents power spectrum density corresponding to fluctuations of the cell length; r is center to center distance between the beads.

to non-thermal contribution unless the latter occurs without noticeable change of RBC's length. However, this probably is not the case. Since non-thermal noise still can not be completely excluded the combination of active and passive microrheology is required to ultimately distinguish between thermal and non-thermal motions [12]. Nevertheless the optical trapping beams pointing fluctuations usually occur at low frequencies depending on trap stiffness, where non-thermal contribution is expected, so the unambiguous extraction of these extra motions is quite challenging.

Difference data were analyzed in similar way (like single bead PSD) yielding the power exponent equal 2.0 and 1.9 in the absence and presence of cell (for all RBC states), respectively. The obtained values in both cases (PSD and $PSD_{\delta x}$) are only slightly perturbed by RBC presence (and stretching) and are much higher than those reported in [113]. This is probably because the data in [113] is fitted only in the range from 11 Hz to 111 Hz and fulfillment of the condition $f \gg f_c$ is questionable. Thanks to the detection method used in this work, the high frequency limit can be extended significantly.

Figure 7.3 shows the real (a) and imaginary (b) part of the free bead response function in Alsever's solution compared with those obtained with RBC attached, both obtained for left trap. The real part of response function was calculated using the Kramers-Kronig integral (eq. (3.46)). The solid lines represent theoretical predictions without any adjustable parameters calculated by inserting $\alpha = 1/[6\pi r\eta(-i\omega)]$ to equation (3.52a). The relatively good agreement of this control experiment with theory indicates that parameters obtained during

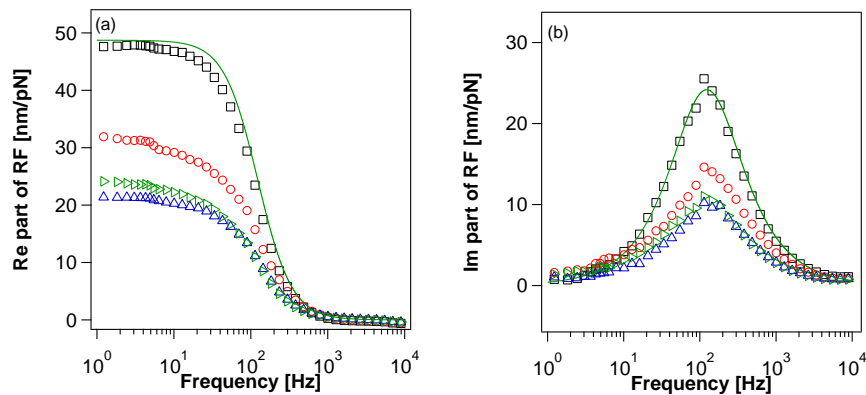


Figure 7.3: Frequency dependence of the real (a) and imaginary (b) parts of an apparent single-particle response function (left trap) in the absence (black squares) and presence of RBC and different forces applied to the cell (red circles) - the cell at rest, green (right) triangles - the cell stretched by 12 %, and blue (up) triangles - the cell stretched by 16 %). The solid green lines are the theoretical predictions based on the measured trap stiffness and calculated without any adjustable parameters.

calibration, in particular stiffnesses, were determined correctly. The difference between theory and experimental data is more pronounced in the real part of the single particle response function probably because of the finite frequency cutoff in the Kramers-Kronig integral. When the cell is attached to the beads, their Brownian motion is partially suppressed leading to the decrease in both real and imaginary part of single particle response function over almost whole measured frequency range. Stretching of the cell leads to the further decrease of the apparent response function. Nevertheless the difference between the cells stretched by 12 % and 16 % appears to be higher at lower frequency region indicating some promotion of slower motions at higher forces.

7.2.2 Two-particles microrheology

Fourier transform of cross correlation displacement (equation (7.1)) of particles coupled solely via hydrodynamic interaction and via RBC is compared in Fig. 7.4. In both cases the motion of the particles become anticorrelated (negative CSD) at low frequency where the confinement by the traps dominate. It is clear however that the presence of RBC significantly increases both the correlation and anticorrelation signals even though the distance between the beads in the absence of cell is little higher. It also dramatically shifts the anticorrelated motion to lower frequencies. The stretching of the cell causes a suppression of anticorrelated motion and/or an additional shift in the same direction consistent with expected increase of the storage moduli. At higher frequencies the propagation of stress is more instantaneous (particularly in the presence of viscoelastic medium like RBC) and one particle tends to move with the other.

The inter-particle response function showed same tendency as was observed in case of CSD (Fig. 7.5). Both the real and imaginary parts significantly

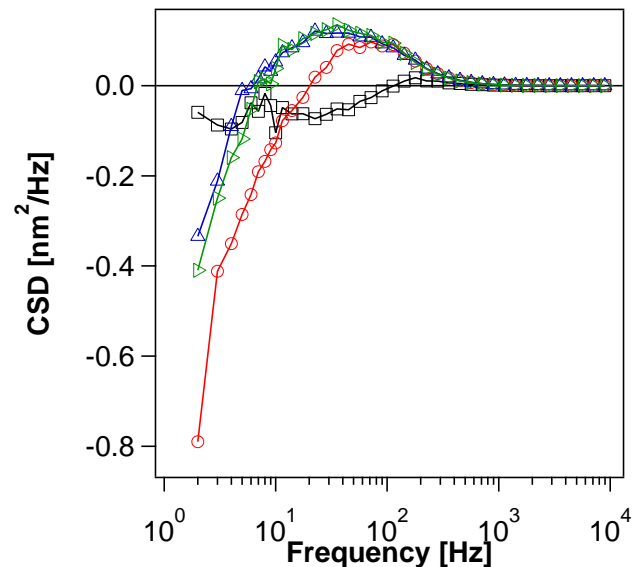


Figure 7.4: Cross spectral density in the absence (black squares, $r = 9.2\mu\text{m}$) and presence of RBC and different strains applied to the cell: red circles - the cell at rest ($r_0 = 9.8\mu\text{m}$), green (right) triangles - the cell stretched by 12 % ($r_1 = 10.6\mu\text{m}$), blue (up) triangles - the cell stretched by 16% ($r_2 = 10.8\mu\text{m}$); r is the center to center distance between the beads. Experimental points are connected by solid lines for better visualization.

increase over wide frequency range when RBC is attached. Anticorrelation observed as negative signal in the imaginary part of response function appears at frequencies roughly one decade smaller than for similar measurements in Alesver's solution. The stretching of the cell leads to an additional increase of low frequency signals ($f < 100$ Hz) and shifts the anticorrelated motion to lower frequencies (Fig. 7.5b).

Investigated system is quite complex so it is difficult to judge whether the presence of RBC just removes anticorrelation or shifts them to lower frequencies. Most probably two effects have place. Also the role of hydrodynamic interactions remains to be elucidated because forces can be transmitted through both the cell itself and surrounding solution. Purely hydrodynamic interaction depends on the distance between two beads and should decrease for longer distances as $1/r$ [122]. In addition the stretching causes significant change in the cell shape leading to the differences in already strongly heterogeneous geometry of the system. This might also influence hydrodynamic interaction and surely increase complexity of the problem, consequently extracting hydrodynamic interaction from these results is not obvious. However in case of pure hydrodynamic interaction the increase in distance between tracked particles (as in the case of stretching) should lead to the decrease of correlation. With RBC we are observing exactly opposite behavior indicating that inter-particle response is dominated by properties of RBC. Taking this into account in the first approximation the hydrodynamic coupling was neglected in calculations. It means that calculated

stiffness will contain an interaction through both the cell and the surrounding medium.

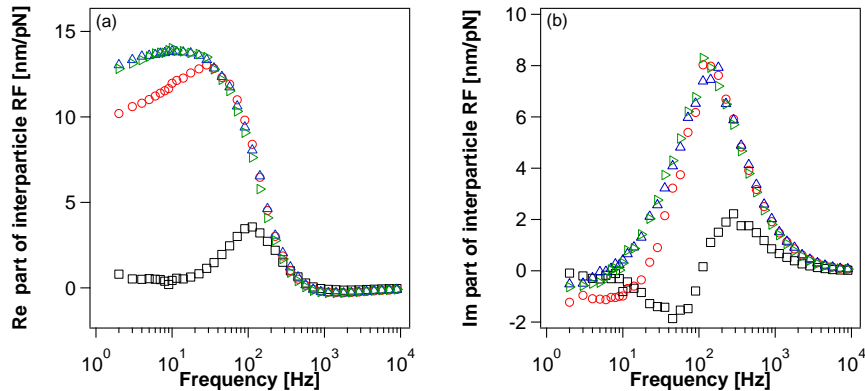


Figure 7.5: Real (a) and Imaginary (b) part of apparent interparticle response function in the absence (black squares, $r = 9.2\mu m$) and presence of RBC and different strains applied to the cell: red circles - the cell at rest ($r_0 = 9.8\mu m$), green (right) triangles - the cell stretched by 12 %, ($r_1 = 10.6\mu m$), blue (up) triangles -the cell stretched by 16% ($r_2 = 10.8\mu m$); r is center to center interparticle distance.

7.2.3 Stiffness of the cell

Single and interparticle response functions from Fig. 7.3 and Fig. 7.5 were corrected for the presence of traps (equations (3.52a) and (3.52c)) giving medium response function from which the stiffness of the system (K) can be obtained by simple inversion. For calculations of corrected (medium) response functions, the trap stiffnesses obtained from corner frequencies of the autocorrelation spectra were used.

The real (elastic) and imaginary (dissipative) parts of the calculated stiffness (K) are presented in Fig. 7.6a and Fig. 7.6b, respectively. Alsever's solution is purely viscous so only imaginary part of stiffness is plotted for comparison. It is clearly visible that the elastic part of the cell stiffness grows with frequency over wide range for all three states of the cell stretches. Stronger frequency dependence is observed for cells at rest. The real part increases when the force is applied so the stress stiffens the cytoskeletal network. Such nonlinear behavior of RBC is well known and was previously reported [101,113,115]. At higher forces further increase of the elastic component is observed but changes are more pronounced at lower frequencies (below 100 Hz). The nonlinear response of the cell indicates that the deformation causes structural changes in the cell/membrane. It was suggested that such hardening can arise from local rearrangement of spectrin network [115]. It is worth to mention that even at strain amplitudes as low as 16 % our experiment is already in a nonlinear regime.

Figure 7.6a also compares elastic component of stiffness measured via single (left trap) and two beads microrheology. Single particle data are accessible at

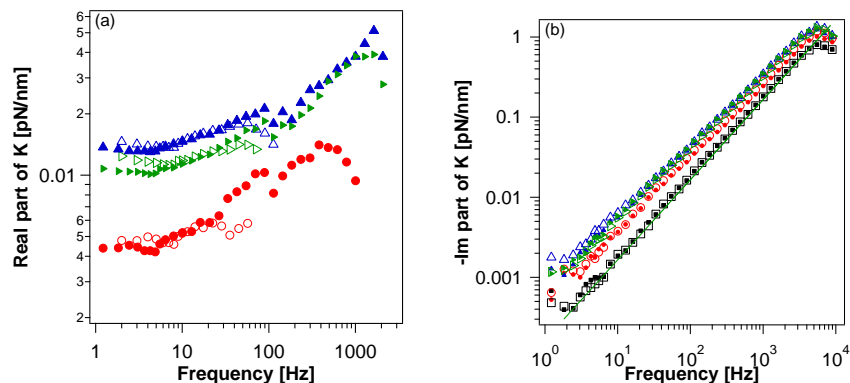


Figure 7.6: (a) Real part of the complex stiffness (K) as a function of frequency measured via single particle (solid markers) and two particles (open markers) rheology. The data are presented in the limited frequency range because of common problem with Kramers-Kronig integral what is particularly noticeable in two beads rheology. (b) Imaginary part of the complex stiffness in the absence and presence of RBC measured with single particle rheology: left trap (solid markers) and right trap (open markers): black squares - without RBC, red circles - the cell at rest, green (right) triangles - the stretched by 12 % and blue (up) triangles -stretched by 16 %. The solid green line is the theoretical prediction based on the measured trap stiffness and calculated without any adjustable parameters. In case of both single and two particles rheology actual complex stiffness was calculated using response functions corrected for the presence of two traps.

higher frequency due to the Kramers-Kronig integral. Surprisingly both methods yield quite similar results though the single probe measurements shows slightly stronger frequency dependence. This striking similarity indicates that local and overall elastic properties of membrane are comparable. It means that the cell transmits the forces to the diametrically opposite side with very high efficiency and local deformation (on average) is negligible at least in the frequency region where data overlap. Such behavior also indicates that stress in the first approximation is evenly distributed along the cell.

The average elastic stiffness obtained in the same way from 12 measured cells at rest is $10 \pm 7 \text{ pN}/\mu\text{m}$ and $9 \pm 6 \text{ pN}/\mu\text{m}$ (both at 10 Hz) for one and two beads rheology, respectively. Both average value and standard deviation measured via two beads rheology is in excellent agreement with previously published data [113].

The apparent similarity of single and two beads rheology is important because single particle rheology is often considered as not ideal [113]. Indeed, in configuration used in this work where stiffnesses of both traps are similar one would expect that the single probe rheology also consists of eventual influence from translational movements. This problem is avoided by using two beads microrheology where the cross-correlated motions are considered. In fact, small difference in these two approaches can be observed at frequencies below 10 Hz where one bead rheology yields slightly lower elastic component in compari-

son to two beads measurements. As previously mentioned, local softening due to non-thermal noise can not be completely excluded in this frequency range. Nevertheless our data shows that influence of translational movements on determined stiffness is not significant and both single and two beads techniques can be applied successfully.

Solvent on its own lacks in elastic component, so the measured real part of stiffness is mainly associated with the cell itself. In contrast, dissipative part (Fig. 7.6b) is expected to reflect viscosity of both Alsever's solution and the cell. Extraction of dissipative component which originates only from the cell is not obvious because of the system's heterogeneity. Simple subtraction of contribution from solvent, as done in [12] for viscoelastic homogeneous system, should rather be avoided here.

Imaginary part of stiffness grows linearly with frequency. Solid line in figure 7.6b is a theoretical prediction for purely viscous solution calculated from the stationary Stokes result as $K = 6\pi R\eta(-i\omega)$ without adjustable parameters [54]. Experimental data obtained in the absence of RBC is consistent with this model, as expected. It is worth mentioning that dissipative parts obtained using the left and right traps are practically identical (see Fig. 7.6b). Small deviation can arise from particle's polydispersity. Dissipative part increases when RBC is attached to the beads and further growth occurs when the cell is stretched. Stretching

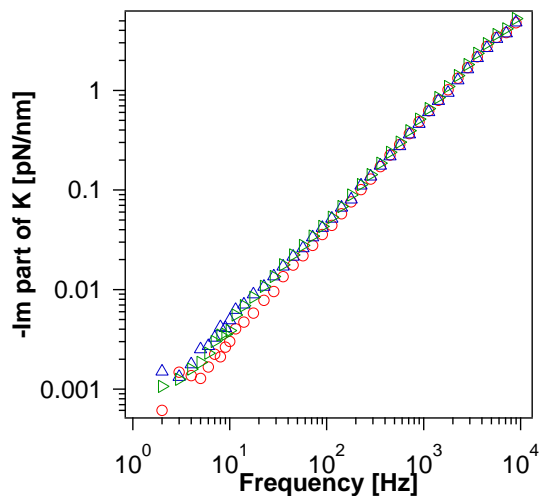


Figure 7.7: Imaginary part of the complex stiffness measured with two particles microrheology for the cell at rest (red circles, $r_0 = 9.8\mu m$) and stretched by 12 % (green (right) triangles, $r_1 = 10.6\mu m$) and 16 % (blue (up) triangles, $r_2 = 10.8\mu m$); r is center to center distance between the beads.

effect dominates at lower frequencies. The difference between dissipation for cell stretched by 12 % and 16 % above 20 Hz is almost negligible. Similar tendency is observed for the imaginary part of K measured via two beads microrheology (see Fig. 7.7). Observed increase in the imaginary part of stiffness suggests the existence of additional, competing dissipative processes when RBC is attached to the beads and when it is stretched.

7.2.4 Raman spectroscopy

In microrheological measurements, we observe changes in the cell elasticity with increasing forces which might cause some structural rearrangement inside the cell. Although we can quantify these changes mechanically, it is hard to suggest which component in the cell undergoes maximum deformation. To gain knowledge on the conformational changes, we make use of Raman spectroscopy. The importance of Raman spectroscopy at single biomolecule level has been previously demonstrated [14, 123].

RBC has lipid bilayer membrane with proteins in it. Underneath it is a cytoskeleton of proteins allowing high elasticity with main protein being spectrin. Ankyrin anchors cytoskeleton to membrane. In general, it is known that membrane proteins determine specific membrane functions, e.g. acting as transporter of specific substances, ion channels, enzyme, receptors, cell identity markers (MHC protein) or linkers which anchor underlying cytoskeleton. Since the latter provide structural stability (via spectrin) and determine shape of the cell it seems to be of particular interest. Hemoglobin has also been shown to have a high affinity interaction and binding with the inner wall of RBC membrane. Number of hemoglobin molecules bound to membrane has been proposed to be of the order of 10^6 per cell [124]. It has also been argued regarding the possibility of hemoglobin to be intercalated within RBC membrane [124, 125]. When RBC goes under stretching then the membrane, cytoskeleton and the molecules bound to them presumably bear most of the force. Thus, it's expected that the stretching should affect the bands mostly related to hemoglobin as well as proteins and lipids in the close proximity of membrane. Preferential excitation close to the edge of RBC should facilitate observation of dominant deformation effects.

Figure 7.8 shows a typical set of Raman spectra obtained from RBC during stretching experiment. The Raman signal was collected for a series of fifteen different stretches of RBC to assess the directionality of changes happening in the spectra. These rich, multiple peaks, vibrational spectra are characteristic of RBC [104, 110, 126].

Raman spectra of RBC are strongly sensitive to excitation wavelength due to possible resonance excitonic coupling between aligned porphyrins [127, 128]. For example resonance Raman of hemoglobin was found to be almost exclusively due to scattering of the haem groups which are strongly absorbing in visible region [129]. In contrast, non-resonant excitation should allow the observation of changes in various constituents of RBC without special promotion (via resonance enhancement) of macrocycle vibrations. That is why 785 nm line (used in this work) yields Raman spectra constituting a mixture of bands from both haem and proteins with relatively strong protein bands [126].

The details regarding proper assignment of particular Raman bands have been a subject of many monographs (see e.g. [126, 130]) and will not be discussed in this study. Instead we will consider only bands which reproducibly change with cell deformation and observed changes are strong enough to make sure they are above noise level typical of this kind of experiment.

It is clearly visible in Fig. 7.8 that the most prominent changes induced by perturbation are observed at around 1035 cm^{-1} . This peak has been variously associated with C-H in-plane bending mode of phenylalanine (Phe) [106, 131] or in plane CH_2 asymmetric mode of vinyl substituent in porphyrin [110, 126]. In

the inset of fig. 7.8 the intensity changes at 1030 cm^{-1} vs relative deformation is presented. Interestingly there are three regions of low, medium and high deformation with completely different behavior. For smaller deformation (of up to 11%), peak around 1035 cm^{-1} is very small and changes are almost negligible. Huge growth in intensity accompanied by band narrowing is observed after RBC is stretched to 16% of its length. More importantly, the peak saturates above 20% of stretch. Such strong force dependence can potentially explain relatively low perturbation of this band in previous, similar experiments where cells were directly trapped by IR beam [104].

The band at 890 cm^{-1} and 960 cm^{-1} which are related to skeletal vibrations are also observed. Intensity changes in these bands are less significant. Although a slight band shift of around 4 cm^{-1} towards small wavenumbers is observed at 890 cm^{-1} . Band at 991 cm^{-1} may correspond to symmetric ring breathing mode of Phe or ν_{45} and undergoes both broadening and a small shift (about 4 cm^{-1}) towards higher wavenumbers. A slight decrease in intensity can also be seen at this position. A strong band at 750 cm^{-1} was measured from the RBCs, which came from the C-N-C breathing stretch vibration in the porphyrin ring. When the RBC was stretched, we observed that this peak shifted up slightly in frequency and its linewidth became narrower. We can see a peak around 1243 cm^{-1} which can be tentatively assigned to Amide III of α -form protein and C-H twist [107]. Phospholipid structural information is contained primarily in the $1062\text{-}1130\text{ cm}^{-1}$ C-C stretching region [107]. Peaks corresponding to C-C and C-N stretch of protein around 1110 cm^{-1} and C-C stretch of trans chain in phospholipid around 1140 cm^{-1} can also be distinguish but no significant changes were observed in these bands as RBC was stretched. CH_2 and CH_3 bending in protein and phospholipid can be observed at 1442 cm^{-1} . In this spectral region we observed increase in the peak intensity and band broadening as we stretched RBC. Another band at about 1535 cm^{-1} maybe assigned to ν_{38} (pyrole breathing) in porphyrin ring of hemoglobin. This band decreases in intensity and a small shift of 3 cm^{-1} occurs when perturbation is applied to the cell. While the peak around 1540 cm^{-1} assigned to either ν_{11} or to Tryptophan (Trp) become more prominent as the force on RBC is increased. Raman measurements were repeated for 15 different RBCs and similar behavior was observed in majority of the cells.

From among all described spectral effects cause by cell deformation the most striking are changes at 1035 cm^{-1} which are most likely associated with Phe in hemoglobin, spectrin and ankyrin, among other proteins. Such huge growth in intensity can be caused by the change of molecular symmetry induced by deformation. The role of hemoglobin in elastic properties of RBC is rather secondary. Nevertheless direct binding to membrane can at least partially influence mechanical response function. On the other hand viscosity of intracellular fluid are supposed to be strongly dependent on concentration and chemical structure of hemoglobin. Elongating the RBC lead to a decrease in the internal volume of cell and corresponding increase in hemoglobin concentration (due to the outflux of water and solutes) [104,132]. This effect can be partially responsible for observed viscosity increase at higher forces in microrheological studies. However only one peak (at 1035 cm^{-1}) exhibit so huge changes, so structural deformation in addition to concentration effect is obvious. At this stage unambiguous location of observed structural changes in RBC is quite difficult because Phenylalanine (Phe) is an essential amino acid that is found in a variety of proteins.

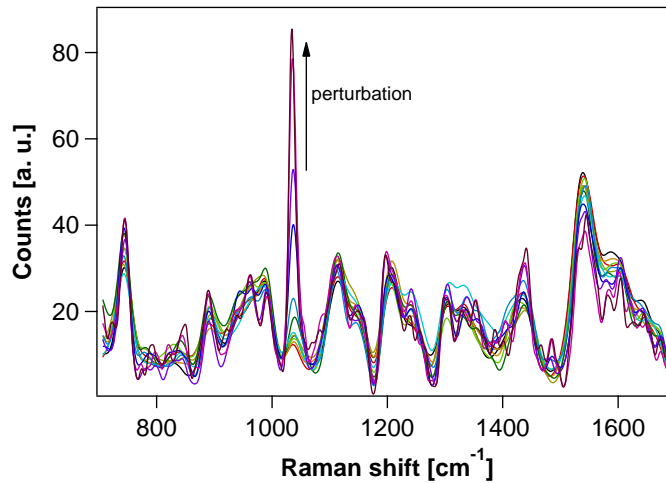


Figure 7.8: Raman spectra of a single RBC at 15 different stretches.

In RBC, it is found in hemoglobin as well as various membrane proteins e.g. ankyrin, band3 proteins and spectrin. Although hemoglobin is considered to be the main source of Raman signal we can not exclude contribution from proteins embedded in membrane and cytoskeleton which presumably undergo maximum deformation. Despite relatively low thickness of the membrane it is (in contrast to internal cell fluids) directly exposed to excitation beam facilitating collection of scattered light. Partial membrane protein contribution to signal might be justified by the presence of strong peak at about 1035 cm^{-1} in Raman spectra of erythrocyte ghosts [106]. In this context ankyrin which anchors cytoskeleton to membrane and spectrin which is responsible for cell's elasticity seems to be of particular interest. It was previously suggested that nonlinear mechanical response of RBC can be explained by possible release of spectrin filament from linker proteins (ankyrin) which then re-bond in a configuration of lower stress [115]. It suggests that linker proteins and spectrin experience particularly strong deformation just before the rupture of the most fragile bonds occur. This model is in agreement with observed intensity changes at 1035 cm^{-1} (see inset fig.7.8). In the region of low deformation (0-11%) the changes are negligible, suggesting that small forces does not affect Phe structure yet. It is most likely that at these forces spectrin rearranges itself without significant changes in its chemical structure, bearing most of the forces. For medium deformation (11-20%), the stress is high enough so that the spectrin network and the linker proteins can undergo structural changes giving steep rise in the intensity. At higher forces ($\geq 20\%$), the Raman signal saturates. This suggests that different processes has to be involved to allow the cell to change shape. We believe that at this point external stress starts to break the weakest bonds between membrane proteins and spectrin (or cytoskeleton) which then re-bond in a configuration of lower stress. We therefore tentatively propose that the changes in band at 1035 cm^{-1} is a powerful probe of interaction between membrane and cytoskeleton during deformation.

In this report we limit our consideration to the peaks whose changes with perturbation can be easily distinguished from noise without using special (statistical) data treatment. Future work will employ sophisticated analysis techniques to reveal more subtle effects.

7.3 Conclusion

In conclusion, these studies show that single and two beads microrheology measurements performed simultaneously for the same human erythrocyte yield similar elastic stiffness suggesting that local and overall elastic properties of RBC are comparable. The small differences between results obtained using these two approaches can be justified by translational motions of RBC-beads system. Also contribution of non-thermal noise can not be excluded but combination of passive and active rheology is required to investigate this matter further. Both, elastic and dissipative components of cell stiffness increase with frequency and also when external stress is applied. Direct linkage between observed mechanical response and chemical structure of the cells was suggested. We found that stretching of the cell affects both haem and proteins bands but changes in proteins structure are significantly stronger. This suggest that proteins in hemoglobin and/or membrane (in particular spectrin and ankyrin) experience the strongest deformation. The growth of imaginary part of stiffness with deformation can be explained by additional dissipative processes associated with the increase of hemoglobin concentration and perturbation of its chemical structure. Finally, we confirmed nonlinear mechanical response of RBC which can be explained by considering some structural reorganization in membrane-cytoskeleton system. Combination of Raman and viscoelastic measurement allowed this model to be proved on molecular level.

8

Mechanochemistry of single red blood cells monitored using Raman tweezers

The primary role of red blood cells (RBCs) is redistribution of oxygen throughout human body. This is possible due to characteristic structure, shape and mechanical properties of the cells. Erythrocytes are built of lipid bilayer which contains many transmembrane proteins and underlying cytoskeleton. It forms flexible biconcave disks which consist mainly of hemoglobin but lacks a cell nucleus and most organelles. Chemical content of RBCs provide a lot of useful information about human health conditions. Therefore blood is one of the most common sample submitted nowadays for medical diagnosis.

As described in previous chapter, in human body, erythrocytes adopt different squeezing/stretching states, hence mechanochemical processes associated with deformation of RBCs have been of particular research interest. Since mechanical properties of RBCs can be affected by malaria, spherocytosis, elliptocytosis or sickle cell anemia [95], mechanochemical studies of RBCs can give us an in-depth understanding of these diseases.

However full understanding of mechanical response of RBC remains illusive. There is therefore strong need to find crucial linkages between structure, mechanical properties and functions of the cell. Understanding of molecular origin of extraordinary mechanical flexibility or nonlinear response of single cell requires more sophisticated experimental approach and extensive theoretical simulations. In this context combination of optical tweezers with single cell spectroscopy seems to be very promising. Linking spectroscopic techniques with optical tweezers opens unique possibility to directly extract biochemical information at single-cell level under controllable mechanical conditions. The possibility of simultaneous use of external force and spectroscopic detection can also provide direct insight into molecular changes caused by mechanical deformations. Here Raman spectroscopy is of particular interest because of its extraordinary chemical resolution and relative simplicity. It yields rich, multi-peaks vibrational spectra containing structural information about RBC's basic

constituents [106–110, 126]. As previously demonstrated, Raman spectroscopy combined with optical tweezers is extremely valuable tool for reliable estimation of cell's vitality [133–137]. Sensitivity of this method is high enough for identification and monitoring of changes in intra-cellular components induced by cell stretching. In particular, direct evidences for deoxygenation of cells with stretching was shown [104].

Most of Raman studies on RBC till now were performed with cells being directly trapped with focused optical beam. This is not an ideal approach because of potential light induced damage within the trapping volume. Reducing the power of trapping beam, as often recommended, leads to significant diminution of Raman signal-to-noise ratio and needs for extensive averaging at the expense of single experiment acquisition time. In this case, external forces applied to cells using optical tweezers are also strongly reduced. This problem can be avoided by attaching RBC to chemically functionalized microparticles which might hold the cell during Raman experiment [115]. Although heating via beads (size dependent process) or influence of scattered light still can not be completely excluded, the risk of direct light-induced damage by trapping beam is significantly reduced. It is therefore possible to perform very sensitive experiments, at higher forces and lower noise, for longer time periods.

This chapter shows the results of Raman spectroscopy of a single red blood cell which is gradually stretched using optically trapped beads attached to the cell. Using this approach we extended our previous Raman measurements [104] to many different RBC's stretching states which require longer time for experiment and more sophisticated analysis method. The applied force is intended to simulate step-by-step deformation experienced by cells in normal conditions (induced by blood flow) as they squeeze through microvasculature. To further improve the sensitivity of the experiments and facilitate their interpretation, 2D correlation and principal component analysis (PCA) techniques were applied. The purpose of this work is to help unravel direct relationship between mechanical deformation of RBC and chemical changes occurring in the cell structure on molecular level.

8.1 Materials and methods

The experimental setup is described in details in section 4.1.1 of chapter 4. The Raman excitation beam used in this case was 785 nm.

Raman spectra were recorded with a spectral resolution of 3 cm^{-1} for 30 seconds at each acquisition. Measured Raman spectra were background subtracted, normalized using Multiplicative Scatter Correction (MSC), smoothed using smoothing spline technique [114] and median centered before performing 2D correlation and PCA. Analysis was done in Matlab platform.

The RBC sample and beads were prepared as described in section 4.3.2 of chapter 4. Polystyrene beads were attached to a single RBC as follows: two beads were trapped in the optical traps while RBC was held by the optical trap generated by the Raman excitation beam. The two trapped beads were carefully approached towards the diametrically opposite ends of RBC and the connection of RBC with the beads was obtained in around 5-10 seconds. The position of beads were then adjusted with the help of movable mirrors to make sure that the excitation beam is hitting the edge of RBC. Cells were stretched

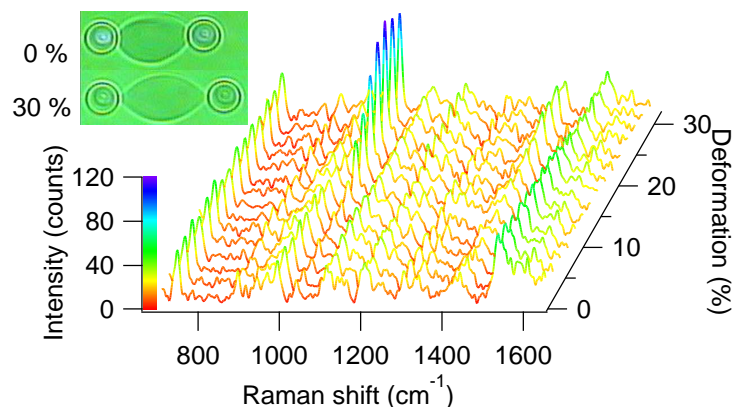


Figure 8.1: 3D representation of Raman spectra of single RBC at 15 different stretches. Inset shows microscope image of RBC, with the polystyrene beads attached, at rest and stretched by 30 %.

by moving one of the trap. Measurements of Raman spectra were done on 15 different cells and most of them were found to behave in a similar fashion.

In order to get insight into spectral changes induced by cell deformation, in particular those which are difficult to observe from direct visual inspection, we used multivariate analysis [67] and 2D correlation [66]. Section 4.4.1 describes the idea behind these two techniques.

Figure 8.1 shows a typical set of Raman spectra of single RBC collected in our experiments. Raman signal at fifteen different stretches was measured to check whether the changes happening in the structure are gradual or random in nature. Raman spectra of RBC depend strongly on excitation wavelength [127,128]. One of the advantage of 785 nm excitation (used in this work) is that bands associated with proteins can be observed in addition to those associated with the porphyrin macrocycle [110]. Presented Raman spectra are characteristic of single RBC and for unstretched cell has been discussed in details in [110,126,127].

8.2 Results

Deformation was conventionally measured using image analysis by calculating the distance between the beads which were attached to the diametrically opposite ends of the cell. It was calculated in the following way: $Deformation(\%) = (\Delta L/L_0) \times 100$ where, $\Delta L = L - L_0$ is the difference between stretched (L) and relaxed (L_0) diameter of the cell.

It is clearly visible in Fig. 8.1, even without statistical processing, that the stretching of the cell affects some Raman bands (see also color gradient of the plot), in particular the bands centered at about 991 cm^{-1} , 1035 cm^{-1} and 1442 cm^{-1} . 1035 cm^{-1} peak is associated with in-plane CH_2 asymmetric mode of vinyl substituent in porphyrin [110,126] and/or Phenylalanine (Phe) [106,131]. The bands at 991 cm^{-1} and 1442 cm^{-1} are assigned to ν_{45} /Phe and CH_2/CH_3 in plane modes of haem, respectively [126]. As seen in Fig. 8.1,

at low deformation the growth of the peaks at 1035 cm^{-1} and 1442 cm^{-1} is negligible. They start to grow when the stretching is more than 10% and the growth is saturated at higher cell deformations (above 20 %).

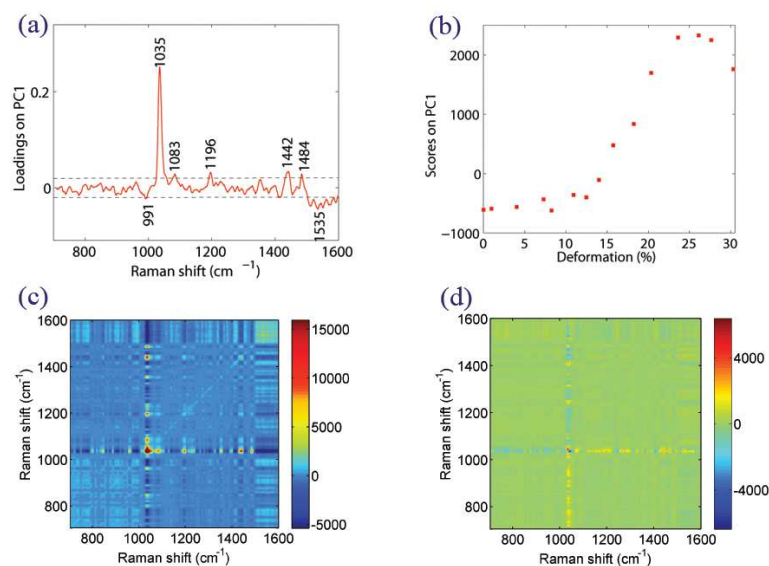


Figure 8.2: PCA and 2D correlation analysis of measured Raman spectra. **Top:** (a) Loading plot with threshold (dashed lines) estimated from experimental noise analysis. The inset demonstrates data used to define the threshold. (b) Scores plot showing overall intensity of all bands above the threshold with increasing cell deformation. **Bottom:** 2D correlation analysis for whole measured spectral window (synchronous map (c) and asynchronous map (d)). Cross correlation peaks can be seen in synchronous map indicating bands correlated during stretching.

The most remarkable finding of our measurements - the extremely high sensitivity of 1035 cm^{-1} peak to the cell extension - has not been reported yet. It permits us to suggest the monitoring of this peak intensity as a marker to characterize internal deformations in the cell in possible lab-on-a-chip applications. Other Raman bands also change with stretching, but their behavior was revealed only using statistical techniques (see below).

8.3 Discussions

To obtain the dynamics of conformational changes we first performed the PCA analysis using data in the whole spectral range (Fig. 8.2a). As can be seen from the score plot, during small deformations of the cell (up to 10%), spectral changes are negligible (see also Fig. 8.1). Hence the maximum intensity variation of spectra obtained at five initial values of deformation may be used to estimate a threshold to discard the peaks generated by the electronic and mechanical noise and errors by numerical calculations. Then we can consider only those Raman bands which are above this threshold.

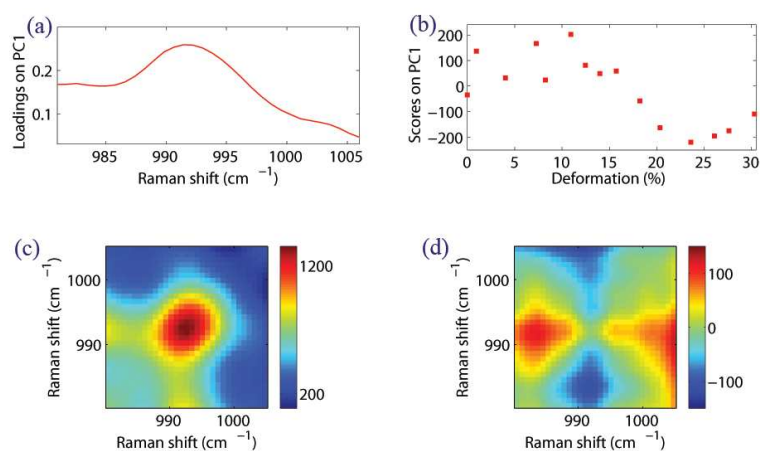


Figure 8.3: Statistical analysis for Raman band at 991 cm^{-1} . **Top:** PCA analysis (loading plot (a) and scores plot (b)). **Bottom:** Expanded view of 2D correlation maps from Fig. 8.2 (synchronous map (c) and asynchronous map (d)).

Hence to establish the threshold in the loadings plot we performed PCA analysis of the Raman spectra obtained for the first five values of deformations. Multiplying each data point on the scores plot gives us the intensity of the corresponding spectra with respect to the median spectrum. The maximum intensity was found to be around 40 units (inset of Fig. 8.2a). To translate this threshold (in intensity) to the loadings plot of complete set of spectra we divided it by the highest value in the scores plot of Fig. 8.2b. The threshold (± 0.02 in loadings) was then used for further analysis.

We conclude that the loadings of the first principal component, which captures almost 80% of the total variance, is dominated by bands centered at 1083, 1196, 1484 and 1535 cm^{-1} along with above mentioned bands at 991, 1035 and 1442 cm^{-1} . The former four bands can be assigned to $\delta(=C_bH_2)_{asym}$, $\nu_5 + \nu_{18}$, ν_3 and ν_{38} modes respectively [110, 126, 130].

These selected peaks are also consistent with the most prominent features observed in the complementary technique, 2D correlation analysis, where strong correlation between these bands is observed (Fig. 8.2c and Fig. 8.2d). Positions of cross-correlation peaks in synchronous map is consistent with the PCA analysis. This confirms that this set of Raman bands is changing synchronously with the cell stretching.

In order to characterize the intensity behavior of correlated bands with deformation, we performed the PCA analysis with the spectral windows reduced to include the selected bands only. Resulting scores plots are intended to mimic the band intensity behavior of single band with stretching. In a way, PCA acts as a fitting that permit us to monitor the selected Raman bands even when the spectra are noisy and without easily distinguishable features. Results for bands at 991, 1035, 1083 and 1196 cm^{-1} are shown separately in Fig. 8.3b, 8.4b, 8.5b and 8.6b, respectively, where we can see that all the bands exhibit similar tendency with the cell stretching. If the cell is deformed less than 10%,

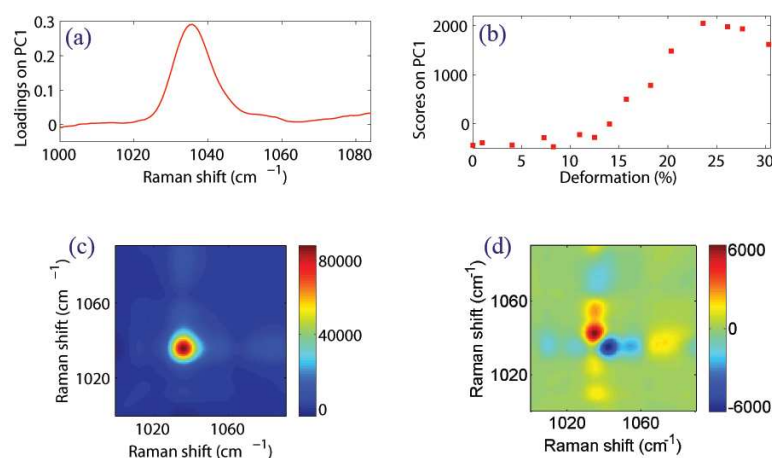


Figure 8.4: Statistical analysis of Raman band at 1035 cm^{-1} . **Top:** PCA analysis (loading plot (a) and scores plot (b)). **Bottom:** Expanded view of 2D correlation maps from Fig. 8.2 (synchronous map (c) and asynchronous map (d)).

these bands exhibit almost constant Raman intensity. Higher mechanical forces lead to almost linear increase (or decrease) dependence with stretching. This behavior is observed up to about 20% of cell deformation. Finally, the bands saturated for deformations exceeding 20%.

However, the bands at 991 and 1535 cm^{-1} showed inverse behavior with increased deformation i.e their intensity decreased in the deformation range of 10-20% and saturated above 20% (see, for example, data shown for 991 cm^{-1} band in Fig. 8.3).

To study the dynamics of band's position and their shapes we took advantage of 2D correlation method. We performed the 2D correlation analysis with the deformation as the external parameter. Figures 8.3, 8.4, 8.5 and 8.6 show 2D maps for the individual bands. Similar trends for some group of peaks are clearly visible. In particular, bands 1196 cm^{-1} and 1442 cm^{-1} (data not shown) show similar patterns in synchronous and asynchronous maps. In the asynchronous map we observe a characteristic pattern for band broadenings formed by four lobes in a cross-like shape. It can also be seen that this pattern is a bit asymmetric. This is caused by the small shift of the Raman band maxima to higher wavenumbers. At 1035 cm^{-1} we observe a similar pattern but with opposite signs in asynchronous maps indicating that this band is narrowing and shifting to smaller wavenumbers with stretching. Bands at 991 and 1535 cm^{-1} also have the same cross-like shape but they are decreasing in intensity (see example data shown for 991 cm^{-1} band, Fig. 8.3). Simulation of their behavior suggest that 991 cm^{-1} band is broadening and shifting to lower wavenumbers and 1535 cm^{-1} band (data not shown) is broadening and shifting to higher wavenumbers. A different pattern was observed for 1085 cm^{-1} band which exhibits two lobes at both parts of the diagonal in asynchronous map (Fig. 8.5). This indicates that the width of the band remains the same but a shift to lower wavenumbers occurs. All observed peak frequency shifts are rather small and do not exceed

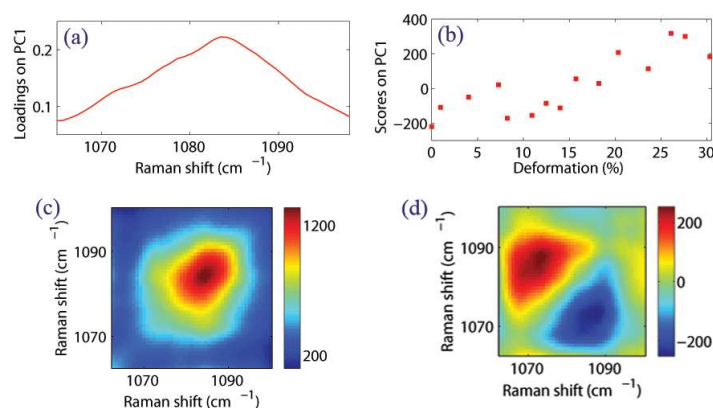


Figure 8.5: Statistical analysis for Raman band at 1083 cm^{-1} . **Top:** PCA analysis (loading plot (a) and scores plot (b)). **Bottom:** Expanded view of 2D correlation maps from Fig. 8.2 (synchronous map (c) and asynchronous map (d)).

5 cm^{-1} , close to the spectrometer resolution.

The main constituents of RBC are: hemoglobin and cytoskeleton (including spectrin), all surrounded by thin membrane with many embedded proteins. That is why vibrational spectra consist mainly of bands characteristic of porphyrin macrocycle and various proteins. The shape of cells is preserved by spectrin network and ankyrin proteins which anchors cytoskeleton to membrane. It has also been shown that about 10^6 hemoglobins per cell are strongly bound to the inner wall of RBC membrane with possible intercalation [124,125]. Stretching of the cell is expected to affect mostly membrane and cytoskeleton, which absorb most of the forces, and also hemoglobins, in particular those which are bounded. Raman excitation close to the edge of RBC allowed us to get signals from the above mentioned cell's regions which undergoes maximum deformation.

The statistical analysis, in particular scores plots, clearly shows that the behavior of most of the bands is quite similar: their intensity remains almost unaffected at low cell deformations and rapid changes occur at intermediate forces which is followed by band saturation at highest deformation achieved in the experiments. Most of these bands can be associated with different vibrational modes in hemoglobin. It indicates that RBC's chemical structure is strongly perturbed by deformation. Such activation/deactivation of selected Raman transitions can be caused by significant changes in molecular symmetry induced by deformation. Although the role of hemoglobin in maintaining the shape of the cell is rather secondary we believe that via direct binding to membrane it acts as an important probe of membrane/cytoskeleton interaction.

Raman measurements were performed using 785 nm excitation beam which is slightly absorbed by hemoglobin. Hence resonant enhancement of some Raman bands has to be considered as another possible mechanism. To the best of our knowledge, absorption measurements of single red blood cell at different stretching states has not been performed yet. Nevertheless electronic structure of hemoglobin is expected to change with cell deformation, at least via

deoxygenation [104, 138]. This should lead to the changes in RBC's absorption spectrum, in particular, the absorption grows at 785 nm [138]. In general Raman spectra excited at 785 nm show strong enhancement of the B_{1g} modes and the vinyl modes [110]. Therefore expected increase of absorption (at 785 nm) with stretching should further enhance all above mentioned modes almost proportionally. However our data clearly shows that intensities of some modes (in particular 1035 cm^{-1}) grow much stronger with stretching than the others so this hypothesis appears to break down. Another effect which is expected to affect proportionally all measured Raman intensities is connected with hemoglobin concentration in the cell. Elongating the RBC decreases the internal volume of cell and leads to the corresponding increase in hemoglobin concentration [104]. This effect should not only promote Raman intensities at all wavenumber but also neighbor-neighbor interaction between hemoglobins. Such enhanced interaction can be partially responsible for observed broadening of the peaks at 1196 and 1442 cm^{-1} . Nevertheless hemoglobin concentration effect alone can not fully explain observed behavior of Raman bands and we have to consider significant structural changes caused by mechanical deformation. Exact nature of structural changes in RBC are not straight forward to determine mainly because Phenylalanine (Phe), which is an essential amino acid that can be found not only in hemoglobin but also in various membrane proteins e.g. ankyrin, band3 proteins and spectrin [139]. Although hemoglobin is most likely the main source of Raman signal perturbation, we can not completely exclude contributions from proteins embedded in membrane and cytoskeleton which bears most of the forces during deformation. Direct exposure of membrane to Raman excitation beam is supposed to enhance total scattering probability from it. Interestingly, in Raman studies of RBC ghost [106], strong peak at about 1035 cm^{-1} was also observed which might suggest partial membrane contribution in our data. From many membrane proteins it is ankyrin which anchors cytoskeleton to membrane and that is why this protein together with spectrin presumably undergoes maximum deformation.

Taking into account all the above mentioned aspects, the behavior of Raman bands intensities as a function of applied deformation can be tentatively explained as follows: we suppose that at low deformation, where bands intensities remain almost constant (within experimental error), spectrin bears most of the forces and rearranges itself without significant changes in its primary chemical structure. It is likely that in this range of deformation, structural changes might occur in its higher order structure. At intermediate deformation range (10-20%), the stress is high enough and can lead to significant structural perturbation of linker proteins, spectrin network as well as hemoglobin attached to membrane leading to significant changes in Raman bands intensities. In order to explain observed behavior of Raman transitions at higher deformation (where bands intensity growth saturates), we need to consider the origin of mechanical nonlinearity of red blood cells. It was proposed that nonlinear response of cell can originate from the possible release of spectrin filament from linker proteins (ankyrin) which then re-bond in a configuration of lower stress [113, 115]. We believe that observed saturation of the peaks correspond to filament release from the linkers. This process is followed by creation of new bonds but in a configuration of similar or even lower stress. Behavior of all the bands discussed here are consistent in a way that they remain constant up to 10% cell deformation, increase (or decrease) in intermediate deformation range, then saturates for a

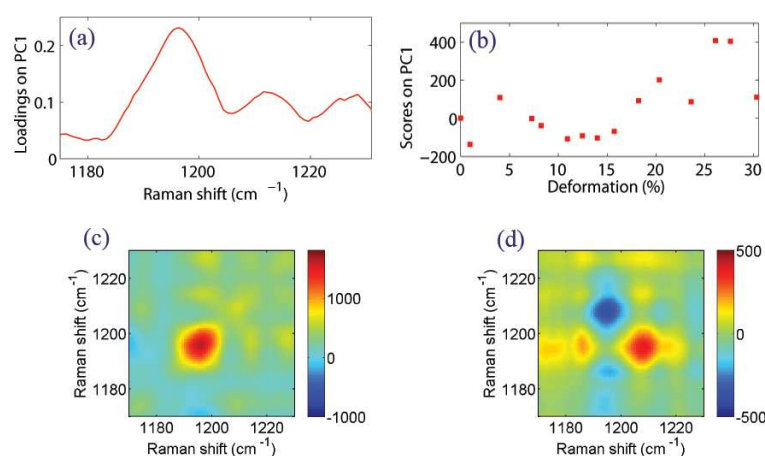


Figure 8.6: Statistical analysis for Raman band at 1196 cm^{-1} . **Top:** PCA analysis (loading plot (a) and scores plot (b)). **Bottom:** Expanded view of 2D correlation maps from Fig. 8.2 (synchronous map (c) and asynchronous map (d)).

small region and finally decrease (or increase) slightly at higher deformation (above $\sim 25\%$).

8.4 Conclusion

We have presented Raman spectra of RBC in relaxed and at various stretching states and discussed the spectral changes induced in RBC by mechanical deformation. Statistical techniques, such as principal component analysis (PCA) and 2D correlation spectroscopy were applied to facilitate detailed analysis of spectral changes. Mechanical deformation of cell mainly affects the bands corresponding to hemoglobin but contribution from spectrin and membrane proteins can not be excluded. While Raman intensity changes with deformation were provided by both - 2D contour maps as well as PCA, other spectral details such as band broadening and shifting were extracted from the 2D correlation analysis. We found that most of the affected bands show similar intensity behavior with stretching. The saturation of bands at higher deformations suggests some structural relaxation that RBC has to undergo to bear extra load. The results confirm widely accepted belief that spectrin release from membrane proteins allows for significant shape changes of red blood cells. We therefore tentatively suggest that interaction between membrane and cytoskeleton during deformation can be efficiently probed by confocal Raman spectroscopy, in particular via the peak around 1035 cm^{-1} .

9

Frequency dependent cross-correlated studies of single DNA mechanics using optical tweezers

Deoxyribonucleic acid (DNA) is a vastly studied biopolymer. DNA studies are not only interesting in prospect for understanding important biological processes such as DNA-protein interactions but it is also a perfect system to model semiflexible polymers under hydrodynamic interactions.

DNA exists in many forms, out of which double-stranded, B-form DNA is the most common and is found in most of the living beings. The double helix provides bending and twisting rigidity and the phosphate group provides the negative charge to the molecule. At the monomer scale, DNA acts as a very stiff material, thus it is called as semiflexible polymer. DNA, like many other polymers, adopts a random coil conformation in a solution to increase its entropy. The entropic force plays an important role in most of the cellular functions, thus its experimental characterization is being explored widely [86]. At physiological conditions, the entropic force exists up to 10pN [16] and is well described by worm like chain (WLC) model. Pulling DNA decreases its entropy at the expense of energy. Elasticity of DNA in this region is thus purely entropic in nature. Between 10 and 65 pN, the force on DNA increases rapidly with stretching as DNA resists further extension. This region falls under “enthalpic elasticity”. Finally at around 65 pN, the molecule enters overstretching regime as its length is increased 1.7 times without much change in the force.

The dynamics of partially extended DNA has been studied previously [2, 4, 140], but its detailed understanding is still a subject of interest. It’s widely believed that DNA goes from a “non-free draining state” to a “free draining” state as it is stretched [140]. The physics of these effects depend mainly on hydrodynamic interactions and entropic force. DNA is double helical due to hydrophobic interactions. Helical structure minimizes the accessible space between consecutive base pairs, and therefore avoid the contact of the bases with

water molecule. Internal hydrodynamic interaction increases the polymer friction coefficient as the DNA is stretched, causing a decrease in DNA relaxation time [140]. As the polymer is stretched, distinct relaxation times and spring constants are introduced due to symmetry breaking for the longitudinal and transverse directions. Nonlinear spring constant and anisotropic friction coefficient plays an important role in polymer dynamics [2]. Recently we showed the contribution of colored noises in DNA, when it is extended [141].

Single molecule force spectroscopy has brought new insights into various DNA biological functions and relationship between hydrodynamic and entropic interactions in light of an extended polymer [2–4, 86, 142]. It still remain unclear regarding DNA's response in medium in which it is embedded in low force regime where entropy is prominent. The DNA molecule undergoes critical biological functions such as transcription, replication and other molecular motor-driven processes. During these processes, it is believed that the DNA strand undergoes numerous mechanical folding and relaxation events that calls for better understanding of how DNA responds to forces.

Here we present an experimental approach that simultaneously measures DNA's viscoelastic response, its cross-correlation spectrum and its complex stiffness. The approach we use is an optical-trap based two particle passive microrheology (PMR) [12, 54] which can be done by tracking thermal fluctuations of both trapped beads simultaneously. Brownian motion of the trapped bead limits the time resolution of the measurement of single bead and can be used only for picoNewton force resolution. Also, single bead rheology just gives the local response function of the system. Benefit of using two beads PMR is that we can probe the whole system. The cross-correlated measurement reduces the noise factor from thermal fluctuation of individual beads. Brownian motion is a stochastic process with no memory. Hence the fluctuation of the two trapped beads are independent of each other. Hence, any correlation that exists between the two beads is due to the molecule with which they are attached. Thus, the cross correlation between the two beads can give high temporal and force resolution of the molecule [2].

We studied the behavior of eight DNA molecule from relaxed state to various incremental force (stretch) and computed the inter-particle complex response function, complex stiffness and cross-spectral density (CSD) at each force/stretch.

9.1 Materials and methods

The studied molecule was a double stranded λ -DNA of 24 Kbp which was obtained by digesting 48 Kbp *E. Coli* DNA (New England Biolabs). The digested DNA was synthesized at both ends with biotin-digoxigenin to connect with streptavidin ($1.87\mu\text{m}$) and anti-digoxigenin ($3.15\mu\text{m}$) coated polystyrene beads (Spherptech) respectively as elaborated in Appendix A.2.

The microrheology set-up and the process for making DNA-bead construct has been described in details in chapter 4.

9.1.1 Data analysis method

Detailed theoretical description of two probe microrheology has been described in chapter 3 and the methodology implemented here is very similar to as proposed in chapter 7. Fluctuations of two particles (without and with DNA in between) were recorded simultaneously with sampling frequency of 20 kHz for 2 minutes. From this data, the DC component was removed and noise-reduced power spectral density (PSD) was computed by averaging together the power spectra of short segments of the filtered data [117]. In order to further reduce noise, randomly distributed points in log scale were obtained and above mentioned calculations for both PSD and CSD spectra were log-binned [118] before response functions were obtained. Data were processed using Igor 6.2 program (Wavemetrics).

In order to monitor the actual length of DNA and to make appropriate correction for a trap, the distance between trapped particles must be known. The distance between two particles were calculated using image analysis and the *a priori* knowledge of beads diameter.

Trap stiffness measurement and calibration of both traps were achieved using the method described in section 1.2 of chapter 1. Calibration factor used for DNA measurements was corrected for changes in position detector sum signal by multiplying it with the ratio of corresponding sum values. Knowing stiffness of the traps, the force can be easily determined by multiplying it by particle displacement. In this work force was calculated based on displacement of bead in fixed (right) trap.

Hydrodynamic drag γ strongly depends on the distance of particle from the surface. Although all measurements were done well above the surface, data was corrected for drag effect using Eq. (7.2). The data were recorded at distance (h) of about 20 μm from the surface.

In order to monitor the actual length of DNA and to make appropriate correction for a trap, the distance between trapped beads must be known. It was calculated using image analysis and *a priori* knowledge of beads diameter. Stretched length was conventionally calculated as: $Stretching(\%) = \frac{L}{L_0} \times 100$, where L_0 and L are the DNA contour length and the length to which DNA is pulled, respectively.

9.2 Results and discussion

Measurements with DNA were preceded by calibration of the system, which was done using exactly the same beads, later attached to DNA.

Power spectral density of bead fluctuations (3.15 μm , right trap) in the absence of DNA is shown in figure 9.1. Spectra were satisfactory fitted using simple Lorentzian formula (equation (1.8)) yielding corner frequencies equal to 296 Hz and 176 Hz corresponding to trap stiffnesses 32.74 pN/ μm and 32.73 pN/ μm , for left (1.87 μm bead) and right (3.15 μm bead) traps, respectively.

Passive microrheology measurements of single DNA molecule were done at seven different stretchings, namely: DNA at rest (without external force, stretched to 72.7%), and the DNA stretched to 85.8% (1.86 pN), 90.9% (6.44 pN), 91.86% (8.72 pN), 93.5% (13.01 pN) and 94.3% (16 pN) respectively. We have discussed earlier in details the changes in PSD of single DNA when it is

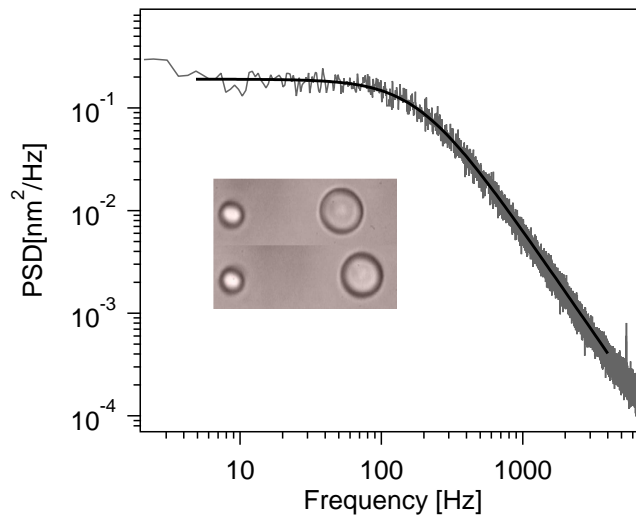


Figure 9.1: Power spectrum density obtained in the absence of DNA (gray curve) is fitted with Lorentzian function (black line) and used for calibration purposes as described in the text. Inset shows the images of constructed system taken by the microscope camera.

stretched [141]. The main aim of this work was to correlate the changes in PSD with the noise of the system. We observed similar trends in our PSD measurements - an overall decrease in the power of the signal and deviation of the shape from Lorentzian, as DNA is stretched. This indicates nonzero contribution of elastic component which grows with strain. Current work concentrates in studying the frequency dependent dynamical properties of DNA's rheological properties using a cross-correlated measurement.

Figure 9.2 shows the cross-correlation of the position fluctuation of two beads in the absence and presence of DNA and at different stretches. The beads solely coupled via hydrodynamic interactions have a characteristic time delayed dip suggesting anticorrelated motion [143]. When no force is applied on the DNA molecule, the cross-correlated fluctuations still show the anticorrelated motion, suggesting hydrodynamic interaction dominates at low stretches. At higher forces, the beads move together in a highly correlated fashion, indicating stiffness of DNA. At a force of 16 pN, the cross-correlated fluctuation displays exponential decay in motion. The stretching of the DNA causes suppression of anticorrelated motion with expected increase of storage moduli. Hydrodynamic coupling of the trapped beads contributes an additional fast-decaying term to the correlation function [143]. Multiplying the cross-correlated motion with respective trap stiffness can give us the measure of force fluctuation across the DNA as calculated by [2].

Fourier transform of cross-correlation displacement of particles will give us cross-spectral density (CSD) which can be used to calculate the inter-particle response function and complex stiffness of the DNA.

Fig. 9.3 shows the real and imaginary part of measured response function

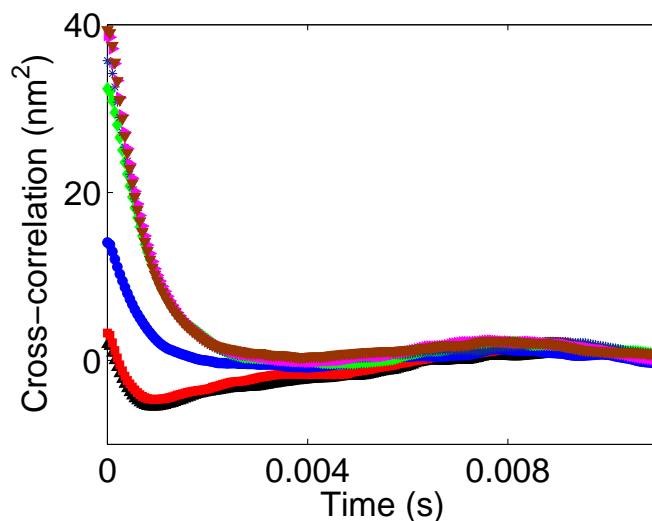


Figure 9.2: Cross-correlated fluctuation in the absence (black up triangle, $r = 6.25\mu m$) and presence of DNA at different stretches: red square - the DNA at rest (72.7%), light blue circle - the DNA stretched to 85.8%, light green diamond - the DNA stretched by 90.9%, dark blue cross - the DNA stretched by 91.86%, pink right triangle - the DNA stretched to 93.5%, brown bottom triangle - the DNA stretched to 94.3%.

(RF). Both real and imaginary parts significantly increase over wide frequency range when DNA is stretched. For beads without DNA in between and for the relaxed state of DNA, frequency dependent anticorrelation in imaginary part of RF is due the domination of trap at lower frequency. At high frequencies, the viscous drag is dominant so that the RF is independent of trap power. Once the DNA is stretched, the stiffness of DNA is the most important governing factor, as was evident from cross-correlated fluctuation as well.

Role of hydrodynamic interaction in this system cannot be ignored. Although it has been suggested that the presence of DNA shields hydrodynamic interaction by 60% [2], suggesting the dominance of DNA in dictating the mechanics of beads in optical traps. Pure hydrodynamic interaction depends on the distance between two beads and should decrease for longer distances as $1/r$ [122] (higher stretching state). With DNA we observe exactly opposite behavior indicating that interparticle response is dominated by properties of DNA. Taking this fact into account hydrodynamic coupling was neglected in calculations. It means that calculated stiffness will contain interaction through both, DNA and surrounding solution.

9.2.1 Stiffness of the DNA

Interparticle response functions from Fig. 9.3 was corrected for the presence of traps, giving medium response function from which stiffness of the system (K) can be obtained by simple inversion. For calculations of trap-corrected

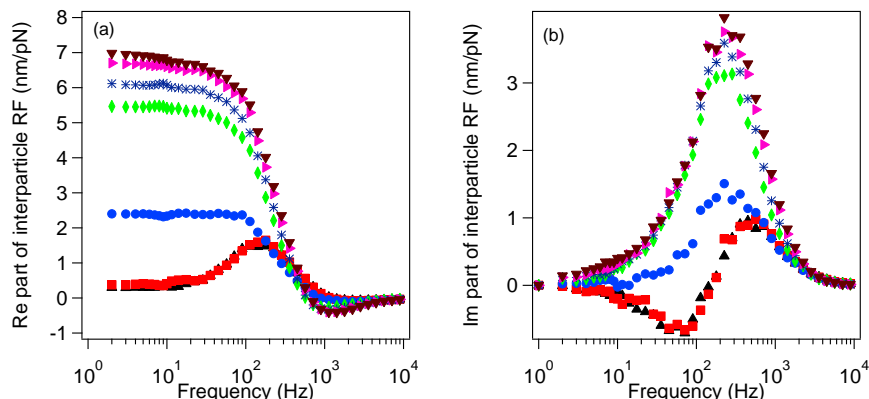


Figure 9.3: Real (a) and Imaginary (b) part of apparent interparticle response function in the absence (black up triangle) and presence of DNA at different stretches: red square - the DNA at rest (72.7%), light blue circle - the DNA stretched to 85.8%, light green diamond - the DNA stretched by 90.9%, dark blue cross - the DNA stretched by 91.86%, pink right triangle - the DNA stretched to 93.5%, brown bottom triangle - the DNA stretched to 94.3%

(medium) response function, the trap stiffnesses obtained from the corner frequencies of the autocorrelation spectra measured for exactly the same particles were used.

DNA elasticity depends on various parameters, such as base pair stability as a function of ionic strength, interphosphate stretching, electrostatic interaction and so on. Fortunately to describe the flexibility of DNA its local properties are not needed, but through coarse graining considerations approximations about the global properties can be made as long as we concentrate on DNA much larger than its persistence length (l_p) [144]. For a very small force $\sim k_B T/l_p$, the DNA force extension relation is linear, but for higher forces the effect becomes nonlinear in nature [87, 145]. The forces applied to DNA in our case is $\gg k_B T/l_p$, hence we should expect nonlinear behavior in the DNA stiffness. This effect has also been noted in previous studies [2, 87, 140].

The real (elastic) and imaginary (dissipative) parts of the calculated stiffness (K) are presented in Fig. 9.4a and Fig. 9.4b, respectively. PBS is purely viscous so only imaginary part of stiffness is plotted for beads without DNA in between. It is clearly visible that the real part of stiffness increases with the force indicative of nonlinear behavior of DNA as predicted by [2]. The increase in stiffness becomes more pronounced as the force goes to higher limits. Its interesting to see that at lower forces (in entropic regime), the stiffness is almost constant over complete frequency range at a given stretch. But above entropic force frequency dependent behavior of stiffness is visible. The stiffness remains constant at low frequency (~ 10 Hz) and then increases slowly with frequency. The slope becomes steeper as we approach higher forces. Solvent on its own lacks in elastic component, so the measured real part of stiffness is mainly associated with the DNA itself.

In contrast, dissipative part (Fig. 9.4b) is expected to reflect viscosity of both

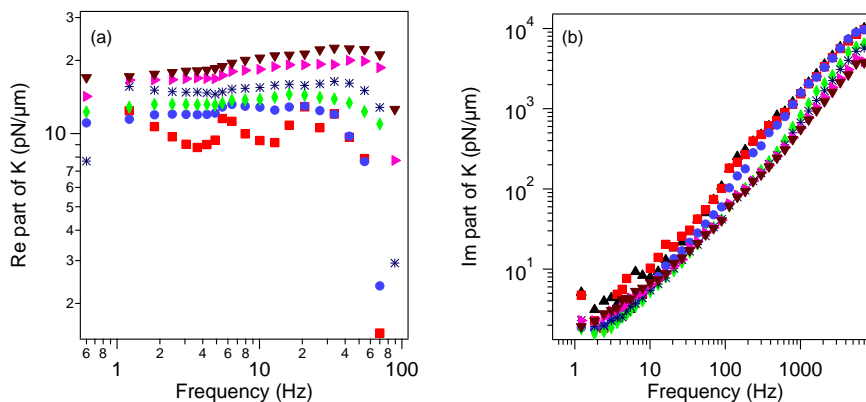


Figure 9.4: (a) Real part of the complex stiffness (K) as a function of frequency at various stretches of DNA. Data for beads with DNA is not shown as PBS acts as a purely viscous medium. (b) Imaginary part of the complex stiffness in the absence and presence of DNA: black up triangle - without DNA, red square - the DNA at rest (72.7%), light blue circle - the DNA stretched to 85.8%, light green diamond - the DNA stretched by 90.9%, dark blue cross - the DNA stretched by 91.86%, pink right triangle - the DNA stretched to 93.5%, brown bottom triangle - the DNA stretched to 94.3%. Complex stiffness was calculated using response functions corrected for the presence of two traps.

PBS and the DNA. Imaginary part of stiffness grows linearly with frequency as shown in Fig. 9.4b. Interestingly, the dissipative part of DNA does not change by any noticeable amount for forces in the entropic regime. For no DNA in between and for DNA in the relaxed state, the dissipative part almost overlaps with each other. Above the entropic regime though, the dissipative part starts to decrease. This effect indicates that at higher stretches, coupling of beads is dominated by DNA and the effect of hydrodynamic interaction decreases, as is also evident from cross-correlation function. This effect is expected as at higher stretches, DNA behaves like a thin rod with high elasticity. Nevertheless, it is not straightforward to deduce the effect of DNA from hydrodynamic interaction.

9.3 Conclusion

These studies show that two beads microrheology measurements performed on single DNA demonstrates a strong dependence of DNA mechanical properties on frequency. Cross-correlation measurement of bead fluctuations in absence as well as presence of DNA was calculated and showed to match with previous results. The cross-correlation function along with real part of response function shows a predominant elastic behavior of DNA at a stretching of $\sim 85\%$. The power spectral density shows an increase in energy of the system with stretching, implying an increase in the elasticity of the system. When there is no force acting on the DNA molecule, then almost all its mechanical properties (PSD, cross-correlation, response function) compares with that of beads without DNA in between. DNA elasticity shows a strong nonlinearity as it increases

with stretching. The elastic component has negligible frequency dependence for forces below entropic regime but shows a increase in elasticity with frequency at higher forces. The dissipative component of DNA stiffness increases with frequency but decreases when external force above entropic regime is applied. Similar frequency dependent mechanical studies of single DNA at higher forces and in overstretching region can open a new window of understanding.

10

Conclusions

Since the advent of single molecule techniques such as optical tweezers, atomic force microscope, magnetic tweezers etc, mechanical studies of single cells and biomolecules have taken an unprecedented boost. Later the combination of spectroscopic techniques such as Raman spectroscopy, opened new horizons in understanding the single biomolecules and cells at the molecular level. But till now there has been a gap in taking full advantage of these techniques. Not much work has been accomplished in the direction of combining mechanical deformation with spectroscopic techniques. This thesis is a step towards combining the two techniques within one system. Thus, correlating mechanical forces measurements with monitoring of structural information and chemical processes provides an ideal method for revealing new insights that either of the technique alone would not be able to provide.

We have demonstrated the importance of frequency dependent mechanical studies of single RBC and single DNA. Till now static studies on both these biosystems have been performed extensively, but not much is known about the dynamic properties in extended frequency range. We have found that both DNA and RBC exhibit nonlinear properties when the force applied to them exceeds a certain minimum level.

Raman spectra of single red blood cells have been previously demonstrated but most of these studies were done by trapping the cell directly in the beam focus. Ideally, this is not a non-invasive technique as cells in beam focus can undergo heating as well as photodegradation. We successfully demonstrated Raman signal from RBC at different stretches, trapped in dual trap optical tweezers, using $3\ \mu\text{m}$ polystyrene beads as handles to manipulate the cell. This configuration allowed us to take measurements for longer periods time and for larger forces, both virtues would be inaccessible if the cell was trapped directly in the beam focus. We were able to relate the nonlinear phenomena observed in case of microrheology with the molecular changes observed in Raman spectra of RBC.

We have, for the first time, shown Raman signal from single dsDNA molecule

in physiological condition. This was made possible by using SERS effect to enhance the Raman signal. Our work demonstrates an impactful methodology that adds a new dimension to the single molecule force spectroscopy field. SERS allows detection of single molecules without tags attached to it while interrogating the system at the bond level.

To summarize, following are the results that I have achieved in my thesis:

- We have shown the possibility of taking Raman spectra from a single dsDNA molecule in physiological conditions, using SERS technique.
- We went a step forward by detecting the Raman signal from a single dsDNA at different mechanical loads. We found that the phosphate backbone undergoes some structural rearrangements even in entropic force regime.
- Mechanical response of single RBC at various incremental steps was studied and the results were complemented by simultaneous Raman measurements. We were able to show a connection between RBC's nonlinearity with changes in molecular conformation.
- We exploited statistical techniques, such as 2d correlation spectroscopy and principal component analysis, to get an in-depth information from Raman signal.
- Frequency dependent cross-correlation measurements were conducted on single DNA molecule. The results show an onset of nonlinearity near the entropic force regime.

Mechanical deformation of single biosystem, complimented by Raman spectroscopy is a very powerful technique and can open new windows of understanding the changes happening inside cells and biomolecules at the molecular level.



Protocols for DNA construct

Here I am going to present the protocol that we implemented in obtaining the DNA molecule of desired length and with biotin and digoxigenin tags attached to its opposite ends via polymerase chain reaction (PCR). For all the purposes water means milliQ water and all the eppendorfs used were autoclaved.

A.1 PCR protocol for amplifying DNA

This protocol was used to amplify a λ -DNA molecule of 12kbp in length. Following are the list of chemicals used for this purpose:

dCTP (Roche, 11051458001), dGTP (Roche, 11051466001), dTTP (Roche, 11051482001), dATP (Roche, 11051440001); PCR system enzyme mix (Taq) and PCR buffer 2 (Roche, Expand high fidelity PCR system); biotin (Invitrogen), digoxigenin (TIB MOL BIOL); DNA marker (Invitrogen, Trackit, λ -DNA/Hind III fragments, 10488-064); TAE buffer (Sigma, T9650); agarose (Conda, 8016); Ethidium Bromide; DNA purification kit (GE, illustra GFX PCR DNA and gel band purification kit, 28-9034-70). Raw DNA sample was obtained from Prof. Llagostera group in Universitat Autònoma de Barcelona.

The PCR process can be divided into two parts and usually spans over two days. In first part, the necessary chemical are mixed together to form a PCR mixture and then put in the PCR machine (Labnet, Multi Gene II) for overnight reaction. It is recommended to carry out the first step in the evening, so that the PCR mixture does not sit in the machine for a long time. Before mixing the chemicals together, it is always better to make aliquots of them. Making aliquots serve two purposes: it protects the stock sample from getting contaminated and it avoids the continuous thawing and freezing of stock, which is not considered good for chemical stability. To make aliquots:

- 460 μ l of water + 10 μ l each of dGTP, dATP, dTTP, dCTP together. From now onwards we will call this mixture as dNTP.

- 25 μ l of PCR buffer 2 from stock.
- 5 μ l of Oligo's to 45 μ l water.
- 10 μ l of enzyme (Taq) from stock.

All the above aliquots are kept at -20 °C. They should be taken out of the freezer and thawed properly just before using them. Its better to shake them a bit so that the solution becomes homogeneous. To make the PCR mixture, all the chemicals are mixed in the following fashion in an eppendorf kept on ice (or ice tray):

- 170 μ l of water
- 25 μ l PCR buffer 2
- 25 μ l dNTP mixture
- 12.5 μ l Biotin
- 12.5 μ l Digoxigenin
- 10 μ l of enzyme (Taq). The enzyme is mixed at the end as it is most vulnerable to contamination
- 1 μ l of DNA for every 110 μ l of PCR solution. So in this case total DNA volume required would be 2.5 μ l.

Above mixture is spun for 30 seconds at 2000 rpm and divided in aliquots of 50 μ l before putting into PCR machine. The PCR machine was programmed to follow the steps in following sequence:

- 94 °C - 2 min
- 94 °C - 30 s, 52 °C - 30 s, 68 °C - 10 min - 10 cycles
- 94 °C - 30 s, 52 °C - 30 s, 68 °C - 10 min+5 s/cycle - 20 cycles
- 72 °C - 7 min
- Hold - 4 °C

The mixture is left overnight in PCR machine. Next day morning, before switching off the machine, preparation for DNA purification should be done. The purification has two steps - recognizing and separating the 12 kbp band from other band and purifying it. Recognition is done by the process known as agarose-gel electrophoresis. It is process in which various strands are separated by the application of electric field. The steps to carry agarose-gel electrophoresis is as follows:

- Making agarose gel: For 14kb - 0.6% agarose is used. 0.6 mg agarose powder to 100 ml of TAE buffer. Our electrophoresis tray uses 70 ml.
- Heat agarose solution in microwave until powder is dissolved.

- The electrophoresis system comes with small tray which is open at the opposite ends. Use tape to block in sides of tray to hold agarose gel solution.
- The system also has a comb with uniformly spaced tooth to create uniform holes in the agarose gel. Use tape to create proper sized holes depending on volumes of PCR solution. Put comb in tray about 5 mm above tray surface.
- Wait for agarose to cool until steam stops and then add 5 μ l of ethidium bromide for every 100 ml of agarose solution. It is important to see that no steam is coming out of agarose gel, so that ethidium bromide (a mutagenic reagent) does not spread in the room as vapor. Mix and immediately pour in to tray.

The agarose gel should solidify in 30-45 minutes. In the meanwhile we can prepare the PCR solution for agarose-gel electrophoresis. Following steps are taken for this purpose:

- Remove eppendorfs from PCR machine. PCR solution eppendorfs can be handled in normal temperature trays.
- Combine all the mixture into one eppendorf. The final amount should be 250 μ l amounts.
- Add load buffer from stock 1:10 (buffer:PCR solution) to the PCR product
- Remove tape after the agarose gel is solidified. Then carefully remove the comb.
- Put this tray in the electrophoresis unit with electrodes. Fill with TAE buffer until gel is completely covered by liquid.
- Place the black blocks, supplied with electrophoresis equipment, beneath the gel in order to see the holes.
- Add 10 μ l of DNA marker solution in the small hole generated by comb in the agarose gel.
- Add all of PCR solution to the big holes. Remember PCR mixture is placed at negative end of tray.
- Set power supply to 90V constant voltage. Push start on power supply and check for bubbles on black electrode to ensure current is running.
- After \sim 45 minutes lines should separate enough for distinguishing the bands. Final output in UV light looks like Fig. A.1.
- Locate 12kbp band based on marker band positions. Usually it is the most intense band in the gel.
- Cut the lines out of the gel and place in to eppendorf. Measure the weight of gel that has been cut out. Remember not to put more than 700 mg of gel in one eppendorf as it can create problem during gel purification.

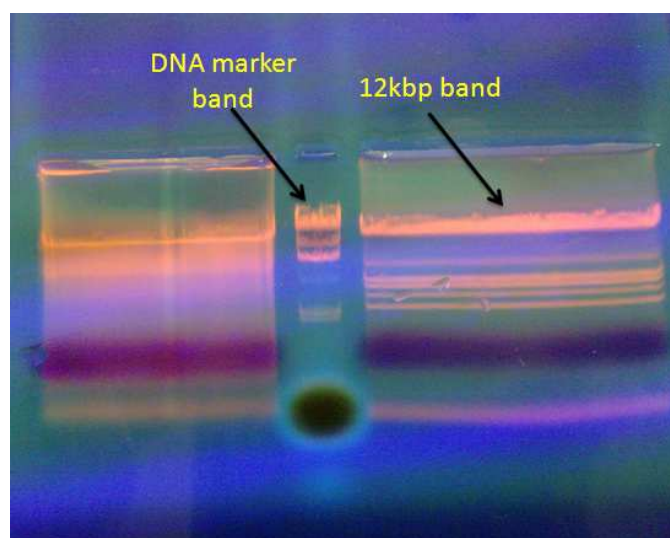


Figure A.1: DNA bands seen after agarose-gel electrophoresis under UV light.

The gel purification is carried out using GE get purification kit and the steps are followed as exactly described in the protocol. Once the gel is purified, the DNA is eluted in $50 \mu\text{l}$ of water. For this purpose, the filter column containing DNA after purification is placed on a new eppendorf and $50 \mu\text{l}$ is added to it. The sample is then allowed to sit for 60 seconds and then centrifuged at maximum speed for 45 seconds. Save the water obtained after centrifuge as it contains the purified DNA. To maximize the quantity of DNA obtained, next we can repeat the elution process on another new eppendorf with $30 \mu\text{l}$ of water. First elution gives the maximum density of DNA.

A.2 DNA preparation through digestion of λ -DNA

In this protocol some modifications is done to the commercially available λ -phage DNA to be able to manipulate it with the optical tweezers. This chain of modifications, whose final objective is to label one end of the DNA with biotins and the other end with digoxigenins, is explained in this section. The first step of the process is to reduce the size of the experimental molecule through a digestion as the λ -DNA has a contour length of $17.2 \mu\text{m}$, which is very big as per the convenience of carrying out the experiments. The list of chemicals required in this case are as follows:

λ -DNA (methyl free, New England Biolabs); Millipore filters; QIAquick Nucleotide removal kit; Biotin-16-dUTP (Roche11093070910); DIG Oligonucleotide tailing kit 2nd Generation (Roche, Ref: 03353583910); T4 DNA ligase (Roche, Ref: 10481220001); XbaI (Roche, Ref: 10674257001); Wizard DNA clean-up system (Promega, Cat: A7280); Sodium Azide (Scharlau; Cat: SO0091); BSA (New England Biolabs, Cat: B9001S); NE buffer 2 (New England Biolabs, Cat: B7002S); T4 Polynucleotide Kinase (New England Biolabs, Cat: M0201S); ATP (New England Biolabs, Cat: P0756S); EDTA (Sigma, Cat:

E9884 - 500G); TRIS (Sigma, Cat: T1503-500G); Oligos SOC-LE (Custom orderer from Sigma, Sequence:); Oligos XbaI50 (Custom orderer from Sigma, Sequence:); Oligos XbaI5D (Custom orderer from Sigma, Sequence:).

SOC-LE, XbaI50 and XbaI5D has following sequence respectively:

- 5'-AGGTCGCCGCCCAAAAAAAAAAAAAA-3'
- 5'-CTAGACCCGGGCTCGAGGATCCCC-3'
- 5'-GGGGATCCTCGAGCCCGGGT-3'

A.2.1 λ -phage DNA Digestion

As stated, we need to cut DNA into two smaller fragments as the contour length is too big for comfort. In this section I will describe how to carry out digestion of 10 μg of DNA. For the digestion of 10 μg of DNA at a total volume of 400 μl we have mixed the chemicals in following steps in an eppendorf:

- 330 μl of miliQ water.
- 20 μl of λ -DNA at 500 $\mu\text{g}/\text{ml}$
- 40 μl of NE Buffer2 at 10X (1X: 50 mM NaCl, 10mM Tris HCl, 10 mM MgCl_2 , 1mM DTT, pH 7.9 at 25 °C)
- 4 μl of BSA protein at 100X (1X:100 $\mu\text{g}/\text{ml}$)
- 6 μl of XbaI restriction enzyme at 20,000U/ml (1 U digests 1 μg of λ -DNA in 1 hour in a total volume of 50 μl at 37 °C)

After gently mixing and centrifugation the solution is incubated in water bath at 37 °C for 4 hours. After incubation, the solution is purified using the WIZARD DNA clean-up system kit (Promega) in order to isolate the digested DNA.

A.2.2 Preparation of the oligonucleotides

In order to attach the biotins and digoxigenins to the DNA we prepared two single stranded oligonucleotides complementary to the cohesive ends of the digested DNA.

Oligonucleotide SOC-LE (Digoxigenins)

For the tailing with digoxigenins of 100pmol of the oligonucleotide SOC-LE we have used the reagents in following steps:

- 8 μl of sterile miliQ water
- 1 μl of SOC-LE oligonucleotide at 100 pmol/ μl
- 4 μl of reaction buffer at 5X (5X: 1M potassium cacodylate, 0.125M Tris HCl, 1.25mg/ml bovine serum albumine, pH 6.6 at °C)
- 4 μl CoCl_2 solution (25mM)

- 1 μ l of DIG-dUTP solution
- 1 μ l dATP solution (10mM in miliQ water)
- 1 μ l of terminal transferase enzyme at 400U/ μ l (in 60 mM K-phosphate (pH 7.2 at 4 °C), 150 mM KCl, 1 mM 2-Mercaptoethanol, 0.5% Triton X-100, 50% glycerol)

After adding the sterile miliQ water to the SOC-LE oligonucleotide solution to reach a total final volume of 9 μ l, the reagents are added in the eppendorf on ice. The solution is mixed and centrifuged briefly and incubated for 15 min at 37 °C. Then placed again on ice and the reaction is stopped by adding the chelating agent EDTA (2 μ l of a 0.2 M EDTA solution at pH 8.0).

Biotinylation of 100 pmol of XbaI50 oligonucleotide

For the tailing with biotins of 100 pmol of the oligonucleotide XbaI50 we used the following reagents:

- 8 μ l of sterile miliQ water
- 1 μ l of XbaI50 oligonucleotide at 100 pmol/ μ l
- 4 μ l of reaction buffer at 5X (5X: 1M potassium cacodylate, 0.125M Tris HCl, 1.25mg/ml bovine serum albumine, pH 6.6 at °C)
- 4 μ l CoCl₂ solution (25mM)
- 1 μ l of biotin-dUTP solution (1mM in miliQ water)
- 1 μ l dATP solution (10mM in miliQ water)
- 1 μ l of terminal transferase enzyme at 400U/ μ l (in 60 mM K-phosphate (pH 7.2 at 4 °C), 150 mM KCl, 1 mM 2-Mercaptoethanol, 0.5% Triton X-100, 50% glycerol)

For the biotinylation we proceeded as in the tailing with digoxigenins, but using a solution of biotin-labeled deoxyuridine-triphosphate (biotin-dUTP) instead of the DIG-dUTP. Thus, after dissolving the XbaI50 oligonucleotide solution in the sterile miliQ water, we added the other reagents on ice. The solution is mixed and centrifuged briefly and incubated for 15 min at 37 °C. Then placed again on ice and the reaction is stopped by adding the chelating agent EDTA (2 μ l of a 0.2 M EDTA solution at pH 8.0).

A.2.3 Purification of the oligonucleotides

After labeling the oligonucleotides with digoxigenins and biotins, and before doing further reactions, we will need to purify the oligonucleotide solutions for several reasons. In order to stop the biotinylation and digoxigenin-labeling of the oligonucleotides, we have added EDTA to the XbaI50 and SOC-LE solutions. EDTA is a chelating agent that binds to di- and trivalent metal ions, making especially strong complexes with Mn²⁺, Cu²⁺, Fe³⁺ and Co³⁺ and can interfere with the activity of enzymes. Therefore we will have to purify the oligonucleotide solutions to take out the remaining EDTA, otherwise we would

not be able to perform the next reactions. Purification also helps in getting rid of unincorporated nucleotides, enzymes, salts and defective oligonucleotides that might have been created during the previous reaction.

For the purification of the oligonucleotides we have used the QIAquick Nucleotide removal kit (QIAGEN) that allows us to recover DNA fragments and oligonucleotides >17 nucleotides, taking out the smaller ones. We followed the steps as described in the protocol supplied by the kit. At the end of elution (carried out in 50 μ l elution buffer), we get the 50 μ l (SOC-LE + DIG) oligonucleotides (100pmol) and 50 μ l (XbaI50+Biotin) oligonucleotides (100pmol).

A.2.4 Phosphorylation of the oligonucleotides

After tailing and purification of oligonucleotides, we need to hybridize them with DNA molecule. However, before doing so we will have to phosphorylate both the XbaI50, SOC-LE and XbaI5D oligonucleotides. Phosphorylation is a process by which a phosphate group (PO_4^-) is attached to a molecule, in this case the 5'-carbon of a nucleotide.

Phosphorylation of the SOC-LE oligonucleotide

To carry out the phosphorylation of SOC-LE oligonucleotide, following reagents were mixed together to reach a final volume of 100 μ l:

- 50 μ l of SOC-LE oligonucleotides
- 22 μ l of miliQ water
- 10 μ l of ligase buffer solution at 10X
- 10 μ l of 10mM ATP
- 8 μ l of T4 polynucleotide kinase at 10U/ μ l

All the above solution was mixed on ice. After combining the reagents and mixing gently, the mixture is incubated for 30 minutes at at 37 °C.

Phosphorylation of the XbaI50 and XbaI5D oligonucleotide

The only difference with the SOC-LE phosphorylation is that in this case, at the same time that the phosphorylation takes place we will hybridize the two complementary oligonucleotides, to simplify later the ligation process with the λ -DNA. Thus the procedure used will be exactly the same to that used in the phosphorylation of SOC-LE except for:

- Use the 50 μ l of XbaI50 oligonucleotides instead of the SOC-LE solution.
- Add 1 μ l of XbaI50 oligonucleotides solution (100pmol/ μ l).

Rest all of the steps is as in the case of SOC-LE oligonucleotide. As before, we mix and incubate the mixture for 30 minutes at at 37 °C.

From now on we will refer to the hybridized oligonucleotides XbaI50 and XbaI5D as XbaI50/5D.

A.2.5 Annealing and ligation of the oligonucleotides with the DNA

Add 5 μl of SOC-LE oligonucleotide to the DNA solution, purified after restriction reaction. The resulting solution is mixed and incubated for 10 minutes at 68 °C in water bath, in order to get DNA strands and oligonucleotides completely melted and extended and thus avoid strange hybridization. After incubation, 10 μl of XbaI50/5D oligonucleotides is added and again incubated in water bath at 42 °C for 1 hour.

After the incubation is complete, let it cool down to ~ 20 °C and then store it in freeze at 4 °C for sometime so that all the strands are correctly hybridized and ready to ligate.

For ligation, following reagents are mixed on ice in the described order:

- 58 μl hybridized DNA and oligonucleotides solution (all).
- 8 μl ligase buffer at 10X.
- 1 μl of milliQ water.
- 10 μl of 10mM ATP.
- 3 μl T4 DNA ligase at 1U/ μl .

After mixing, the reagents are incubated overnight at 16 °C.

Finally to stop the reaction and to store the DNA in a more appropriate buffer, we perform the dialysis to EDTA-Tris buffer (10 mM Tris, pH 8.0; 1mM EDTA; 10 mM NaCl).

B

Protocol describing Labview program for DNA extension

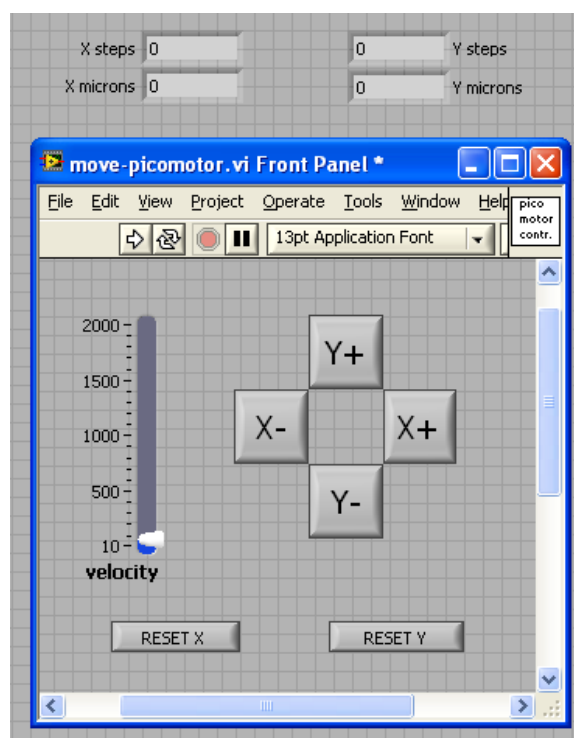
We have developed a program in Labview for automated measurement of force-extension curve of a DNA molecule in dual optical trap. This section describe the steps for using this program. There are few things to remember before using this program:

- Movement of trap can be either controlled manually or with the help of program by just toggling the state of “**MANUAL ON**” between ON and OFF.
- Only ONE of the three - “**MANUAL ON**”, “**CALIBRATION ON**”, “**STRETCHING ON**”, can be ON at one time. If we want to run a particular command, the other two should be OFF.
- ON state of a command means that the green LED beside it must be glowing. Similarly OFF state means that the LED is not glowing. An example is shown in fig. B.1.



Figure B.1: It can be seen from the figure that calibration state is off as the LED is not glowing while stretching state is on because the LED is glowing.

- There is a sub-VI called “**move picomotor**” (fig. B.2). This VI will appear as soon as “**CALIBRATION ON**” or “**STRETCHING ON**” is clicked. This VI is used to move the trap position through program in X and Y directions. There is a velocity bar on the left of this VI. It defines how fast the trap position will move when we click on any of the four - X- (left), X (right), Y- (down), Y (up).

Figure B.2: Screen-shot of sub-VI *move picomotor*.

B.1 Experiment's Outlook

The Experiment consists of dual trap. One of the traps is fixed while the other can be moved with the help of picomotor. Two beads of different sizes and different chemistry are trapped in the two traps. Smaller bead with streptavidin (strep) coating on it is trapped in the fixed trap while bigger bead with digoxigenin (DIG) coating is trapped in movable trap. Once the bead-DNA construct is made, then movement of DIG bead away from strep bead leads to the stretching of DNA. By monitoring the displacement of strep bead we can evaluate the force acting on DNA. Strep bead displacement is monitored with the help of position detection beam that is coaxial with trapping laser (T1).

B.2 Calibration of moving trap and picomotor

As the experiment consists of only one detection beam, we need to first calibrate the set-up for DIG bead. Block the path of beam that traps strep bead (T1). DIG bead is trapped at T2 and moved at the same position where T1 is present. To make sure that the detection beam is passing through the centre of DIG bead, look for the fringes that are formed due to back-scattered light. Fringes formed should be symmetric and circular in shape. Adjust the position of bead with help of joystick until the fringes become symmetric.

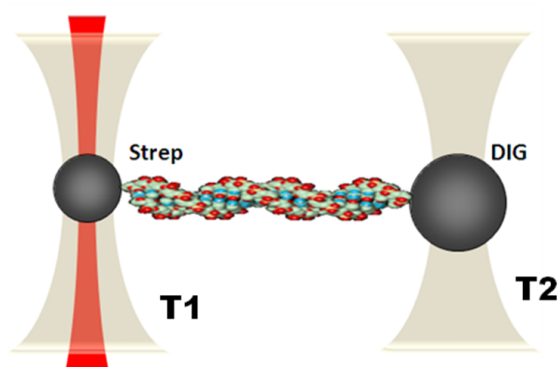


Figure B.3: A schematic representation of experimental outlook.

Be in “**calibration**” window of the program. Now switch off the “**MANUAL ON**” command and click on “**CALIBRATION ON**” button to make it active. After adjusting the QPD, so that average Brownian motion value is almost zero, wait for 30 sec to accumulate data. Then deactivate the “**CALIBRATION ON**” button.

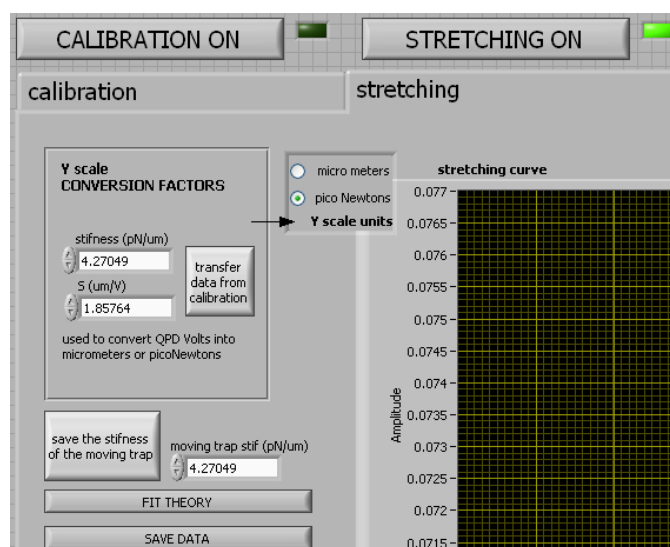


Figure B.4: A screen-shot of stretching window used in the program.

- Switch to “**stretching**” window. Activate “**STRETCHING ON**” by clicking on it (fig B.4).
- Transfer the values of trap stiffness and conversion factor by clicking on “**transfer data from calibration window**”.
- Save this stiffness value for further analysis using “**save the stiffness of**

the moving trap” command.

- Move the trapped bead a bit to the left by clicking on “X-” button on “**move-picomotor**” window. We just need to move the bead by approximately $1 \mu\text{m}$.
- Keep the Y-scale unit at micrometers and X-scale unit at motor steps (fig. B.5a). They are present diagonally opposite to each other near “**stretching curve**” window.
- Define the motor steps and motion velocity that we need to use. Step size is usually around 50 units while motion velocity is kept around 500 units. Step size usually depends upon how many steps we want to take while stretching the DNA. If more steps are required then keep the step size small and vice-versa.
- Click on “**START MEASUREMENT**” button. Remember to keep the correction factor off (fig. B.6).
- A graph will appear in stretching curve window that will go from non-linear plot to linear and then back to non-linear. Stop the measurement as soon as you see the linear part disappear by clicking on “**STOP MEASUREMENT**” (fig. B.5b).

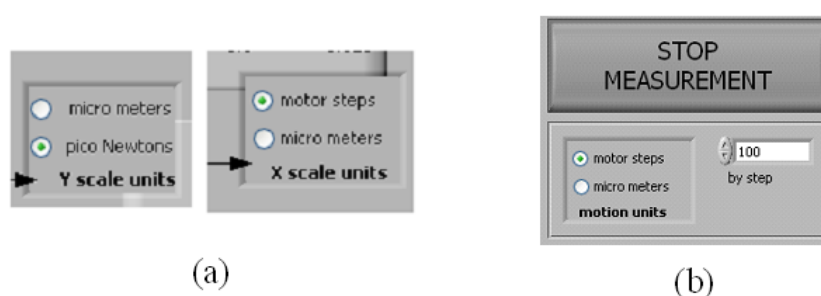


Figure B.5: A screen-shot describing units used during running the program.

Now toggle the status of “**STRETCHING ON**” from ON to OFF. Select a linear range in the graph using markers, with green marker at the beginning and red at the end of the curve (fig. B.6) and again toggle “**STRETCHING ON**” to ON state. Click on “**FIT LINEAR to get alpha**” to calibrate the picomotor at desired step size (i.e. to convert step size into nanometers).

- Move the trapped DIG bead to its previous position and unblock the laser that we blocked previously (T1). Trap streptavidin bead in T1.
- Toggle the “**STRETCHING ON**” state to OFF and move to “**calibration**” window of the program.
- Activate “**CALIBRATION ON**” state to ON. Take the trap calibration data as mentioned previously for DIG bead.

- Toggle the “**CALIBRATION ON**” state to OFF and move to “**stretching**” window. Toggle the “**STRETCHING ON**” to ON state and transfer the calibration values of strep bead to stretching part by clicking on “**transfer data from calibration**”. Also transfer the histogram value from calibration window by clicking on “**transfer histogram center X**” (fig. B.6).

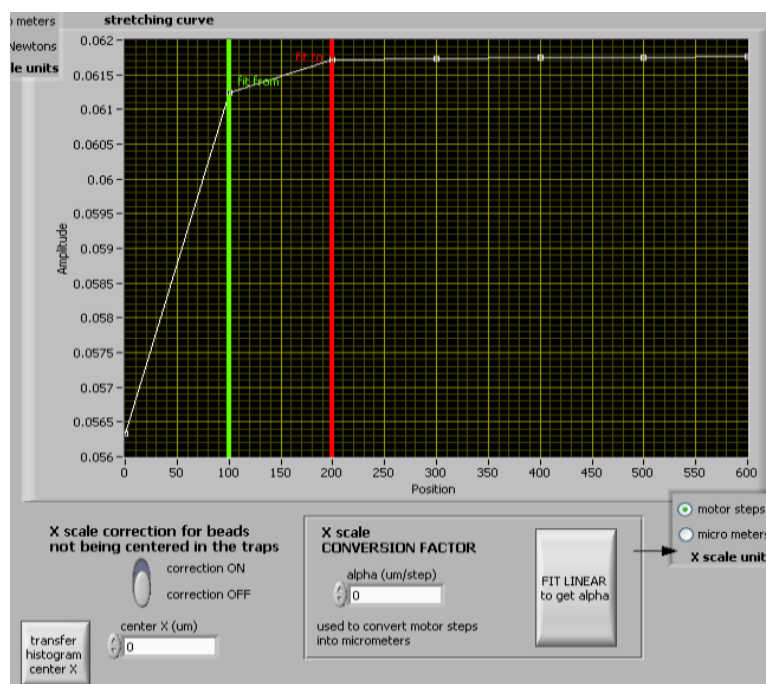


Figure B.6: A screen-shot showing the interface of stretching curve window.

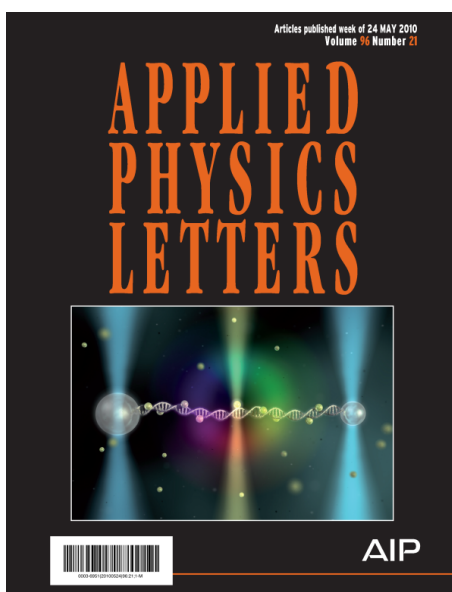
Now make DNA connection by approaching the two trapped beads closer. DNA binding occurs in few seconds. Move the DIG bead away to check whether the binding has occurred or not. Remember we can always move the joystick manually by toggling the “**MANUAL OFF**” to ON state. After it’s certain that there is a DNA in between two beads, bring the two beads close again such that they are just touching each other. Reset the value of X and Y to zero (fig. B.2) and change the Y and X scale units to “**pico Newtons**” and “**micro meter**” from “**step size**” and “**motor steps**” respectively (fig. B.5a).

Start measurement by clicking on “**START MEASUREMENT**” button. Switch on the correction term. Take the measurement until QPD reaches the non-linear regime or the DNA breaks. We will observe a stretching curve in the “**stretching curve**” window that should look like the WLC model.

Save the data obtained by clicking on “**SAVE DATA**” button. A window will appear where we can select the folder in which we want to save our data.

Annex 1: List of Publications of Saurabh Raj

- S. Rao, S. Raj, S. Bálint, C. B. Fons, S. Campoy, M. Llagostera and D. Petrov: *Single DNA molecule detection in an optical trap using surface-enhanced Raman scattering*; Applied Physics Letters; **96** (21): (2010) - cover page



- I. A. Martinez, S. Raj and D. Petrov : *Colored noise in the fluctuations of an extended DNA molecule detected by optical trapping*; Eur. Biophys. J.; **41**: (2012)
- S. Raj, M. Marro, M. Wojdyla and D. Petrov : *Mechanochemistry of single red blood cells monitored using Raman tweezers*; Biomed. Opt. Express; **3**: (2012)
- S. Rao, S. Raj, B. Cossins, M. Marro, V. Guallar and D. Petrov: *DNA structure effects at low forces revealed by surface-enhanced Raman scattering*; accepted in Biophys. J.; (2012)
- S. Raj, M. Wojdyla and D. Petrov: *Studying single red blood cells under a tunable external force by combining passive microrheology with Raman spectroscopy*; submitted in Cell Biochemistry and Biophysics; (2012)
- M. Wojdyla, S. Raj and D. Petrov: *Absorption spectroscopy of single red blood cells in the presence of mechanical deformations induced by optical traps*; accepted in Journal of Biomedical Optics; (2012)

- M. Marro, S. Raj, S. Rao, A. Taubes, P. Villoslada, and D. Petrov : *Using 2D correlation and multivariate analysis combined with plasmonic effects to expand the use of Raman microspectroscopy in biomedical applications*; Proc. SPIE; 8087, 80871H (2012)
- S. Raj, S. Rao, M. Marro Sanchez, M. Wojdyla and D. Petrov : *Load bearing studies of single DNA molecules and red blood cells using optical tweezers and Raman spectroscopy*; Proc. SPIE; 8427, 842719 (2012)
- S. Raj, M. Wojdyla, and M. Marro Sanchez and D. Petrov : *Force and Raman spectroscopy of single red blood cell*; Proc. SPIE; 8427, 842712 (2012)
- Ignacio A. Martinez, S. Raj and D. Petrov : *Optical trapping detects colored noise in the fluctuations of an extended DNA molecule*; Proc. SPIE; 8427, 84270V (2012)

Annex 2: Conferences and workshops

- S. Raj, S. Rao and D. Petrov : *Optical trapping system for active microrheology of single biosystems* (poster); Photonics4Life – Annual Meeting; Florence, Italy: (2009)
- S. Raj, S. Rao and D. Petrov : *Strain induced DNA structural changes revealed with optical tweezers and surface-enhanced Raman spectroscopy* (talk); Photonics 2010; Guwahati, India: (2010)
- S. Raj, S. Rao and D. Petrov : *Optical trapping system for active microrheology of single biosystems* (poster); 4th International Graduate Summer School: Biophotonics '09; Hven, Sweden: (2009)
- S. Raj, M. Wojdyla, and M. Marro Sanchez and D. Petrov : *Force and Raman spectroscopy of single red blood cell* (talk); SPIE-Photonics Europe; Brussels, Belgium: (2012)
- S. Raj, S. Rao, M. Marro Sanchez, M. Wojdyla and D. Petrov : *Load bearing studies of single DNA molecules and red blood cells using optical tweezers and Raman spectroscopy* (talk); SPIE-Photonics Europe; Brussels, Belgium: (2012)

Annex 3: List of elements used in the optical set-ups

Raman set-up with 785 nm excitation beam

- **Trapping beam:** 1064 nm, 1000 mW, Laser Quantum Limited, Manchester, England
- **Raman excitation beam:** 785 nm, 90 mW, Micro Laser systems Inc
- **Position detection beam:** 633 nm, 5 mW, He-Ne laser, Research Electro-optics Inc.; Model no. LHRP-0501
- **Objective:** Nikon, oil immersion, 100X, 1.3NA
- **Spectrometer:** SpectraPro 2500i spectrometer (Acton research, USA)
- **Spectrometer camera:** Spec-10:100B thermoelectrically controlled charge-coupled device (Princeton Instruments, USA)
- **Imaging camera:** CCD color camera (JAI)
- **QPD:** New Focus, model 2991
- **Picomotor:** New Focus, 8807

Raman set-up with 532 nm excitation beam

- **Trapping beam:** 985 nm, 400 mW, Arroyo Instruments
- **Raman excitation beam:** 532 nm, 50 mW, RGBLase optical fiber coupled laser
- **Position detection beam:** 635 nm, 5 mW Coherent laser
- **Objective:** Nikon, oil immersion, 100X, 1.3NA
- **Spectrometer:** Andor Shamrock 163
- **Spectrometer camera:** Andor iDus camera
- **Imaging camera:** CCD color camera (JAI)
- **QPD:** New Focus, model 2991
- **Picomotor:** New Focus, 8807

Microrheology set-up

- **First trapping beam:** 1064 nm, 3000 mW, Manlight
- **Second trapping beam:** 850 nm, 200 mW, Arroyo instruments
- **Position detection beam for 1064 nm trap:** 532 nm, 50mW, RG-BLase optical fiber coupled laser
- **Position detection beam for 850 nm trap:** 635 nm, 5 mW Coherent laser
- **Objective:** Nikon, oil immersion, 100X, 1.3NA
- **Acousto-optic deflector:** ISOMET LS55
- **ADC converter:** National Instruments, BNC 2110
- **Imaging camera:** CCD color camera (JAI)
- **QPD:** New Focus, model 2991
- **Picomotor:** New Focus, 8807

Bibliography

- [1] D. E. Discher, P. Janmey, and Y. L. Wang. Tissue cells feel and respond to the stiffness of their substrate. *Science*, 310:1139–1143, 2005.
- [2] J. C. Meiners and S. R. Quake. Femtonewton force spectroscopy of single extended DNA molecules. *Phys. Rev. Lett.*, 84:5014–5017, 2000.
- [3] F. Ritort. Single-molecule experiments in biological physics: methods and applications. *J. Phys.: Condens. Matter*, 18:R531–R583, 2006.
- [4] S. R. Quake, H. Babcock, and S. Chu. The dynamics of partially extended single molecules of dna. *Nature*, 388:151–154, 1997.
- [5] P. A. Janmey and D. A. Weitz. Dealing with mechanics: mechanisms of force transduction in cells. *Trends Biochem. Sci.*, 29:364–370, 2004.
- [6] D. Mizuno, C. Tardin, C. F. Schmidt, and F. C. MacKintosh. Nonequilibrium mechanics of active cytoskeletal networks. *Science*, 315:370–373, 2007.
- [7] M. R. K. Mofrad and R. D. Kamm. *Cytoskeletal Mechanics: Models and Measurements*. Cambridge University Press, Cambridge, England, 2006.
- [8] D. T. N. Chen, Q. Wen, P. A. Janmey, J. C. Crocker, and Arjun G. Yodh. Rheology of soft materials. *J. Opt. A: Pure Appl. Opt.*, 1:301–322, 2010.
- [9] M. L. Gardel, M. T. Valentine, and D.A. Weitz. *Microscale Diagnostic Techniques*. Springer, 2005.
- [10] M. Atakhorrami, D. Mizuno, G.H. Koenderink, T.B. Liverpool, F.C. MacKintosh, and C.F. Schmidt. Short-time response of viscoelastic fluids measured with Brownian motion and with active probes. *Phys. Rev. E*, 77:061508, 2008.
- [11] J. C. Crocker, M. T. Valentine, E. R. Weeks, T. Gisler, P. D. Kaplan, A. G. Yodh, and D. A. Weitz. Two-point microrheology of inhomogeneous soft materials. *Phys. Rev. Lett.*, 85:888–891, 2000.
- [12] D. Mizuno, D. A. Head, F. C. MacKintosh, and C. F. Schmidt. Active and passive microrheology in equilibrium and nonequilibrium systems. *Macromolecules*, 41:7194–7202, 2008.
- [13] E. Bailo and V. Deckert. Tip-enhanced Raman spectroscopy of single RNA strands: Towards a novel direct-sequencing method. *Angew. Chem. Int. Ed.*, 47:1658–1661, 2008.

- [14] D. Petrov. Raman spectroscopy of optically trapped particles. *J. Opt. A: Pure Appl. Opt.*, 9:S139–S156, 2007.
- [15] S. Rao, S. Raj, S. Balint, C. Bardina Fons, S. Campoy, M. Llagostera, and D. Petrov. Single DNA molecule detection in an optical trap using surface-enhanced Raman scattering. *Appl. Phys. Lett.*, 96:213701, 2010.
- [16] S. B. Smith, L. Finzi, and C. Bustamante. Direct mechanical measurements of the elasticity of single DNA molecules by using magnetic beads. *Science*, 258:1122–1126, 1992.
- [17] J. Mameren, M. Modesti, R. Kanaar, C. Wyman, G. J. Wuite, and E. J. Peterman. Dissecting elastic heterogeneity along DNA molecules coated partly with Rad51 using concurrent fluorescence microscopy and optical tweezers. *Biophys. J.*, 91:L78–L80, 2006.
- [18] J. van Mameren, P. Gross, G. Farge, P. Hooijman, M. Modesti, M. Falkenberg, G. J. L. Wuite, and E. J. G. Peterman. Unraveling the structure of DNA during overstretching by using multicolor, single-molecule fluorescence imaging. *Proceedings of the National Academy of Sciences*, 106:18231–18236, 2009.
- [19] M. A. van Dijk, L. C. Kapitein, J. van Mameren, C. F. Schmidt, and E. J. G. Peterman. Combining optical trapping and single-molecule fluorescence spectroscopy: Enhanced photobleaching of fluorophores. *J. Phys. Chem. B*, 108:6479–6484, 2004.
- [20] H. Fu, H. Chen, J. F. Marko, and J. Yan. Two distinct overstretched DNA states. *Nucleic Acids Research*, 38:5594–5600, 2010.
- [21] G. Singh, G. Volpe, C. Creely, H. Grotsch, I. Geli, and D. Petrov. The lag phase and G1 phase of a single yeast cell monitored by Raman microspectroscopy. *J. Raman Spectrosc.*, 37:858–864, 2006.
- [22] C. Creely, G. Volpe, G. Singh, M. Soler, and D. Petrov. Raman imaging of floating cells. *Opt. Exp.*, 12:6105–6110, 2005.
- [23] E. J. Blackie, E. C. Le Ru, and Pablo G. Etchegoin. Single-molecule surface-enhanced Raman spectroscopy of nonresonant molecules. *J. Am. Chem. Soc.*, 131:14466–14472, 2009.
- [24] S. Rao, S. Raj, B. Cossins, M. Marro, V. Guallar, and D. Petrov. DNA structure effects at low forces revealed by surface-enhanced Raman scattering. *Submitted*, 2012.
- [25] S. Raj, M. Wojdyla, and D. Petrov. Single red blood cell under tunable external force studied by combining passive microrheology and Raman spectroscopy. *Submitted*, 2012.
- [26] S. Raj, M. Marro, M. Wojdyla, and D. Petrov. Mechanochemistry of single red blood cells monitored using Raman tweezers. *Biomed. Opt. Express*, 3:753–763, 2012.
- [27] A. Ashkin. Acceleration and trapping of particles by radiation pressure. *Phys. Rev. Lett.*, 24:156–159, 1970.

- [28] A. Ashkin, J.M. Dziedzic, J.E. Bjorkholm, , and S. Chu. Observation of a single-beam gradient force optical trap for dielectric particles. *Opt. Lett.*, 11:288–290, 1986.
- [29] A. Ashkin and J.M. Dziedzic. Optical trapping and manipulation of viruses and bacteria. *Science*, 235:1517–1520, 1987.
- [30] A. Ashkin. Forces of a single-beam gradient laser trap on a dielectric sphere in the ray optics regime. *Biophys. J.*, 61:569–582, 1992.
- [31] K. Svoboda and A. Ashkin. Biological applications of optical forces. *Ann. Rev. Biophys. Struc.*, 23:247—285, 1994.
- [32] M. Kerker. *The scattering of light and other electromagnetic radiation*. Academic Press, New York, 1969.
- [33] A. Mazolli, P. A. Maia Neto, and H. M. Nussenzveig. Theory of trapping forces in optical tweezers. *Proceedings of the Royal Society A: Mathematical, Physical and Engineering Sciences*, 459:3021–3041, 2003.
- [34] K. Visscher, S. P. Gross, and S. M. Block. Construction of multiple-beam optical traps with nanometric-resolution position sensing. *IEEE J. of Sel. Topics in Quantum Electronics*, 2:1066 – 1076, 1996.
- [35] W. M. Lee, P. J. Reece, R. F. Marchington, N. K. Metzger, and K. Dhoklaka. Construction and calibration of an optical trap on a fluorescence optical microscope. *Nature Protocols*, 2:3226—3238, 2007.
- [36] D. C. Appleyard, K. Y. Vandermeulen, H. Lee, and M. J. Lang. Optical trapping for undergraduates. *Am. J. Phys.*, 75:5–14, 2007.
- [37] S. F. Tolić-Nørrelykke, E. Schäffer, J. Howard, F. S. Pavone, F. Jülicher, and H. Flyvbjerg. Calibration of optical tweezers with positional detection in the back focal plane. *Rev. Sci. Instrum.*, 77:103101, 2006.
- [38] L. P. Ghislain, N. A. Switz, and W. W. Webb. Measurement of small forces using an optical trap. *Rev. Sci. Instrumen.*, 65:2762–2768, 1994.
- [39] F. Gittes and C. F. Schmidt. Interference model for back-focal-plane displacement detection in optical tweezers. *Opt. Lett.*, 23:7–9, 1998.
- [40] C. V. Raman and K. S. Krishnan. A new type of secondary radiation. *Nature*, 121:501—502, 1928.
- [41] G. J. Puppels, C. Otto F. F. M. de Mul, J. Greve, M. Robert-Nicoud, D. J. Arndt-Jovin, and T. M. Jovin. Studying single living cells and chromosomes by confocal Raman microspectroscopy. *Nature*, 347:301–303, 1990.
- [42] J. Duguid, V. A. Bloomfield, J. Benevides, and G. J. Thomas. Raman spectroscopy of DNA-metal complexes. i. interactions and conformational effects of the divalent cations: Mg, Ca, Sr, Ba, Mn, Co, Ni, Cu, Pd, and Cd. *Biophys. J.*, 65:1916–1928, 1993.

- [43] D. Gill, R. G. Kilponen, and L. Rimai. Resonance Raman scattering of laser radiation by vibrational modes of carotenoid pigment molecules in intact plant tissues. *Nature*, 227:743–744, 1970.
- [44] J.C. Merlin. Resonance Raman spectroscopy of carotenoids and carotenoid-containing systems. *Pure Appl. Chem.*, 57:785—792, 1985.
- [45] M. Fleischmann, P. J. Hendra, and A. J. McQuillan. Raman spectra of pyridine adsorbed at a silver electrode. *Chem. Phys. Lett.*, 26:163—166, 1974.
- [46] D. L. Jeanmaire and A. P. Van Duyne. Surface Raman spectroelectrochemistry: part i. heterocyclic, aromatic, and aliphatic amines adsorbed on the anodized silver electrode. *Journal of Electroanalytical Chemistry*, 84:1—20, 1977.
- [47] M. G. Albrecht and J. A. Creighton. Anomalously intense Raman spectra of pyridine at a silver electrode. *J. Am. Chem. Soc.*, 99:5215—5217, 1977.
- [48] S. Nie and S. R. Emory. Probing single molecules and single nanoparticles by surface-enhanced Raman scattering. *Science*, 275:1102—1106, 1997.
- [49] E. Smith and G. Dent. *Modern Raman spectroscopy: A practical approach*. John Wiley and Sons, 2005.
- [50] P. Kambhampati, C. M. Child, M. C. Foster, and A. Campion. On the chemical mechanism of surface enhanced Raman scattering: Experiment and theory. *J. Chem. Phys.*, 108:5013–5026, 1998.
- [51] F.C. MacKintosh and C.F. Schmidt. Microrheology. *Current Opinion in Colloid and Interface Science*, 4:300–307, 1999.
- [52] L.D. Landau and E.M. Lifshitz. *Theory of Elasticity*. Butterworth-Heinemann, 1986.
- [53] G. Jiang, A. H. Huang, Y. Cai, M. Tanase, and Michael P. Sheetz. Rigidity sensing at the leading edge through $\alpha_v\beta_3$ integrins and RPTP α . *Biophys. J.*, 90:1804—1809, 2006.
- [54] M. Atakhorrami, J. I. Sulkowska, K. M. Addas, G. H. Koenderink, J. X. Tang, A. J. Levine, F. C. MacKintosh, and C. F. Schmidt. Correlated fluctuations of microparticles in viscoelastic solutions: Quantitative measurement of material properties by microrheology in the presence of optical traps. *Phy Rev E*, 73:061501, 2006.
- [55] R. Kubo. The fluctuation-dissipation theorem. *Rep. Prog. Phys.*, 29:255–284, 1966.
- [56] A. Einstein. On the motion of small particles suspended in liquids at rest required by the molecular-kinetic theory of heat. *Annalen der Physik*, 17:549–560, 1905.
- [57] T. G. Mason and D. A. Weitz. Optical measurements of frequency-dependent linear viscoelastic moduli of complex fluids. *Phys. Rev. Lett.*, 74:1250–1253, 1995.

- [58] L.D. Landau and E.M. Lifshitz. *Statistical Physics*. Butterworth-Heinemann, 1980.
- [59] F. Gittes, B. Schnurr, P. D. Olmsted, F. C. MacKintosh, and C. F. Schmidt. Microscopic viscoelasticity: shear moduli of soft materials determined from thermal fluctuations. *Phys. Rev. Lett.*, 79:3286–3289, 1997.
- [60] M. T. Valentine, P. D. Kaplan, D. Thota, J. C. Crocker, T. Gisler, R. K. Prud'homme, M. Beck, and D. A. Weitz. Investigating the microenvironments of inhomogeneous soft materials with multiple particle tracking. *Phys. Rev. E*, 64:061506, 2001.
- [61] E. Fallman and O. Axner. Design for fully steerable dual-trap optical tweezers. *App. Opt.*, 36:2107–2113, 1997.
- [62] P. C. Lee and D. Meisel. Adsorption and surface-enhanced Raman of dyes on silver and gold sols. *J. Phys. Chem.*, 86:3391—3395, 1982.
- [63] N. Leopold and B. Lendl. A new method for fast preparation of highly surface-enhanced Raman scattering (SERS) active silver colloids at room temperature by reduction of silver nitrate with hydroxylamine hydrochloride. *J. Phys. Chem. B*, 107:5723—5727, 2003.
- [64] S. Balint, M. P. Kreuzer, S. Rao, G. Badenes, P. Miskovsky, and D. Petrov. Simple route for preparing optically trappable probes for surface-enhanced Raman scattering. *J. Phys. Chem. C*, 113:17724–17729, 2009.
- [65] I. Mikhailyuk and A. Razzhivin. Background subtraction in experimental data arrays illustrated by the example of Raman spectra and fluorescent gel electrophoresis patterns. *Instr. Exp. Tech.*, 46:765—769, 2003.
- [66] I. Noda and Y. Ozaki. *Two-dimensional correlation spectroscopy - applications in vibrational and optical spectroscopy*. John Wiley and Sons, England., 2004.
- [67] Alvin C. Rencher. *Methods of Multivariate Analysis*. John Wiley and Sons, USA, 2002.
- [68] D. Mizuno, R. Bacabac, C. Tardin, D. Head, and C. F. Schmidt. High-resolution probing of cellular force transmission. *Phys. Rev. Lett.*, 102:168102, 2009.
- [69] K. Kneipp, Y. Wang, H. Kneipp, L. T. Perelman, I. Itzkan, R. R. Dasari, and M. S. Feld. Single molecule detection using surface-enhanced Raman scattering (SERS). *Phys. Rev. Lett.*, 78:1667—1670, 1997.
- [70] H. Xu, E. J. Bjerneld, M. Käll, and L. Börjesson. Spectroscopy of single hemoglobin molecules by surface enhanced Raman scattering. *Phys. Rev. Lett.*, 83(21):4357–4360, 1999.
- [71] E. Le Ru and P. Etchegoin. *Principles of Surface-Enhanced Raman Spectroscopy: and related plasmonic effects*. Elsevier, 2009.
- [72] B. Prescott, W. Steinmetz, and G. J. Thomas. Characterization of DNA structures by laser raman spectroscopy. *Biopolymers*, 23:235—256, 1984.

- [73] Y. C. Cao, R. Jin, and C. A. Mirkin. Nanoparticles with Raman spectroscopic fingerprints for DNA and RNA detection. *Science*, 297:1536–1540, 2002.
- [74] L. Movileanu, J. M. Benevides, and G. J. Thomas. Temperature dependence of the Raman spectrum of DNA. II. Raman signatures of premelting and melting transitions of poly(dA).poly(dT) and comparison with poly(dA-dT).poly(dA-dT). *Biopolymers*, 63:181–194, 2002.
- [75] A. Barhoumi, D. Zhang, F. Tam, and N. J. Halas. Surface-enhanced Raman spectroscopy of DNA. *JACS*, 130:5523–5529, 2008.
- [76] K. Kneipp, H. Kneipp, V. B. Kartha, R. Manoharan, G. Deinum, I. Itzkan, R. R. Dasari, and M. S. Feld. Detection and identification of a single DNA base molecule using surface-enhanced Raman scattering (SERS). *Phys. Rev. E*, 57:R6281–R6284, 1998.
- [77] A. MacAskill, D. Crawford, D. Graham, and K. Faulds. DNA sequence detection using surface-enhanced resonance Raman spectroscopy in a homogenous multiplexed assay. *Anal. Chem.*, 81:8134–8140, 2009.
- [78] H. Wei and H. Xu. Surface-enhanced Raman scattering of λ -DNA. *Appl. Phys. A*, 89:273–2757, 2007.
- [79] G. J. Thomas, J. M. Benevides, S. A. Overman, T. Ueda, K. Ushizawa, M. Saitoh, and M. Tsuboi. Polarized Raman spectra of oriented fibers of A DNA and B DNA: Anisotropic and isotropic local Raman tensors of base and backbone vibrations. *Biophys. J.*, 68:1073–1088, 1995.
- [80] R. C. Lord and G. Thomas Jr. Raman spectral studies of nucleic acids and related molecules — i ribonucleic acid derivatives. *Spectrochimica Acta A*, 23:2551–2591, 1967.
- [81] W. Ke, D. Zhou, J. Wu, and K. Ji. Surface-enhanced Raman spectra of calf thymus DNA adsorbed on concentrated silver colloid. *Appl. Spect.*, 59(4):418–423, 2005.
- [82] M. D. Wang, H. Yin, R. Landick, J. Gelles, and S. M. Block. Stretching DNA with optical tweezers. *Biophysical J.*, 72:1335–1346, 1997.
- [83] C. Bouchiat, M. D. Wang, J. F. Alemand, T. Strick, S. M. Block, and V. Croquette. Estimating the persistence length of a worm-like chain molecule from force-extension measurements. *Biophys. J.*, 76:409–413, 1999.
- [84] A. Carter, Y. Seol, and T. Perkins. Precision surface-coupled optical-trapping assay with one-basepair resolution. *Biophys. J.*, 96(7):2926–2934, 2009.
- [85] C. Bustamante, S. Smith, J. Liphardt, and D. Smith. Single molecule studies of DNA mechanics. *Curr. Opinion in Struct. Biology*, 10:279–285, 2000.
- [86] C. Bustamante, Z. Bryant, and S. B. Smith. Ten years of tension: single-molecule DNA mechanics. *Nature*, 421:423–427, 2003.

- [87] J. F. Marko and E. D. Siggia. Stretching dna. *Macromolecules*, 28:8759–8770, 1995.
- [88] M. Woodside, P. Anthony, W. Behnke-Parks, K. Larizadeh, D. Herschlag, and S. Block. Direct measurement of the full, sequence-dependent folding landscape of a nucleic acid. *Science*, 314:1001–1004, 2006.
- [89] X. Qian and S. Nie. Single-molecule and single-nanoparticle SERS: from fundamental mechanisms to biomedical applications. *Chem. Soc. Rev.*, 37:912–920, 2008.
- [90] T. Yano, P. Verma, Y. Saito, T. Ichimura, and S. Kawata. Pressure-assisted tip-enhanced Raman imaging at a resolution of a few nanometers. *Nat. Photon.*, 3:473–477, 2009.
- [91] J. Rezac, P. Hobza, and S. A. Harris. Stretched DNA investigated using molecular-dynamics and quantum-mechanical calculations. *Biophysical J.*, 98:101–110, 2010.
- [92] G. Bao and S. Suresh. Cell and molecular mechanics of biological materials. *Nature Materials*, 2:715–725, 2003.
- [93] S. Guido and G. Tomaiuolo. Microconfined flow behavior of red blood cells in vitro. *C. R. Physique*, 10:751–763, 2009.
- [94] S. Chien. Red cell deformability and its relevance to blood flow. *Ann. Rev. Physiol.*, 49:177–192, 1987.
- [95] S. Suresh. Mechanical response of human red blood cells in health and disease: Some structure-property-function relationships. *J. Mater. Res.*, 21:1871–1877, 2006.
- [96] E. A. Evans. New membrane concept applied to the analysis of fluid shear- and micropipette-deformed red blood cells. *Biophys. J.*, 13:941–954, 1973.
- [97] A. Tozeren, R. Skalak, K. L. Sung, and S. Chien. Viscoelastic behavior of erythrocyte membrane. *Biophys. J.*, 39:23–32, 1982.
- [98] K. C. Neuman and A. Nagy. Single-molecule force spectroscopy: optical tweezers, magnetic tweezers and atomic force microscopy. *Nature Methods*, 5:491–505, 2008.
- [99] S. Henon, G. Lenormand, A. Richert, and F. Gallet. A new determination of the shear modulus of the human erythrocyte membrane using optical tweezer. *Biophys. J.*, 76:1145–1151, 1999.
- [100] M. Dao, C.T. Lim, and S. Suresh. Mechanics of the human red blood cell deformed by optical tweezers. *J. Mech. Phys. Solids*, 51:2259–2280, 2003.
- [101] J. P. Mills, L. Qie, M. Dao, C. T. Lim, and S. Suresh. Nonlinear elastic and viscoelastic deformation of the human red blood cell with optical tweezers. *Mol. Cell Bio.*, 1:169–180, 2004.

- [102] A. Fontes, M. L. Barjas Castro, M. M. Brandao, H. P. Fernandes, A. A. Thomaz, R. R. Huruta, L. Y. Pozzo, L. C. Barbosa, F. F. Costa, S. T. O. Saad, and C. L. Cesar. Mechanical and electrical properties of red blood cells using optical tweezers. *J. Opt.*, 13:044012, 2011.
- [103] G. Lenormand, S. Henon, A. Richert, J. Simeon, and F. Gallet. Direct measurement of the area expansion and shear moduli of the human red blood cell membrane skeleton. *Biophys. J.*, 81:43–56, 2001.
- [104] S Rao, S Balint, B Cossins, V Guallar, and D Petrov. Raman study of mechanically induced oxygenation state transition of red blood cells using optical tweezers. *Biophys. J.*, 96:209–216, 2009.
- [105] L. Starrs and P. Bartlett. Colloidal dynamics in polymer solutions: Optical two-point microrheology measurements. *Faraday Discuss.*, 123:323–334, 2003.
- [106] S. C. Goheen, L. J. Lis, O. Kucuk, M. P. Westerman, and J. W. Kaufman. Compositional dependence of spectral features in the Raman spectra of erythrocyte membranes. *J. Raman Spectrosc.*, 24:275–279, 1993.
- [107] J. L. Lippert, L. E. Gorczyca, and G. Meiklejohn. A laser Raman spectroscopic investigation of phospholipid and protein configurations in hemoglobin-free erythrocyte ghosts. *Biochimica et Biophysica Acta*, 382:51–57, 1975.
- [108] D. F. H. Wallach and S. P. Verma. Raman and resonance-Raman scattering by erythrocyte ghosts. *Biochimica et Biophysica Acta*, 382:542–551, 1975.
- [109] R. D. Snook, T. J. Harvey, E. C. Faria, and P. Gardner. Raman tweezers and their application to the study of singly trapped eukaryotic cells. *Integrative Biology*, 1:43–52, 2009.
- [110] B. R. Wood, P. Caspers, G. J. Puppels, S. Pandiancherri, and D. McNaughton. Resonance Raman spectroscopy of red blood cells using near-infrared laser excitation. *Anal Bioanal Chem*, 387:1691–1703, 2007.
- [111] M. Puig de Morales-Marinkovic, K. T. Turner, J. P. Butler, J. J. Fredberg, and S. Suresh. Viscoelasticity of the human red blood cell. *Am J Physiol. Cell Physiol.*, 293:597–605, 2007.
- [112] S. Amin, Y. K. Park, N. Lue, R. R. Dasari, K. Badizadegan, M. S. Feld, and G. Popescu. Microrheology of red blood cell membranes using dynamic scattering microscopy. *Optics Express*, 15:17001–17009, 2007.
- [113] Y. Z. Yoon, J. Kotar, A. T. Brown, and P. Cicuta. Red blood cell dynamics: from spontaneous fluctuations to non-linear response. *Soft Matter*, 7:2042–2051, 2011.
- [114] C. H. Reinsch. Smoothing by spline functions. *Numerische Mathematik*, 10:177–183, 1967.
- [115] YZ. Yoon, J. Kotar, G. Yoon, and P. Cicuta. Non-linear mechanical response of the red blood cell. *Phys. Biology*, 5:036007, 2008.

- [116] Y. Liu, D. K. Cheng, G. J. Sonek, M. W. Berns, C. F. Chapman, and B. J. Tromberg. Evidence for localized cell heating induced by infrared optical tweezers. *Biophys. J.*, 68:2137–2144, 1995.
- [117] G. J. Brouhard, H. T. Schek III, and A. J. Hunt. Advanced optical tweezers for the study of cellular and molecular biomechanics. *IEEE Trans Biomed Eng.*, 50:121–125, 2003.
- [118] T. Betz, M. Lenz, JF. Joanny, and C. Sykes. ATP-dependent mechanics of red blood cells. *PNAS*, 106:15312–15317, 2009.
- [119] R. R. Brau, J. M. Ferrer, H. Lee, C. E. Castro, B. K. Tam, P. B. Tarsa, P. Matsudaira, M. C. Boyce, R. D. Kamm, and M. J. Lang. Passive and active microrheology with optical tweezers. *J. Opt. A: Pure Appl. Opt.*, 9:S103–S112, 2007.
- [120] N. S. Gov. Active elastic network: Cytoskeleton of the red blood cell. *Phys. Rev. E*, 75:011921, 2007.
- [121] F. Gallet, D. Arcizet, P. Bohec, and A. Richert. Power spectrum of out-of-equilibrium forces in living cells: amplitude and frequency dependence. *Soft Matter*, 5:2947–2953, 2009.
- [122] L. A. Hough and H. D. Ou-Yang. Correlated motions of two hydrodynamically coupled particles confined in separate quadratic potential wells. *Phys. Rev. E*, 65:021906, 2002.
- [123] J. Chan, S. Fore, S. Wachsmann-Hogiu, and T. Huser. Raman spectroscopy and microscopy of individual cells and cellular components. *Lasers and Photonics Review*, 2:325–349, 2008.
- [124] N. Shaklai, J. Yguerabide, and HM. Ranney. Interaction of hemoglobin with red blood cell membranes as shown by a fluorescent chromophore. *Biochemistry*, 16:5585–5592, 1977.
- [125] S. Fischer, RL. Nagel, RM. Bookchin, EF. Roth Jr, and I. Tellez-Nagel. The binding of hemoglobin to membranes of normal and sickle erythrocytes. *Biochimica et Biophysica Acta*, 375:422–433, 1975.
- [126] A. Bankapur, E. Zachariah, S. Chidangil, M. Valiathan, and D. Mathur. Raman tweezers spectroscopy of live, single red and white blood cells. *PLoS ONE*, 5:e10427, 2010.
- [127] B. R. Wood and D. McNaughton. Raman excitation wavelength investigation of single red blood cells in vivo. *J. Raman Spectrosc.*, 33:517–523, 2002.
- [128] B. R. Wood, B. Tait, and D. McNaughton. Micro-Raman characterisation of the R to T state transition of haemoglobin within a single living erythrocyte. *Biochimica et Biophysica Acta*, 1539:58–70, 2001.
- [129] H. Brunner and H. Sussner. Resonance Raman scattering of haemoglobin. *Biochimica et Biophysica Acta*, 310:20–31, 1973.

- [130] S. Hu, K. M. Smith, and T. G. Spiro. Assignment of protoheme resonance Raman spectrum by heme labeling in myoglobin. *J. Am. Chem. Soc.*, 118:12638–12646, 1996.
- [131] XL. Yan, RX. Dong, L. Zhang, XJ. Zhang, and ZW. Zhang. Raman spectra of single cell from gastrointestinal cancer patients. *World J Gastroenterol*, 11:3290–3292, 2005.
- [132] A. Jay and P. Canham. Viscoelastic properties of the human red blood cell membrane. II. Area and volume of individual red cells entering a micropipette. *Biophys. J.*, 17:169–178, 1977.
- [133] A.C. De Luca, G. Rusciano, R. Clacia, V. Martinelli, and G. Pesce. Spectroscopical and mechanical characterization of normal and thalassemic red blood cells by Raman tweezers. *Opt. Exp.*, 16:7943–7956, 2008.
- [134] T.J. Harvey, E.C. Faria, A. Henderson, E. Gazi, A.D. Ward, N. W. Clarke, M. D. Brown, R. D. Snook, and P. Gardner. Spectral discrimination of live prostate and bladder cancer cell lines using Raman optical tweezers. *J Biomed. Opt.*, 13:1–12, 2008.
- [135] K. Chen, Y. Oin, F. Zheng, M. Sun, and D. Shi. Diagnosis of colorectal cancer using Raman spectroscopy of laser-trapped single living epithelial cells. *Opt. Letters*, 31:2015–2017, 2006.
- [136] J.W. Chan, D.S. Taylor, T. Zwerdling, S.M. Lane, and K. Ihara. Micro-Raman spectroscopy detects individual neoplastic and normal hematopoietic cells. *Biophys. J*, 90:648–656, 2006.
- [137] J.L. Deng, Q. Wei, M.H. Zhang, and Y.Q. Li. Study of the effect of alcohol on single human red blood cells using near-infrared laser tweezers Raman spectroscopy. *J Raman Spectros*, 36:257–261, 2005.
- [138] B. L. Horecker. The absorption spectra of hemoglobin and its derivatives in the visible and near infra-red region. *J. Biol. Chem.*, 148:173–183, 1943.
- [139] V. Bennett and P. J. Stenbuck. Human erythrocyte ankyrin. purification and properties. *J Biol Chem.*, 255:2540–2548, 1980.
- [140] J. W. Hatfield and S. R. Quake. Dynamic properties of an extended polymer in solution. *Phys. Rev. Lett.*, 82:3548–3551, 1999.
- [141] I. A. Martínez, S. Raj, and D. Petrov. Colored noise in the fluctuations of an extended DNA molecule detected by optical trapping. *Eur. Biophys. J.*, 41:99–106, 2012.
- [142] W. J. Greenleaf, M. T. Woodside, and S. M. Block. High-resolution single-molecule measurements of biomolecular motion. *Annu. Rev. Biophys. Biomol. Struc.*, 36:171–190, 2007.
- [143] J. C. Meiners and S. R. Quake. Direct measurement of hydrodynamic cross correlations between two particles in an external potential. *Phys. Rev. Lett.*, 82:2211–2214, 1999.

-
- [144] L. D. Williams and L. J. Maher. Electrostatic mechanisms of DNA deformation. *Annu. Rev. Biophys. Biomol. Struct.*, 29:497–521, 2000.
- [145] J. Kovac and C. C. Crabb. Modified Gaussian model for rubber elasticity. 2. The wormlike chain. *Macromolecules*, 15:537–541, 1982.